

CHARACTERISTICS OF MUON PAIR PRODUCTION
IN P-P COLLISIONS AT VERY HIGH ENERGIES
AS A PROBE OF PROTON CONSTITUENTS

BY

JOSEPH ALAN PARADISO

B.S.E.E. Tufts University
1977

SUBMITTED TO THE DEPARTMENT OF
PHYSICS IN PARTIAL FULFILLMENT
OF THE REQUIREMENTS FOR THE
DEGREE OF

Doctor of Philosophy

at the

MASSACHUSETTS INSTITUTE OF TECHNOLOGY

April 1981

©Massachusetts Institute of Technology 1981

Signature of Author _____

Department of Physics
April 29, 1981

Certified by _____

Ulrich Becker
Thesis Supervisor

Accepted by _____

George F. Koster
Chairman, Department Committee

CHARACTERISTICS OF MUON PAIR PRODUCTION
IN P-P COLLISIONS AT VERY HIGH ENERGIES
AS A PROBE OF PROTON CONSTITUENTS

by

JOSEPH ALAN PARADISO

Submitted to the Department of Physics in
April, 1981 in partial fulfillment of the
requirements for the Degree of
Doctor of Philosophy

ABSTRACT

The reaction $P + P \rightarrow \mu^+ + \mu^- + (\text{anything})$ has been measured at the CERN Intersecting Storage Rings. A large-acceptance magnetized-iron spectrometer was employed, and muon pairs with masses between 2 and 25 GeV were observed. We have accumulated a total of 7827 events with an integrated luminosity of $1.12 \cdot 10^{38} \text{ cm}^{-2}$ at $\sqrt{s} = 62 \text{ GeV}$, and 1509 events with a luminosity of $0.42 \cdot 10^{38} \text{ cm}^{-2}$ at $\sqrt{s} = 44 \text{ GeV}$; presently the highest available energies. The ISR collides protons against protons, hence the data is free of corrections necessary for measurements made with nuclear targets.

Cross-sections are given for J and T production, and an upper limit of $\sigma < 40 \cdot 10^{-38} \text{ cm}^2$ is set on new heavy resonances $X \rightarrow \mu^+ + \mu^-$ for $m_X > 20 \text{ GeV}$. The continuum is examined down to the smallest $\sqrt{T} = m/\sqrt{s} = 0.07$. No significant indication of scaling violation is seen in a comparison with lower energy data. The measured cross-section is found to be a factor 1.6 above Drell-Yan predictions using structure functions determined from deep-inelastic neutrino scattering data.

The dependence of dilepton production on $X_F = p_{||}/p_{(\text{max})}$, transverse momentum, and helicity angle is measured. The X_F distributions are compared with Drell-Yan predictions. A steeper X_F dependence is seen at the T region than in the surrounding continuum. The helicity distributions are described by the form $1 + \eta \cdot \cos^2 \theta$ (with $\eta \gtrsim 1$) and indications are found for $\eta < 1$ in the T region. The average transverse momentum is observed to increase with mass and beam energy, reaching large values of up to 2 GeV. The shape of the p_t distributions and dependence of $\langle p_t \rangle$ on mass and s are compared with QCD calculations.

Fits are made to the proton sea-quark distributions, using valence-quark parameterizations in the Drell-Yan formula derived from neutrino scattering experiments.

Distributions of hadron multiplicity are presented, and an excess of dimuons with no associated hadrons is observed at $\sqrt{s} = 62 \text{ GeV}$. The mass distributions of the hadronless dimuons are compared with predictions based on the 2γ process in proton collisions.

Thesis Supervisor: Dr. Ulrich Becker

Title: Professor of Physics

TABLE OF CONTENTS

ABSTRACT.....	2
SECTION I INTRODUCTION.....	5
References.....	10
Figures.....	12
SECTION II THE APPARATUS.....	16
II-1) The Spectrometer.....	16
II-2) The Triggering System.....	18
II-3) Reconstruction, Resolution, and Acceptance.....	20
II-4) Luminosity Measurement.....	24
References.....	26
Tables.....	27
Figures.....	28
SECTION III THE ANALYSIS.....	42
III-1) Overview.....	42
III-2) Pass 1, Tape Reduction.....	42
III-3) Pass 2, Momentum Reconstruction.....	43
III-4) Pass 3, Data and Background Processing.....	45
III-5) Pass 4, Redundancy Check.....	48
III-6) Pass 5, Cross-Section Formulation.....	48
a) Monte-Carlo Reweighting.....	48
b) Fiducial Cuts.....	50
c) Event Scan.....	53
d) Background Subtraction.....	55
e) Acceptance and Cross-Section Calculation.....	56
III-7) Pass 6, Normalization and Data Fitting.....	59
III-8) Analysis Comparison.....	59
References.....	61
Tables.....	62
Figures.....	68
SECTION IV RESULTS.....	88
IV-1) The Mass Spectra.....	88
a) Parameterization.....	88
b) Resonances.....	88
c) Scaling Comparison.....	90
d) Comparison with the Drell-Yan Formula.....	91
IV-2) Dependence on X_F	93
IV-3) Dependence on $\cos\theta_{CS}$	93
IV-4) Transverse Momentum.....	94
IV-5) Fits to the Sea Quark Distribution.....	95
References.....	97
Tables.....	99
Figures.....	103
CONCLUSIONS.....	116

TABLE OF CONTENTS (cont.)

APPENDIX I	DEFINITIONS.....	117
	Figures.....	118
APPENDIX II	SENSITIVITIES AND SYSTEMATICS.....	119
	AII-1) Sensitivity to Production Parameters.....	119
	AII-2) Background Sensitivity.....	120
	AII-3) Normalization Error.....	120
	Figures.....	121
APPENDIX III	THE CDC ANALYSIS AND THE AVERAGING PROCESS...	133
	AIII-1) The CDC Analysis.....	133
	a) Pass 1.....	133
	b) Pass 2.....	134
	c) Pass 3 and beyond.....	135
	AIII-2) The Averaging Process.....	135
APPENDIX IV	SEARCH FOR EVIDENCE OF THE 2γ PROCESS.....	136
	Figures.....	139
ACKNOWLEDGMENTS	143

SECTION I INTRODUCTION

Indications of pointlike constituents inside protons came from deep-inelastic electron scattering experiments¹⁾ performed at SLAC in 1968, which measured the structure function νW_2 and showed it to scale as a function of the dimensionless quantity $\omega \equiv 2M_P \nu/q^2$, independent of ν ($\equiv E - E'$ of the scattered electron) and q^2 ($q \equiv 4$ -momentum transfer) separately. This behavior was understood²⁾ in terms of incident electrons scattering against point-like "partons" inside of the nucleons.

The deep-inelastic scattering process is sketched in Fig. I-1 (a). The hadroproduction of lepton pairs is given in the crossed diagram (Fig. I-1 (b)). Here the lepton pair arises from the decay of a timelike photon resulting from the annihilation of a quark and anti-quark associated with the incident hadrons. The electromagnetic coupling of the timelike photon to the nucleon constituents thus provides a probe which is exploited by experiments measuring the hadroproduction of dileptons. The measurements presented in this thesis investigate dimuon production in proton collisions at the highest incident energies yet attained, currently available only at the ISR.

Most experiments studying dilepton production were also motivated to search for neutral vector mesons decaying into lepton pairs and dominating production at their resonant masses. The $J^3)$ and $T^4)$ were originally detected in this way. These are described theoretically as bound states of charmed and bottom quarks with their respective anti-quarks. Symmetry considerations suggest the existence of a sixth (top) quark, which will produce a family of heavier resonances yet unseen in experiments. The intermediate vector boson (Z_0) predicted by electro-weak theory decays into lepton pairs and has also been searched for in dilepton experiments. Current arguments and results, however, place the Z_0 and toponium masses above⁵⁾ the reach of existing accelerators and postpone this quest until higher energies are attained.

One of the first lepton pair experiments⁶⁾ investigated proton-nucleus collisions using the 29.5 GeV proton beam at BNL and measured a continuum of muon pairs with masses up to 5 GeV, which could not be adequately explained in terms of processes known at that time.

In 1970 Drell and Yan constructed a model⁷⁾ of dilepton production from hadron collisions in which a massive virtual photon arises from the electromagnetic annihilation of a "valence" quark from one hadron with an anti-quark plucked from the virtual "sea" associated with the other hadron. This virtual photon decays into the observed lepton pair. The mass spectrum predicted by this model successfully fit the continuum as first measured in Ref. 6.

The Drell-Yan model assumes a "pointlike" coupling between the quarks and photon, and postulates both annihilating quarks to act independently of the other "spectator" quarks in the interaction ("impulse approximation").* The diagram for the Drell-Yan interaction is illustrated in Fig. I-1 (b). The double-differential cross-section may easily be expressed in terms of this model⁸⁾:

$$\text{Eq. I-1)} \quad \frac{d^2\sigma}{dm dX_F} = \frac{8\pi\alpha^2}{3m^3} \cdot \frac{1}{N_c} \cdot \sum_i \left[\frac{e_i^2}{x_1 + x_2} (q_i(x_1)\bar{q}_i(x_2) + q_i(x_2)\bar{q}_i(x_1)) \right]$$

where:

x_1 = Fraction of total nucleon momentum carried by quark #1.

x_2 = Fraction of total nucleon momentum carried by quark #2.

q_i, \bar{q}_i = Structure functions of nucleon. These are defined as $x f_i(x)$, where $f_i(x)$ is the probability of quark_i having fractional momentum x . The valence distributions are normalized such that $\int_0^1 f_i(x) dx = \#$ of quarks of flavor "i" composing the nucleon. Here we have colliding protons, hence 2 up and 1 down valence quarks; heavier flavors and anti-quarks must come from the "sea".

e_i = Electric charge of quark flavor "i" ($\pm 1/3$ or $\pm 2/3$ electron charge).

N_c = Number of color states possible per quark, presently $N_c=3$.

†) It has been shown¹²⁾ that the sea-content of strange and heavier quarks is comparatively small.

*) For $m < 3$ GeV, there exists a low-mass continuum¹³⁾ (against the backdrop of resonances), which is not explained by the Drell-Yan mechanism due to inaccuracy in the impulse approximation. Other mechanisms (see Ref.14), based on softer annihilation processes and hadron decay, have been proposed to explain this phenomenon.

m = Mass of lepton pair.

X_F = Feynman scaling variable $\equiv p_{||} / p_{(\max.)}$ (see App. I).

The cross-section for the subprocess $q_1 + \bar{q}_1 \rightarrow \ell^+ + \ell^-$ ($\ell \equiv$ lepton) is (in analogy to electron-positron annihilation) $\sigma = 4\pi\alpha q_1^2 / 3m^4$, which yields the factor in front of Eq.I-1. The color-factor is included due to the requirement that the quark/anti-quark must have corresponding color/anti-color to annihilate. The terms enclosed in brackets represent the probability of locating the required quark and anti-quark associated with the colliding particles, weighted by the square of the quark charge. The sum runs over all quark flavors.

Expressing x_1 and x_2 in terms of the mass and X_F of the lepton pair yields:

$$\begin{aligned} \text{Eq. I-2)} \quad X_F &= x_1 - x_2 & \tau &\equiv m^2/s = x_1 x_2 \\ m^2 &\approx s \cdot x_1 x_2 & x_{1,2} &= \frac{1}{2} [\sqrt{X_F^2 + 4\tau} \pm X_F] \end{aligned}$$

Assuming similarity between time-like and space-like probing, the structure functions measured in deep-inelastic scattering experiments can be used. Multi-parameter fits to the actual dilepton cross-sections can also extract structure functions; in many cases a combination of both techniques is used.⁹⁾

The original Drell-Yan formula lacked the color factor N_c , which was introduced later in accordance with the postulations of Quantum Chromodynamics. QCD also predicts an additional yield of dileptons via mechanisms involving gluon processes.

Diagrams involving hard gluon emission are added to the Drell-Yan process of Fig. I-1(b). The first-order diagrams in α_s are shown in Fig. I-2 (called the "Compton" and "Annihilation" diagrams in analogy to their correspondence with QED). The effects of these diagrams have been estimated,¹⁰⁾ however the contribution from higher-order processes (Fig. I-3) may also be significant. QCD introduces additional corrections from the radiation of soft gluons,¹¹⁾ in analogy with QED radiative corrections.

Throughout this thesis, our measurements are analyzed within the framework of the Drell-Yan model. As indicated above, the Drell-Yan process is essentially the "zero'th-order" term in QCD expansion, and theoretical predictions of dilepton production characteristics are currently being revised to account for the effects of higher-order processes, which have not yet been rigorously calculated. In cases where our data is in significant disagreement with Drell-Yan (ie. P_t and normalization; see below) the influence expected from QCD is mentioned.

In particular, the following characteristics of the continuum are examined:

- 1) Equations I-1 and I-2 yield the hypothesis of scaling, ie. the dimensionless form of the cross-section will depend only on the parameter τ :

$$\text{Eq. I-3)} \quad m^3 \frac{d^2\sigma}{dm dX_F} = F(\tau)$$

We test this by comparing our measurements at 62 and 44 GeV. A comparison with lower energy data collected by experiments using nuclear targets tests scaling over the largest energy range available.

- 2) Due to the point-like coupling of the spin- $\frac{1}{2}$ quarks to the virtual photon, one expects the Drell-Yan dimuons to be produced with a dependence on the polar angle of the form $1 + \cos^2\theta$. Our data tests this prediction at ISR energies and examines polarization at the T resonance.
- 3) The quarks have only longitudinal momentum in the simple Drell-Yan picture, hence the dileptons are predicted to be produced with essentially no P_t . The confinement constraints alone provide a "primordial" transverse momentum of $k_t \approx 300 \text{ MeV}^{15)}$ to the quarks, and even after adding this to the model, the P_t of the produced dilepton falls far short of that measured in experiment.¹⁶⁾ The primordial momentum should not vary with beam energy, hence the P_t of the Drell-Yan dimuons will show no dependence on s . QCD corrections increase the mean P_t of the dileptons and introduce dependence of $\langle P_t \rangle$ on beam energy. This experiment tests QCD predictions via the measured P_t distributions. We have measured $\langle P_t \rangle$ at the highest available energies and masses, thus our results provide an important investigation into the evolution

of $\langle P_t \rangle$ with s and m .

- 4) QCD calculations will affect the predicted normalization of the continuum cross-section. Lepton pair experiments have produced cross-sections above the Drell-Yan prediction and theoretical arguments¹⁷⁾ expect an approximate factor of two; the major contribution is thought to come from the vertex correction (Fig. I-3 (d)). The present QCD estimates are somewhat coarse however, due to a lack of knowledge concerning contributions from higher-order diagrams.

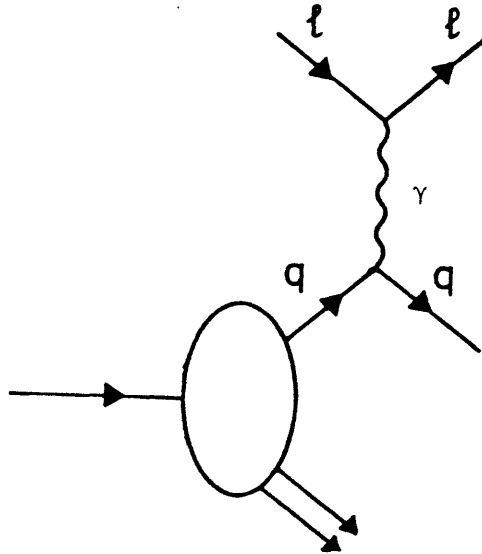
The two-photon effect (see Fig. I-4) is also a source of dileptons; here the incoming protons emit two photons which interact to form the observed lepton pair. The yield of dileptons in proton collisions from the two-photon effect has been calculated.¹⁸⁾ The cross-section increases with $[\ln(s)]^3$. At ISR energies, the 2-photon process should produce a measurable yield of dileptons,¹⁹⁾ and at even higher energies, it will provide a considerable source of background to the Drell-Yan continuum. Our data provides the only possibility at present to search for muon pair production by the 2γ effect in proton collisions; such a search is attempted in this thesis.

SECTION I - REFERENCES

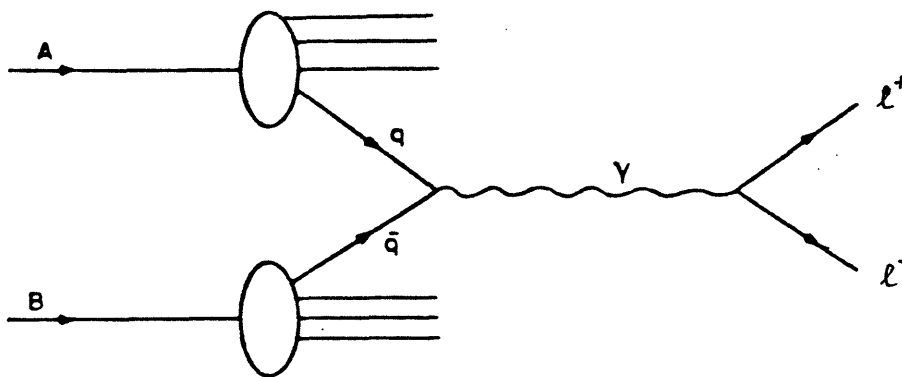
- 1) E.M. Riordan, Thesis MIT, June (1973).
J.I. Friedman and H.W. Kendal, Ann. Rev. Nucl. Sci. 22, 203 (1969).
M. Breidenbach et. al., Phys. Rev. Lett. 23, 935 (1969).
- 2) J.D. Bjorken, Phys. Rev. 179, 1547 (1969).
J.D. Bjorken and E.A. Paschos, Phys. Rev. 185, 1975 (1969).
- 3) J.J. Aubert et. al., Phys. Rev. Lett. 33, 1404 (1974).
J.E. Augustin et. al., Phys. Rev. Lett. 33, 1406, (1974).
- 4) S.W. Herb et. al., Phys. Rev. Lett. 39, 252 (1977).
W.R. Innes et. al., Phys. Rev. Lett. 39, 1240, 1640(E) (1977).
- 5) J.P. Revol, Thesis MIT, and refs. therein, April 1981.
M. White, Thesis MIT, and refs. therein, April 1981.
- 6) J. Christenson et. al., Phys. Rev. Lett. 25, 1523 (1970).
- 7) S.D. Drell and T.M. Yan, Phys. Rev. Lett. 25, 316, 902(E) (1970).
- 8) G. Altarelli, Proc. of the EPS Int. Conf. on High-Energy Phys. Vol 2, 727 (1979).
- 9) A.S. Ito et. al., Fermilab-PUB-80/19-EXP-80 (1980).
J. Badier et. al., Phys. Lett. 89B, 145 (1979).
F.T. Dao et. al., Phys. Rev. Lett. 39, 1388 (1977).
G.R. Farrar, Nucl. Phys. B 77, 429 (1974).
- 10) H. Fritzsche and P. Minkowski, Phys. Lett. 73B, 80 (1980).
Yu. L. Dokshitser et. al., Phys. Reports 58, 269 (1980).
M. Chaichian et. al., Nuc. Phys. B 175, 493 (1980).
G. Parisi and R. Petronzio, Nuc. Phys. B 154, 427 (1979).
G. Altarelli et. al., Phys. Lett. 76, 351 and 356 (1978).
F. Halzen and D.M. Scott, Phys. Rev. D 18, 3378 (1978).
- 11) H.D. Politzer, Nuc. Phys. B 129, 301 (1977).
- 12) J.G.H. De Groot et. al., Zeit. Phys. C1, 143 (1979).
- 13) K. Bunnell et. al., Phys. Rev. Lett. 40, 136 (1978).
R. Stroynowski et. al., Phys. Lett. 97B, 315 (1980).
- 14) D.M. Grannan et. al., Phys. Rev. D 18, 3150 (1978).
I.H. Dunbar, Phys. Rev. Lett. 41, 210 (1978).
E.V. Shuryak, Phys. Lett. 78B, 150 (1978).

- 15) The MARK-J Collaboration , Phys. Reports 63, 337-391 (1980).
R. Brandelik et. al., DESY preprint 80/40 (1980).
- 16) D. Antreasyan et. al., "Production Mechanisms of High-Mass Muon Pairs",
submitted to Phys. Rev. Letters.
See also Sec. IV of this thesis, and refs. therein.
- 17) G. Altarelli et. al., Nucl. Phys. B 143, 521 and 146, 544 (1978)
and 157, 461 (1979).
J. Kubar et. al., Nucl. Phys. B 175, 251 (1980).
- 18) J.A.M. Vermaseren, private communication.
R. Moore, Z. Phys. C5, 351 (1980).
C.E. Carlson and K.E. Lassila, Phys. Lett. 97B, 291 (1980).
- 19) F. Vannucci, CERN Preprint EP/80-82 (1980).

FIGURE I-1 PROCESSES PROBING NUCLEON CONSTITUENTS
WITH VIRTUAL PHOTONS



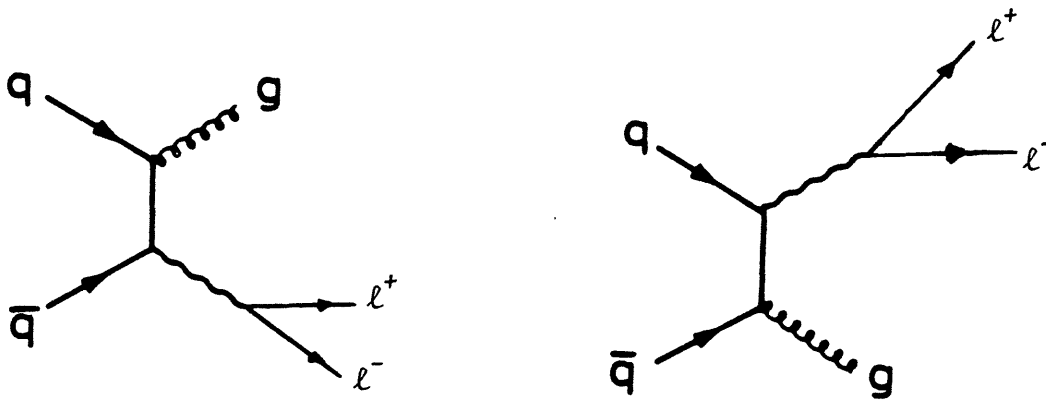
- a) The Deep-Inelastic Scattering Process. The incoming lepton couples to a constituent quark in a target nucleon via a spacelike photon.



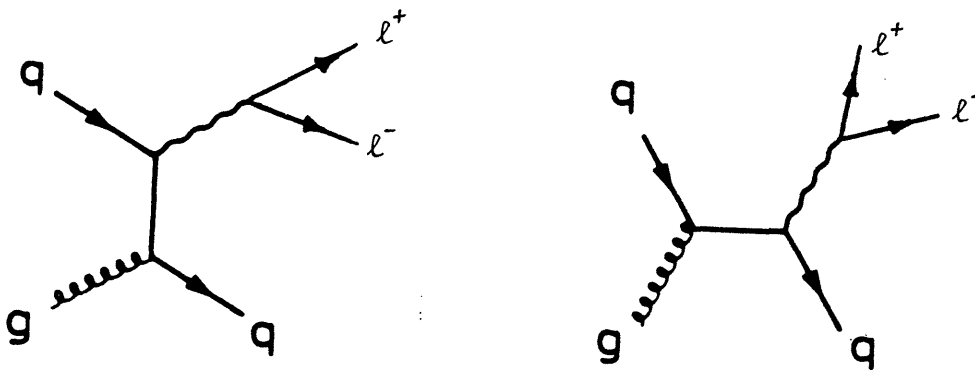
- b) The Drell-Yan Process. A quark from hadron A annihilates with an anti-quark associated with hadron B, forming a timelike photon which decays into the observed lepton pair.

FIGURE I-2

All First-order QCD Corrections to Drell-Yan



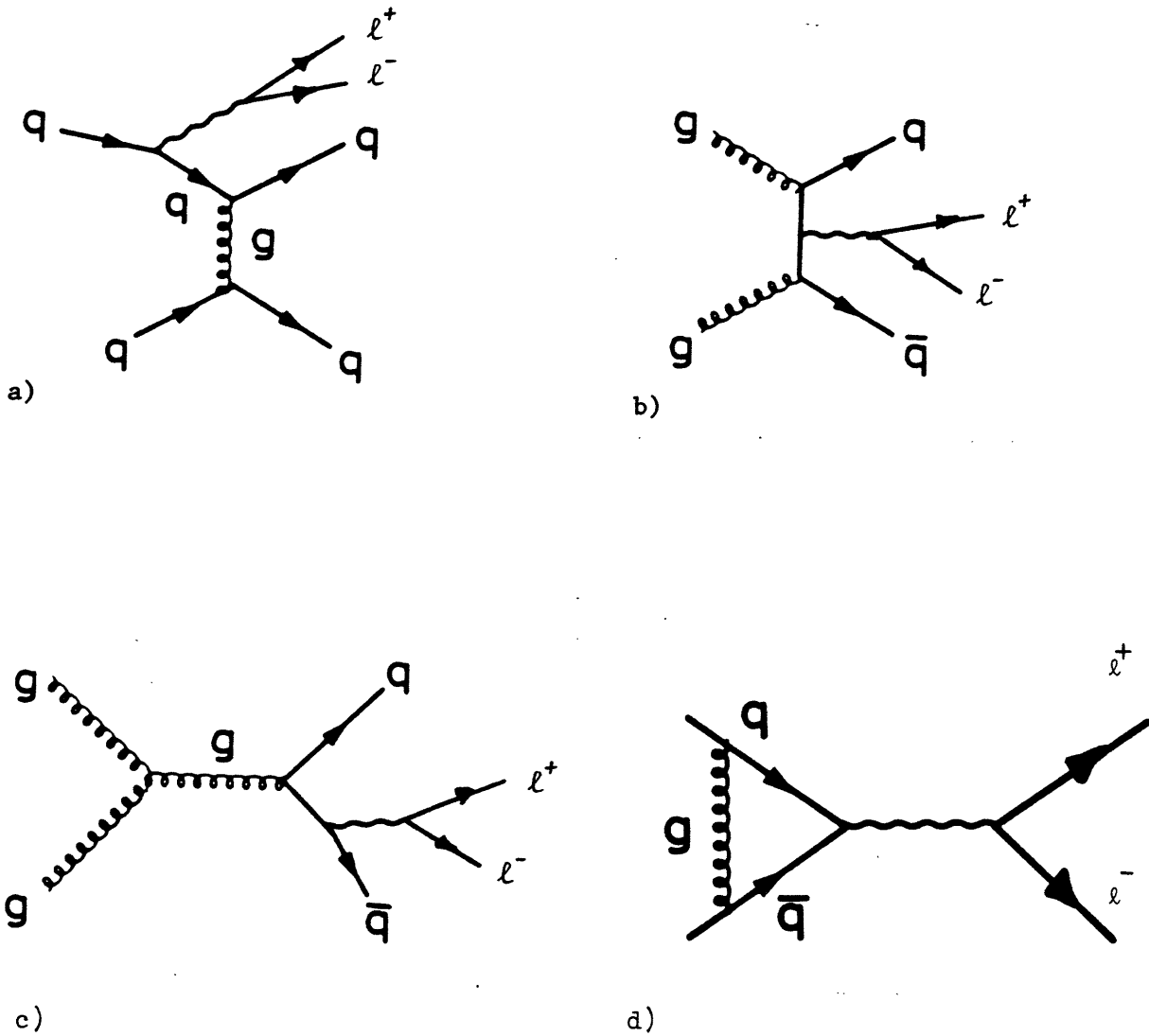
a) The "Annihilation" Process



b) The "Compton" Process

FIGURE I-3

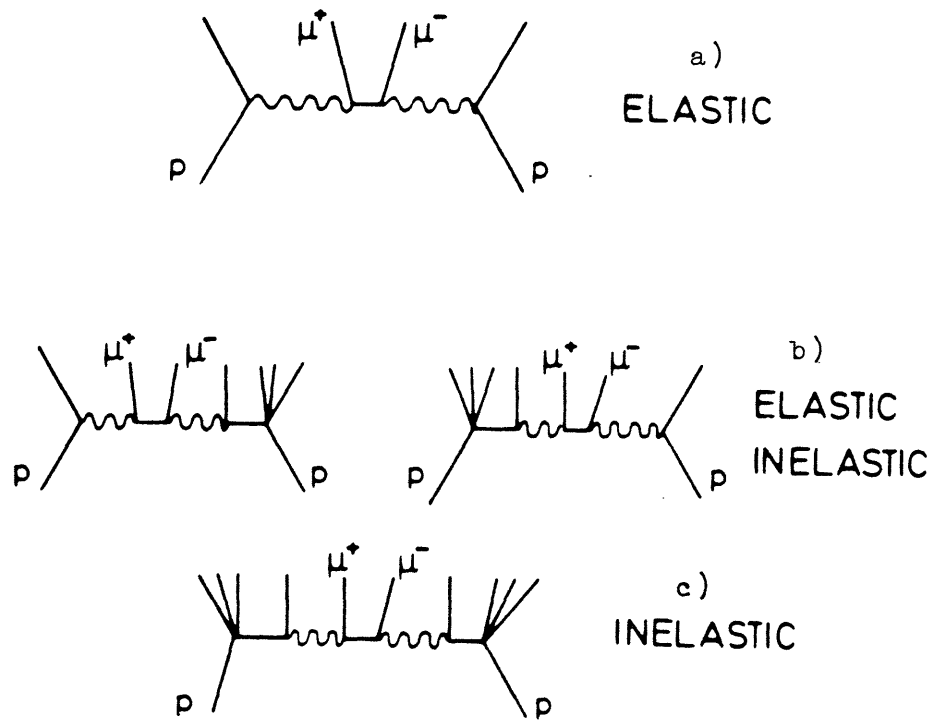
Some Second-order QCD Diagrams for Lepton Pair Production



In figure a), a virtual photon is emitted in the hard scattering between two quarks. In b) and c), the virtual photon arises from gluon-gluon interaction. Figure d) is the QCD vertex correction. All are of second order in α_s .

FIGURE I-4

Muon-Pair Production by the 2γ Process



Part a) depicts the elastic process, where both protons remain intact after scattering. Part b) is semi-elastic; ie. one proton fragments into secondary hadrons after scattering. In Part c), both protons fragment.

SECTION II THE APPARATUS

II-1) The Spectrometer

The spectrometer hardware and data-taking procedures have been described with varying detail in other publications¹⁾ which may be consulted for additional information. Figure II-1 portrays a cutaway view of the spectrometer components, and to lend physical perspective to this drawing, I have included two photographs of the apparatus as installed in intersection two of the ISR (Fig. II-2).

The beamlines and interaction region are surrounded by 7 iron toroids* excited to a relatively uniform magnetic field of 17.5 KGauss[†], which bend and momentum analyze muon tracks in the longitudinal (θ) direction and absorb hadrons accompanying the muon pair. At least 1.3 meters of iron (ie. 7 hadron absorption lengths) lie in the path of a track to prevent background from hadron punch-through. In order to reduce single-muon background resulting from π and K decay, the mean-free path of hadrons is minimized by clustering the iron close (40 cm) to the interaction region and placing a lead plug forward of the intersection to absorb hadrons travelling along the beamlines. The detector accepts muons produced with polar angle $15^\circ < \theta < 120^\circ$ over the full range of azimuth $0 < \phi < 360^\circ$, thus covering 65% of the complete 4π solid angle (see fig. II-3 for angle definitions). Muons are identified by penetration, requiring a minimum of 1.8 GeV momentum to escape the spectrometer.

An array of large drift chambers (total: 192 planes, 800 m² area, 4800 wires) is placed between the magnet yokes and around the detector in order to produce space-points determining the muon tracks and momenta. The resolution of these chambers has been measured to be $\sigma = 430 \mu\text{m}$. Each chamber has 4 planes in order to measure two perpendicular coordinates

*) At the time of the proposal²⁾, it was thought that many events would be produced along the beamline due to a smaller sea-quark momentum in Drell-Yan annihilation, thus the detector was placed asymmetrically about the interaction region to enhance the acceptance at high X_F and cover the forward region down to 15° .

†) The magnetic field has been measured via Hall probes and search coils, and calculated via FATIMA computer simulation (see ref. 3). All methods agree to within 3 percent.

(for example X,Y) with twofold redundancy, ie. 2 planes with drift wires in the X-direction, and 2 planes with wires in the Y-direction. Each of the two planes are offset by one-half of a cell width (5 cm.), such that the drift times recorded at each plane will differ, and the left-right ambiguity can be resolved. The details of chamber construction and testing have been published.⁴⁾ The chambers are precisely surveyed after insertion into the detector, and the survey measurements are verified by fitting cosmic rays through the apparatus and checking the fit residuals. Accuracy of the survey has little effect on the resolution when compared with the contribution due to multiple scattering in the iron.

Inside of the magnet and clustered about the intersection is an array of 136 drift chambers which detect charged tracks produced along with the dimuon. These chambers ⁵⁾ are accurate to 0.3 mm. along the beamline and 2.6 mm. in the transverse direction, and determine tracks emitted within $9^\circ < \theta < 171^\circ$ over all ϕ with 3-5 spacepoints per track. The charged tracks are fitted to a common vertex which is used in the muon reconstruction analysis.

Two telescopes composed of 34 drift chambers surround one of the beamlines downstream of the intersection (see Fig. II-3) and measure charged tracks between $30^\circ \rightarrow 1^\circ$ of ring #1. The details of these chambers are published in ref. 6.

Five scintillator hodoscopes labeled A,B,C,D,E, (see Fig. II-1) are built into the spectrometer in order to define dimuon signatures in the trigger logic and aid in offline track reconstruction. Hodoscope A is composed of 12 scintillation counters placed such that they subtend the entire solid angle covered by the spectrometer; 8 counters coaxially surrounding the intersection region inside of the magnet, and 4 counters perpendicular to the beamplane. Further away from the intersection, hodoscopes B and D are coaxial with the beamline; B is made of 23 counters placed between the magnet yokes after 50 centimeters of iron, while D contains 26 counters 4 meters in length and surrounding the periphery of the magnet. Hodoscopes C and E are perpendicular to the beamplane and cover 360° in equi-angular segments centered on the beam axis. Hodoscope C contains 24 elements positioned forward of the intersection between yokes 2a and 2b, while E is made of 48 counters

(up to 3 meters in length) surrounding the beampipes at the front of the magnet. Hodoscopes D and E register muons exiting the detector, B and C indicate muons traversing the detector, and the A hodoscope, which is placed before the absorber, is also sensitive to other charged particles produced in the interaction.

There is one fast photomultiplier on each end of the D counters. Both outputs are recorded by TDC's, and the difference in time between the ends gives the location along the counter traversed by the muon to within 25 cm., which serves as a validity check on the chamber data. Outputs from both phototubes of each D-counter are combined to form one composite signal which is used in the triggering logic.

II-2) The Triggering System

The B,C,D, and E hodoscopes are positioned such that they divide the ϕ -plane into 24 equiangular sectors (see Fig. II-4). Since the magnet is toroidal about the beam axis, there is no bending of the muon tracks in the ϕ -projection (ie. front or back view), and the tracks are mapped onto straight lines. The 24 ϕ -sectors are centered on the intersection region; hence, allowing for large multiple scattering in the iron, a muon track will always be within 2 of these sectors.

A muon signature is defined in the trigger by a coincidence of one D or E counter with its corresponding (or adjacent) B or C counter respectively. Two such muon signatures are required by the trigger. Since background due to beam-spray and accidentals is considerable (typical rates for the counters run 10 \rightarrow 30 Khz), further conditions were introduced into the trigger hardware:

- 1) The two candidate dimuons are required to be opposite one another in the ϕ -plane within ± 3 hodoscope sectors (ie. the tracks form an angle in ϕ of $180^\circ \pm 50^\circ$). This eliminates false triggering due to beam gas and renegade protons which saturate portions of the apparatus with coincidences.
- 2) All D-counter signals must arrive within 8 nsec of each other. Cosmic rays passing through the D-hodoscope are at least 16 nsec out of time, hence are suppressed by this cut.

At this point, a fast trigger signal exists in the hardware which can be cleared or inhibited by the following additional restrictions:

- 3) Sets of anti-counters are placed along the two beamlines (see Figs. II-3 and II-4). Coincidences are formed between the downstream and delayed upstream signals on each beam that indicate a beam-halo or beam-gas event and apply a veto signal to the electronics which clears the trigger.
- 4) At least two of the inner A counters must fire. This requirement indicates that a beam-beam interaction has indeed taken place in the intersection.
- 5) The online computer system must be ready to accept an event.

At this point, an interrupt is sent to a microprocessor acting as a buffer between CAMAC and the on-line PDP-11/45 computer. The microprocessor reads the hodoscope TDC information and applies the following additional cuts via software:

- 6) If the D-hodoscope was hit by both tracks, timing cuts are applied to the traversed counters to eliminate out-of-time cosmic rays escaping hardware requirement 2 listed above.
- 7) The back-to-back requirement (called " ϕ -matching") described earlier in paragraph 1 is enforced more stringently and applied to the inner (B and C) as well as outer (D and E) hodoscopes.*
- 8) The drift chamber TDC's are read, and coarse spacepoints are determined by pairing all hit perpendicular wires in each chamber can (no time information is analyzed). At least 6 such spacepoints are required in the detector to insure reconstructability in a more detailed off-line analysis.† This is the most restrictive cut applied to the trigger.

*) Hardware requirement 1 actually allows a separation in ϕ of $180^\circ \pm 4$ sectors for the inner (B and C) hodoscopes; in the microprocessor this allowance is reduced to ± 3 sectors.

†) 8-12 spacepoints are present in a typical event.

No further trigger rejection is attempted, and the hodoscope, drift chamber, and vertex detector information is transferred to a buffer system in the online computer memory which is periodically flushed to magnetic tape. In addition to trigger data, the scaler rates, ISR functional data, and TDC calibrations are written out to tape during the course of a run. The scalers are sampled every 10 seconds.

The trigger conditions discussed above are presented in table II-1, along with typical rate attenuations applied by each cut. Starting with a "raw" trigger rate of $50 \rightarrow 300$ hz (after cuts 1 and 2), only $1 \rightarrow 5$ events are written on tape per second.

II-3 Reconstruction, Resolution, and Acceptance

Figure II-6 shows a computer-reconstructed picture of a typical dimuon event in the spectrometer of mass 5.3 GeV. Each track is well-fitted with four chamber spacepoints, and we see no other "sporadic" hits in the chambers; a testimony to the effectiveness of the iron absorber. The difference in D-counter timing between both tracks is under 1 nanosecond, indicating that they arose from a beam-beam interaction. We see a well-fitted vertex in the inner detector and 8 charged tracks accompanying the dimuon (tracks derived from the forward telescopes are not portrayed in these pictures). There is evidence of inner-detector tracks and spacepoints following the trajectories of the muons found in the outer-detector, thereby "linking" both systems.

Figure II-7 is a picture of a dimuon event of mass 10.1 GeV fitted at an unusually high transverse momentum of 6.4 GeV. Track #2 penetrates the side of the detector with very high momentum (thus displays little curvature), while track #1 bends as it goes forward (thus is much softer). There are many associated particles in the inner-detector, and we again see good linking to the muon tracks extrapolated from the outer-detector.

An extensive Monte-Carlo program was developed to simulate and analyze detector behavior. This program accurately models the detector geometry and accounts for counter/chamber efficiency, δ -ray production, and the trigger constraints described previously. Muon tracks are propagated through the yokes accounting for the magnetic field, multiple scattering, and energy loss in the iron. The production mechanism generates Monte-Carlo events such that their distributions in mass,

transverse momentum (P_t), Feynman-X (X_F), and the Collins-Soper polarization ($\cos\theta_{CS}$) of the dimuon match that of the data (see Section III-6 ; these parameters are defined in Appendix I). A total of 1.5 million events were generated between masses of 3 and 25 GeV, and 32,000 events (2.1%) were accepted by the analysis.

The acceptance of the detector is derived from this Monte-Carlo by investigating the ratio of accepted and fitted events over the actual number of originally generated events as a function of the parameter in question. Figure II-8 shows the detector acceptance as a function of mass, P_t , X_F , and $\cos\theta_{CS}$ (the last three are plotted for 4 different mass regions). The curves are smoothed interpolations of histograms, each bin of which is calculated as:

$$\frac{N_{fit}}{N_{gen}} \quad \text{where:} \quad \begin{array}{l} N_{fit} = \text{Number of events fitted within} \\ \quad \quad \quad \text{bin limits.} \\ N_{gen} = \text{Number of events generated within} \\ \quad \quad \quad \text{bin limits.} \end{array}$$

The use of the fitted values in the numerator vs. generated values in the denominator also accounts for resolution effects.

Due to the minimum requirement of 1.8 GeV momentum for a track to escape the detector, events with mass less than approx. 2.8 GeV cannot be observed. The effects of this cutoff are evident in Figure II-8 (a), where we notice the acceptance abruptly drop two decades between masses of 8 and 4 GeV. In order to penetrate the detector, events in the J region (2-4 GeV) must be produced forward with $0.1 < X_F < 0.35$ and muon momenta of 3-5 GeV. This is obvious in Figure II-8 (b), where we see a very narrow window of acceptance in X_F (centered at 0.2) at low mass widen progressively with increasing mass. This phenomenon is also noticeable in the transverse momentum acceptance (Fig. II-8 (c)). At low mass we notice a cutoff at high P_t ($P_t > 2$ GeV) where the dimuons have little extra energy to fuel an additional transverse kick; depriving momentum from one muon in order to boost the momentum of the opposite track and increase the P_t will prevent the softer track from escaping the magnet. This cutoff increases with mass, until at higher mass regions ($m > 8$ GeV) we see the inverse effect; an acceptance decrease at low P_t , which is due to the detector assymetry. Muons travelling forward at very low θ_μ (see Fig. II-3) can escape through the 15° gap between the beamlines and magnet yokes, which causes the decline in acceptance with increasing $\cos\theta_{CS}$ (Fig. II-8 (d)).

The spectrometer resolution is limited primarily by multiple scattering of the muons in the iron yokes. An estimate of the resolution is understood via an elementary analysis. Given:

Eq. II-1) $\theta_B = \frac{0.03(B\ell)}{P}$ θ_B = Bending angle of muon track in magnet
 $\Delta\theta_{MS}$ = Expected deviation in track trajectory due to multiple scattering

Eq. II-2) $\Delta\theta_{MS} = \frac{0.015}{P} \sqrt{\frac{\ell}{\ell_0}}$ B = Magnetic field strength (KGauss)
 P = Momentum of track
 ℓ = Amount of magnetized iron traversed by track (cm.)
 ℓ_0 = Radiation length of traversed material (cm.)

Since momentum is determined via track bending, we assume:

Eq. II-3) $\frac{\Delta P}{P} = \frac{\Delta\theta_{MS}}{\theta_B} = \frac{0.5}{B\sqrt{\ell \cdot \ell_0}}$ (From II-1 and II-2 above)

We see this uncertainty in momentum to be independent of P .

Plugging in an average length traversed in the spectrometer:

and: $\langle \ell \rangle = 1.7$ meters
 $B = 17.5$ KGauss
 $\ell_0 = 1.76$ cm. (for iron)

yields:

Eq. II-4) $\frac{\Delta P}{P} = 15\%$

The mass of the dimuon can be expressed in terms of the momenta (P_1, P_2) and opening angle ($\theta_{\mu\mu}$) of the muons:

Eq. II-5) $M_{\mu\mu}^2 = 4P_1 P_2 \cdot \sin^2\left(\frac{\theta_{\mu\mu}}{2}\right)$

The momentum uncertainty quoted in Eq. II-4 above yields a mass resolution of *:

*) The measuring error in $\theta_{\mu\mu}$ is much less than that in P , thus we ignore it in this approximation.

$$\text{Eq. II-6)} \quad \frac{\Delta M}{M} = \frac{1}{\sqrt{2}} \cdot \frac{\Delta P}{P} = 11\% \quad \underline{\text{Independent of mass!!}}$$

A value of $\Delta M/M = 10.8\%$ has been obtained by observing the 770 MeV width of the narrow J resonance (see Fig. II-9). By comparing the upper and lower halves of cosmic rays fitted through the detector (while accounting for energy loss in iron), we also obtain a similar resolution.

The above analysis can also be adapted to transverse momentum. Since the P_t of the dimuon is the sum of the transverse components of each muon momentum, we can crudely estimate the order of the error:

$$\text{Eq. II-7)} \quad \frac{\Delta P_t}{P_t} \approx \sqrt{2} \frac{\Delta P}{P} = 21\% \quad \text{From Eq. II-4}$$

The Monte Carlo program described earlier can be used to estimate detector resolution, and the results are presented in Figs. II-10 thru II-13. Here we fit a gaussian distribution to histograms filled with the difference between fitted and generated values of a parameter divided by the generated value of the parameter, and the σ of the gaussian reflects the resolution. This is done for mass, P_t , X_F , and $\cos\theta_{cs}$ using Monte Carlo events in four different mass ranges. In the higher mass bins, the lack of statistics in the Monte Carlo causes coarse distributions which yield greater uncertainty in the gaussian fit. This is reflected in the size of the error bars plotted with the resolution values in the figures. The Monte Carlo distributions in mass, X_F , P_t , and $\cos\theta_{cs}$ have been reweighted (See Sec. III-6) to be flat in order to avoid any skews in the gaussians.

Our previous approximations are supported; we see a mass resolution of 10% fairly constant with mass in Fig. II-10, and P_t resolution changing from 17% to 30% with mass (averaging at about 20%, since most events are at lower mass) in Fig. II-11. Resolution in X_F (Fig. II-12) seems fairly constant with mass at about 10%, while the $\cos\theta_{cs}$ resolution (Fig. II-13) improves considerably with mass (again a geometrical effect) from 14% to 2.6%.

II-4 Luminosity Measurement

Luminosity is monitored during runs simultaneously by two completely independent systems which are displayed schematically in Fig. II-5. The first method employs the W,X,Y, and Z counters* grouped about the outer beampipe sections. A coincidence of upstream counters W and Z with delayed downstream counters X and Y is used to define a beam-beam event rate:

$$\text{Eq. II-8) } BB_1 = (W \cdot X_{\text{delayed}}) \cdot (Z \cdot Y_{\text{delayed}})$$

This BB signal is proportional to the instantaneous luminosity, and is recorded on tape during a run.

The second system uses the H3-H4 hodoscope arrays placed about the inner beampipe sections. An analogous coincidence is defined:

$$\text{Eq. II-9) } BB_2 = (H4_L \cdot H3_{L_{\text{delayed}}}) \cdot (H4_R \cdot H3_{R_{\text{delayed}}})$$

This signal is monitored via scalers and periodically recorded in the logbook during a run. An accidental rate is derived for this system by eliminating the delay in H3 in Eq. II-9, thus mistiming the coincidence. This signal is proportional to accidentals in the system, and is subtracted from BB_2 to form the corrected beam-beam rate.

Counters W,X,Y,Z,H3, and H4 can be seen positioned in Fig. II-3. Both monitor systems are calibrated by the "Van Der-Meer" method, where low-current beams are injected into the rings and displaced vertically from each other in precise steps, allowing one to deduce their relative heights⁷⁾. This enables the absolute luminosity (L) to be calculated, which can be compared with the recorded BB rates, allowing a constant "K" to be determined such that:

$$\text{Eq. II-10) } L (\text{cm}^2/\text{sec}) = K \cdot BB$$

Such calibrations are made periodically to observe and account for counter aging and other system perturbations.

The luminosity values from both systems were laboriously transferred from the logbooks to computer files† where they were analyzed for

*) These counters, with different delays introduced, also serve as the anti-counters described in Section II-2.

†) Even though BB_1 is recorded on the data tapes, it is compared with values listed in the logbooks to intercept scaler readout errors.

consistency. Figure II-14 shows the average luminosities resulting from both systems* for each run taken between 1977 and 1979. We see that the MIT luminosity is persistently higher than that taken via the Pisa monitors, possibly because the MIT monitors are much more sensitive to beam background conditions.† Three pieces of evidence attest to this background dependence:

- 1) We have noticed finite correlations between the beam veto rate and BB_1 .
- 2) The constant K in Eq. II-10 varies appreciably between calibrations of the MIT monitors.
- 3) Between runs 45 and 80 of Fig. II-14 (b), we see an abrupt factor 2 increase in MIT luminosity, while Pisa value remains unaffected. During these runs, much lead was removed from the beamlines which shielded against beam-halo, causing an increase in background and counter rates which raised BB_1 .

Since the Pisa values do not show such a background dependence, they are used in the analysis, and a comparison with the corresponding MIT values determines a systematic error in luminosity measurement of about 6%. The differential luminosity for each run is multiplied by the accumulated gated-clock time and integrated for each beam energy.

Figure II-14 also exhibits other interesting features. A periodic ramp-like behavior can be noticed in the luminosity; this occurs at each ISR fill, since currents are most intense at the beginning of the fill and gradually decay. The average luminosity seems to rise slowly in Fig. II-14 (a) from $8 \times 10^{30} \text{ cm}^{-2}/\text{sec}$ at run #0 to nearly 2×10^{31} at run #800; this is due to improvements in the ISR performance and maximum current capacity between 1978 and 1979.

*) In this figure, the monitor systems are named after their parent institutions, ie. System #1 (W,X,Y,Z counters) are "MIT monitors", while System #2 (H3, H4) are "Pisa monitors".

†) The accidental signal subtracted from BB_2 which assists in compensating for background is not recorded for BB_1 .

SEC. II REFERENCES

- 1) D. B. Novikoff, Thesis, MIT (1979).
D. Antreasyan et. al., Phys. Rev. Lett. 45, 863 (1980).
D. Antreasyan et. al., CERN-EP/79-116 (1979).
- 2) U. Becker et at., Proposal, CERN/ISRC 73-28 (1973).
- 3) Ch. Iselin, Notes on the Use of the Computer Program FATIMA,
CERN internal report.
- 4) U. Becker et al., Nuc. Inst. and Methods, 128, 593 (1975).
- 5) A. Bechini et al., Nuc. Inst. and Methods, 156, 181 (1978)
See also: V. Cavaasinni, Thesis, Scuola Normale Superiore, Pisa (1978).
- 6) F. Carbonara et al., Nuc. Inst. and Methods, 171, 479 (1980).
- 7) S. Van der-Meer, "Calibration of Effective Beam Height in the ISR,"
CERN Internal Report ISR-PO/68-31 (1968).

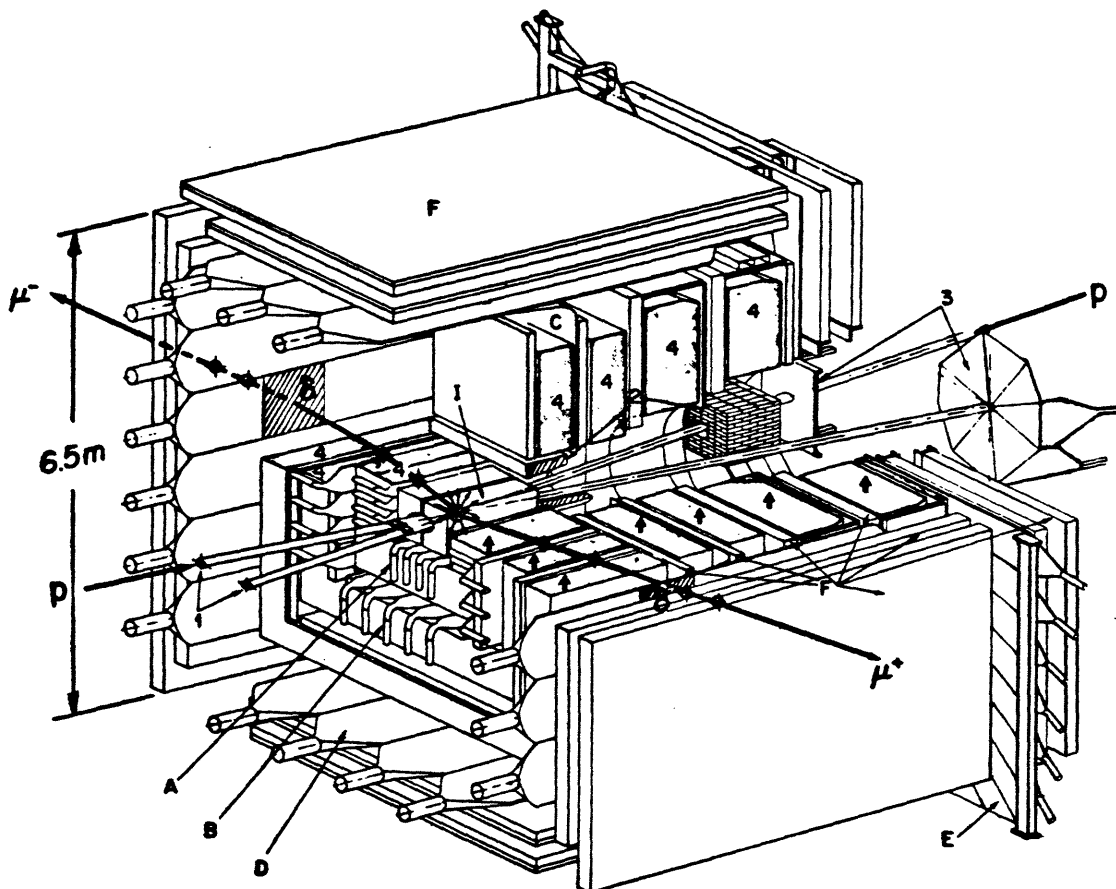
TABLE II-1 TRIGGER QUALIFICATIONS

Cut Number (referenced in text)	Description	% <u>PASSED</u> by each cut
1 - 2	Raw dimuon trigger containing hardware ϕ -match of hodoscopes and D-counter timing requirement.	-----
3, 5	Beam veto supplied via anticounters. Computer-ready gate.	50%
4	At least 2 A-counters present to guarantee beam-beam interaction.	70%
6	Cosmic Ray Reject test applied to D-counter timing via microprocessor.	90%
7	ϕ -match requirement re-enforced by microprocessor.	50%
8	At least 6 coarse spacepoints found in the chambers.	15%
- TOTAL -	All cuts together	2% <u>PASSED</u>

Thus 98% of all raw triggers are REJECTED

NOTE: The effectiveness of various cuts depends upon beam conditions. These percentages represent typical values during an average ISR run. The cuts are listed in the order applied to the trigger.

FIGURE II-1 THE SPECTROMETER - CUTAWAY VIEW

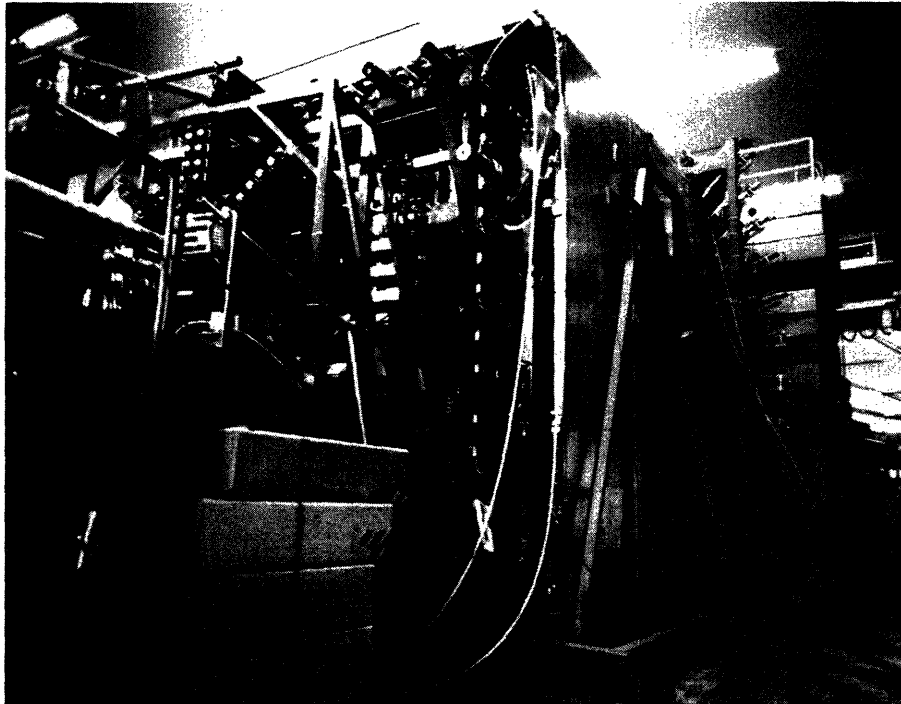


LEGEND:

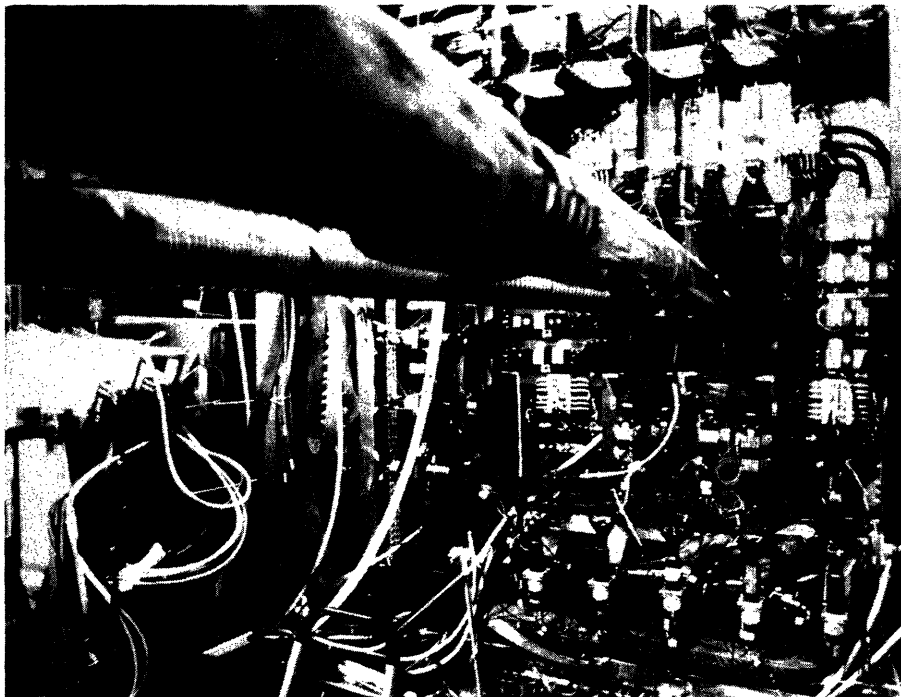
- 1) Beam pipes
- 2) Lead absorbers
- 3) Luminosity and beam-veto monitors
- 4) Magnitized iron toroids
- A) Inner hodoscope (there are 2 sets of A counters; the set described in the text is not shown)
- B,D) Trigger hodoscopes coaxial with beamline
- C,E) Trigger hodoscopes perpendicular to beamline
- F) Drift chambers for muon detection
- I) Interaction region and vertex detector

The computer reconstruction of an event with mass 24.5 GeV and $P_t = 1.2$ GeV is superimposed over the drawing. Chamber spacepoints are denoted by circles, and the shaded areas labeled " δ " represent the D-hodoscope interception points determined to within 25 cm.

Figure II-2.



a) View of the dimuon spectrometer. Outer drift chambers and D-counter photomultipliers can be seen (center), and part of the E-hodoscope is visible in front of the concrete wall at right.



b) Beamlines and intersection region (the vertex detector is removed). The magnet encloses the intersection, and portions of the A and B hodoscopes can be seen mounted on the magnet and protruding from the gaps between yokes.

Figure III-3. THE DETECTOR – OVERHEAD VIEW

- Yoke 1 – Yoke 4: Magnetized Iron Yokes
 [Hatched Box] : Muon Detection Chambers
 T1, T2: Chamber Telescopes
 B, C, D, E: Trigger Hodoscopes
 W, X, Y, Z: Luminosity/Veto Counters
 H3, H4: Luminosity Hodoscopes
 H2: Downstream Hodoscope
 P, SP, SU: ISR Vacuum Pumps
 F, T: ISR Magnets

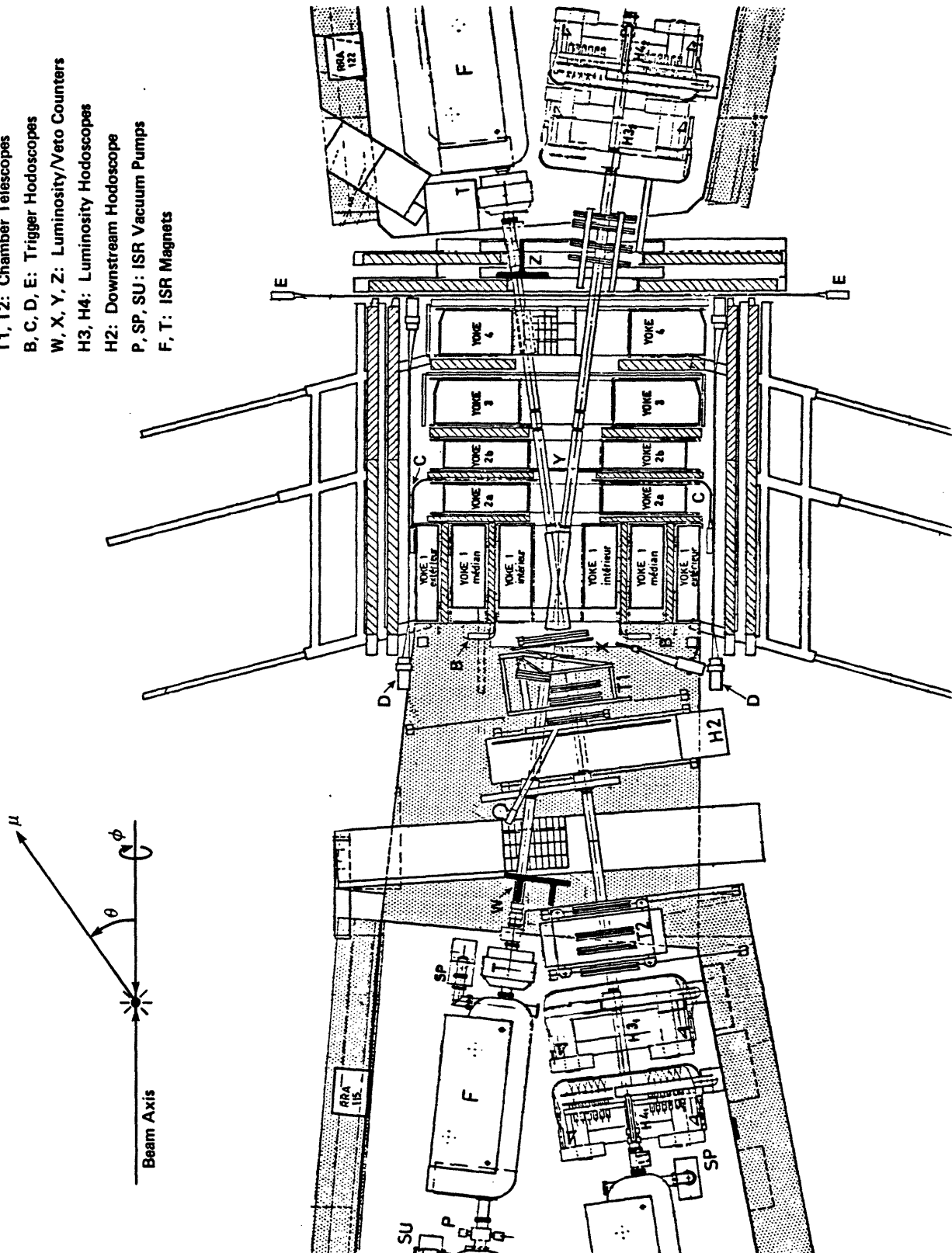
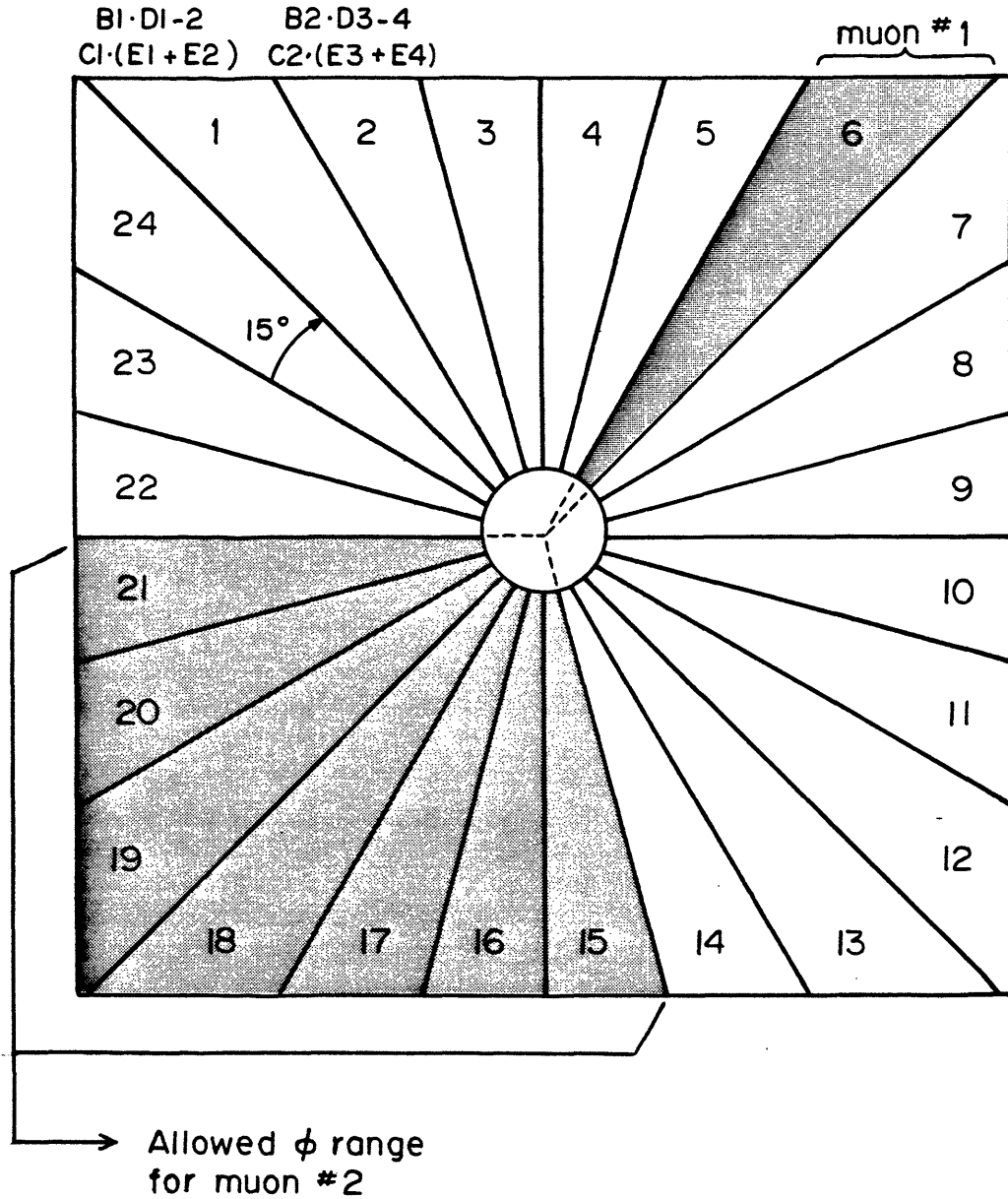


Figure II-4 Hodoscope Sectors formed in the ϕ -Projection



This figure depicts the 24 sectors formed in the ϕ -projection (orthogonal to the beamline) by the hodoscopes and used in the trigger logic. Coincidences of the component counters are given for the first two sectors; the rest follow in similar fashion. All dimuon candidates must be back-to-back within ± 3 sectors to be accepted by the trigger; the shading in the figure portrays an example.

Figure II-5 Luminosity Monitors and Veto Counters

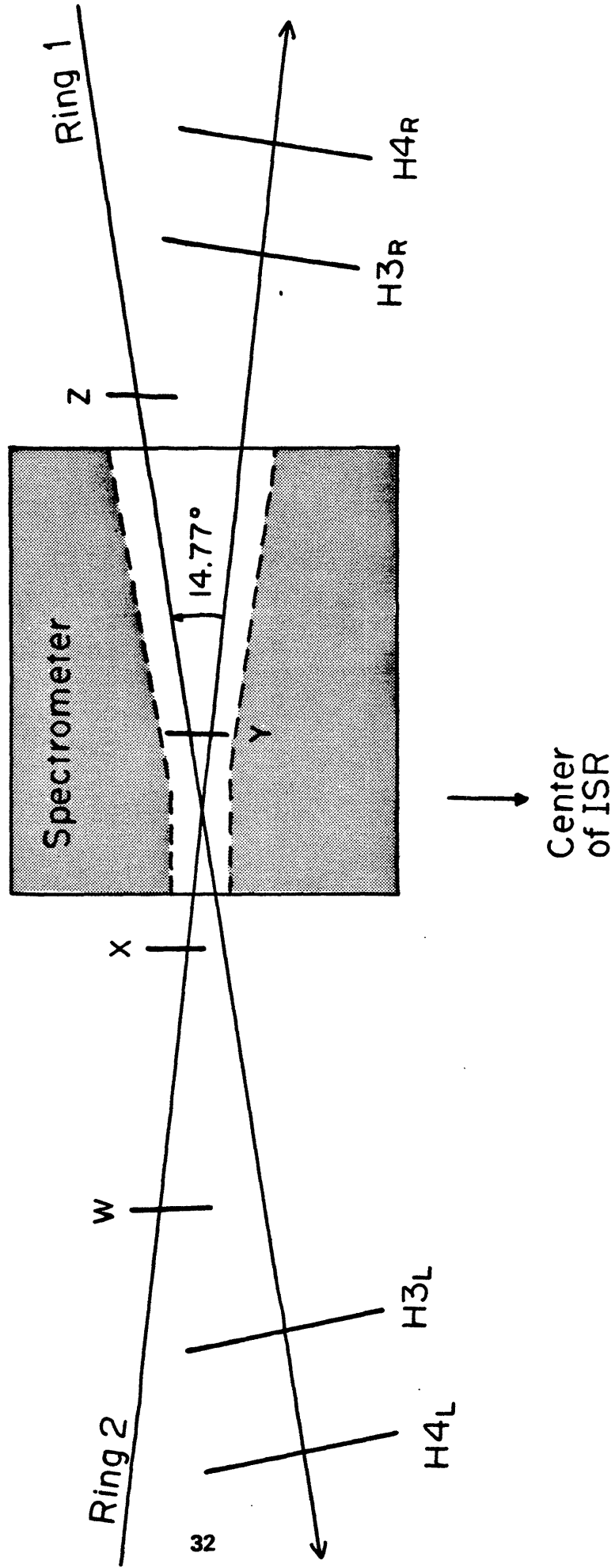
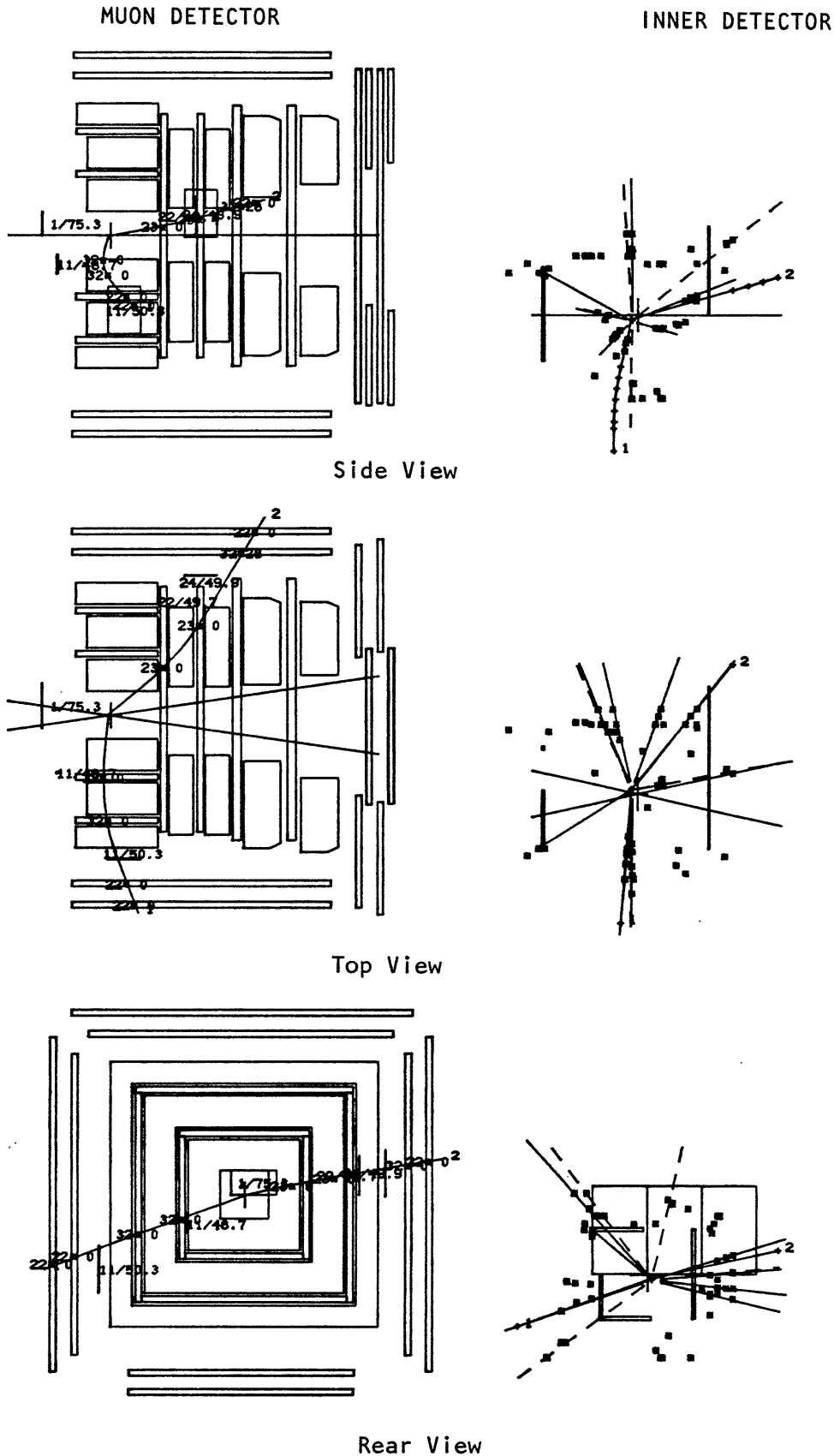


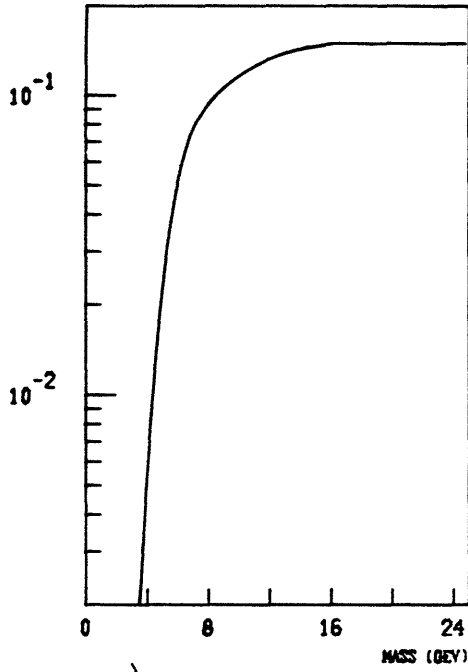
FIGURE II-6 A TYPICAL RECONSTRUCTED EVENT



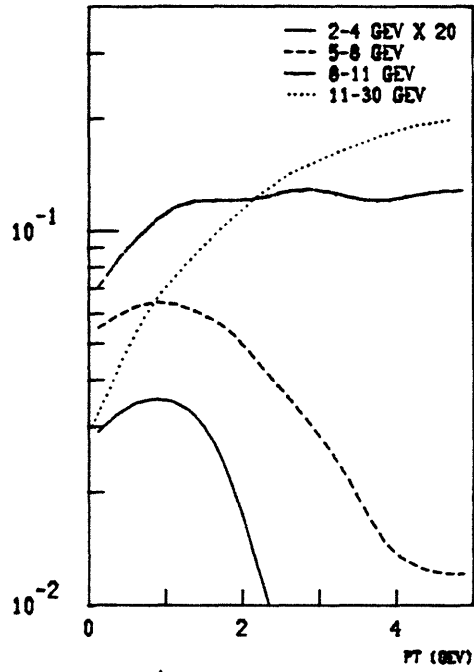
RUN NO 826 EVENT 120
 MASS= 5.338 PPERP= 0.529 XF=0.068
 P1= 2.76 X1= 1.14 P2= -3.06 X2= 1.18
 BDL1= 25.26 BDL2= 23.75

FIGURE II-8 DETECTOR ACCEPTANCE

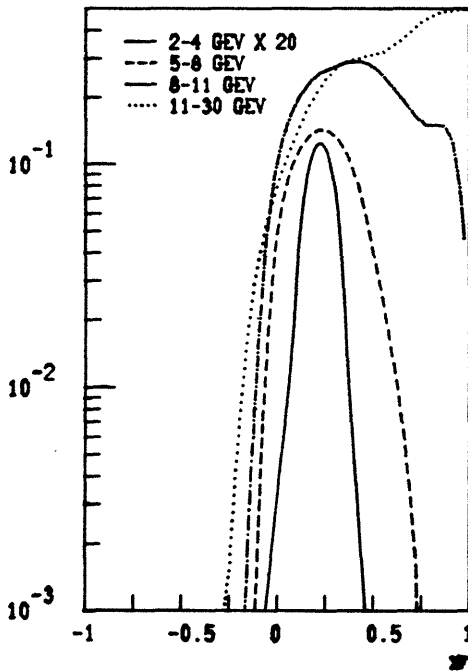
$\sqrt{s} = 62$ GEV MONTE-CARLO WEIGHTING



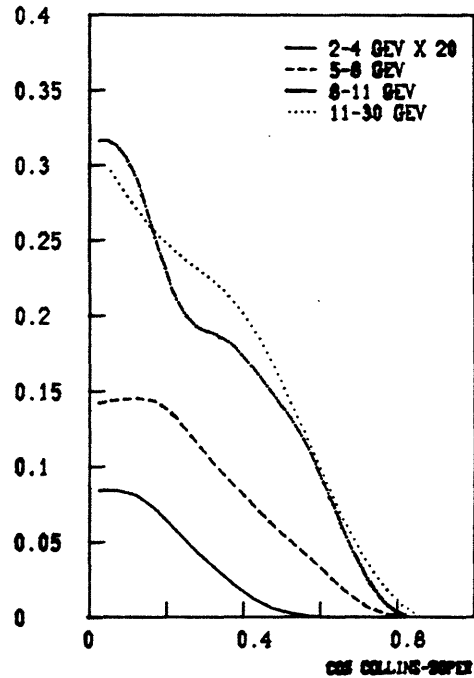
a) MASS ACCEPTANCE



c) PT ACCEPTANCE



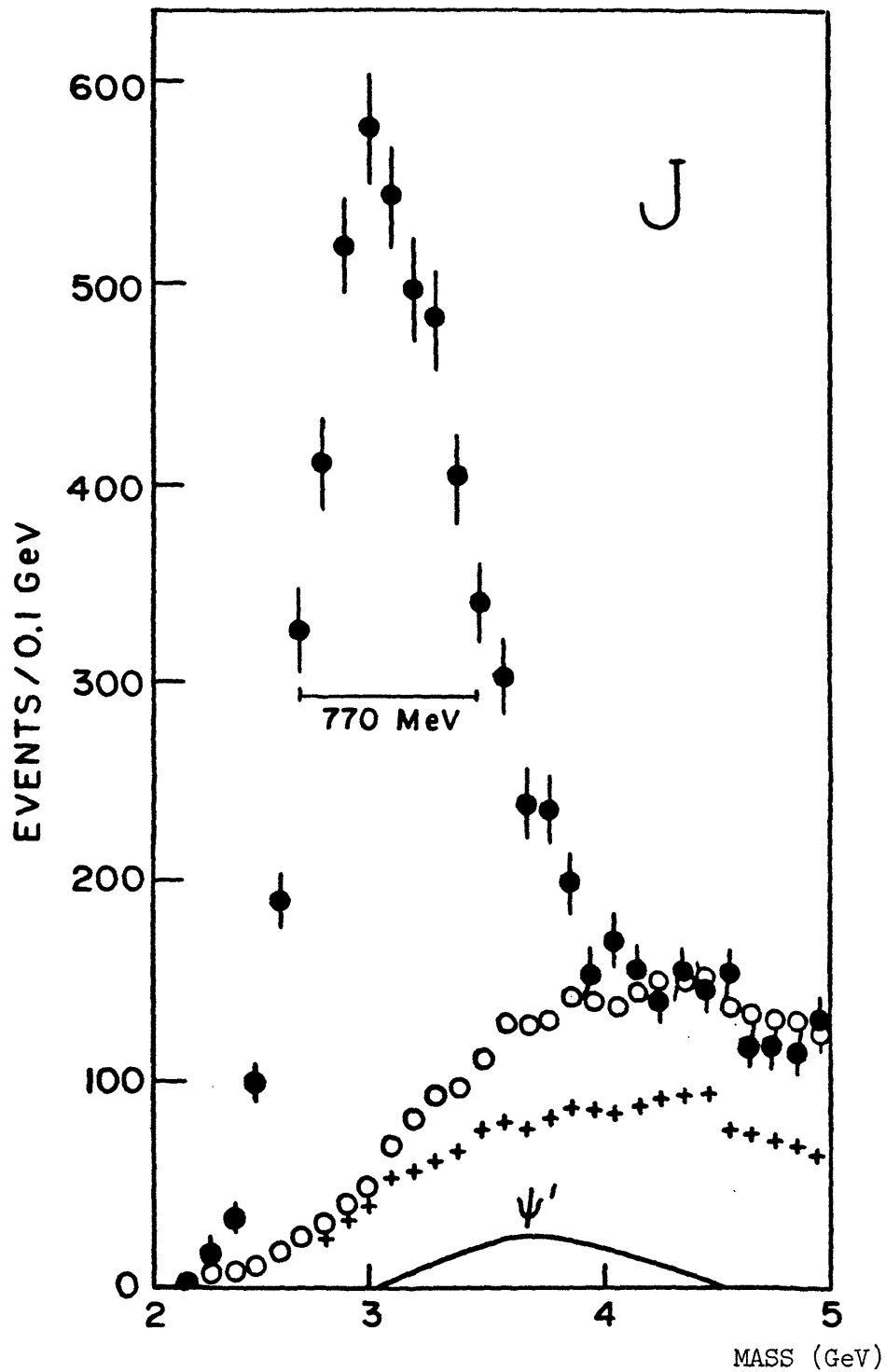
b) XF ACCEPTANCE



d) COS COLLINS-SOPER ACCEPTANCE

Parts b, c, and d portray acceptance within the mass ranges listed in the legends.

FIGURE II-9 THE J RESONANCE



- = Accepted $\mu^+\mu^-$ events
- + = Background events estimated from $\mu^+\mu^+$ and $\mu^-\mu^-$ distributions (see Sec. III).
- = Sum of Drell-Yan continuum fit, $\psi' \rightarrow \mu^+\mu^-$ (solid line), and background.

The 770 MeV width of the J reflects the 10.5% mass resolution.

FIGURE II-10 MASS RESOLUTION

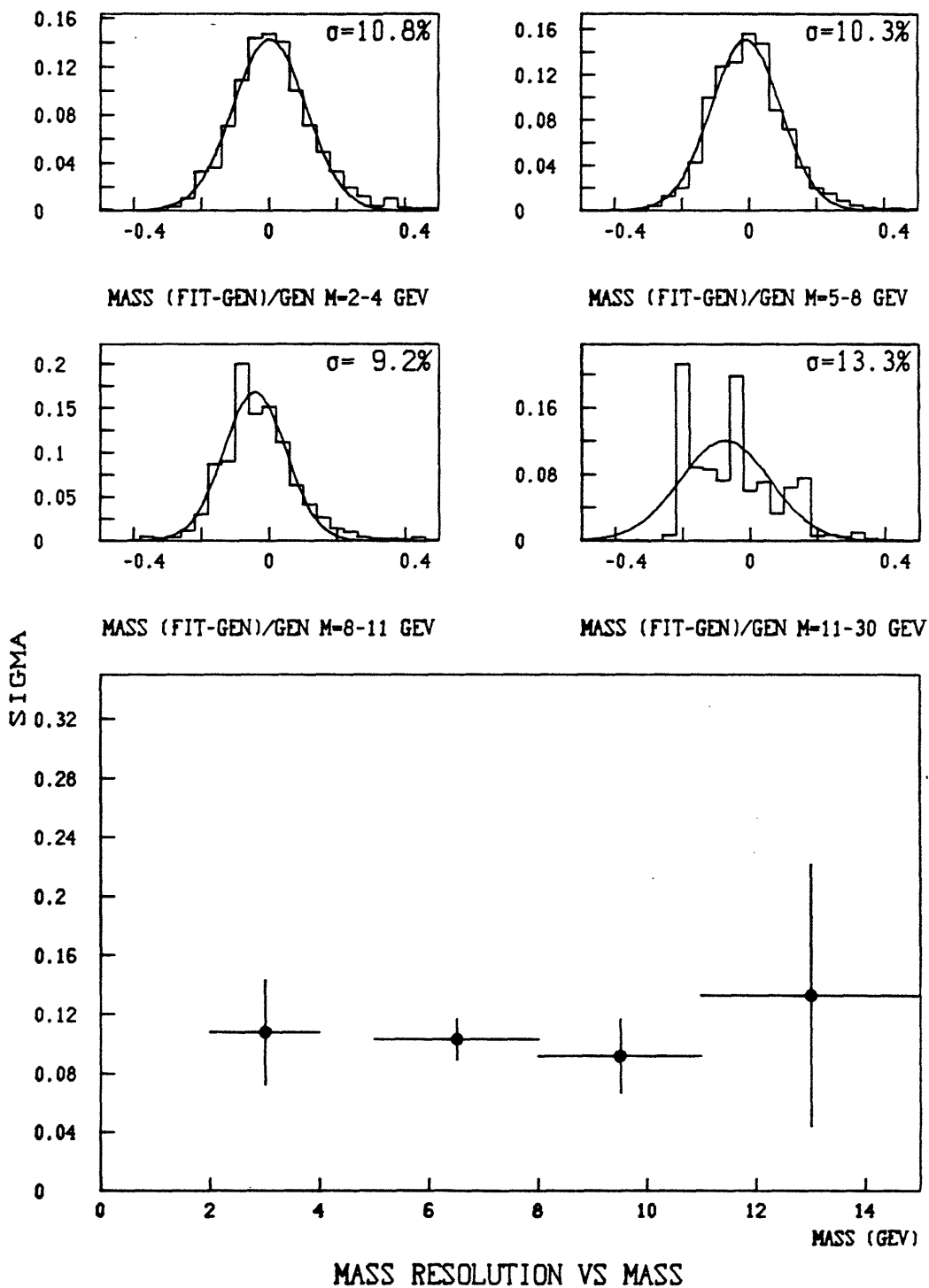


FIGURE II-11 P_T RESOLUTION

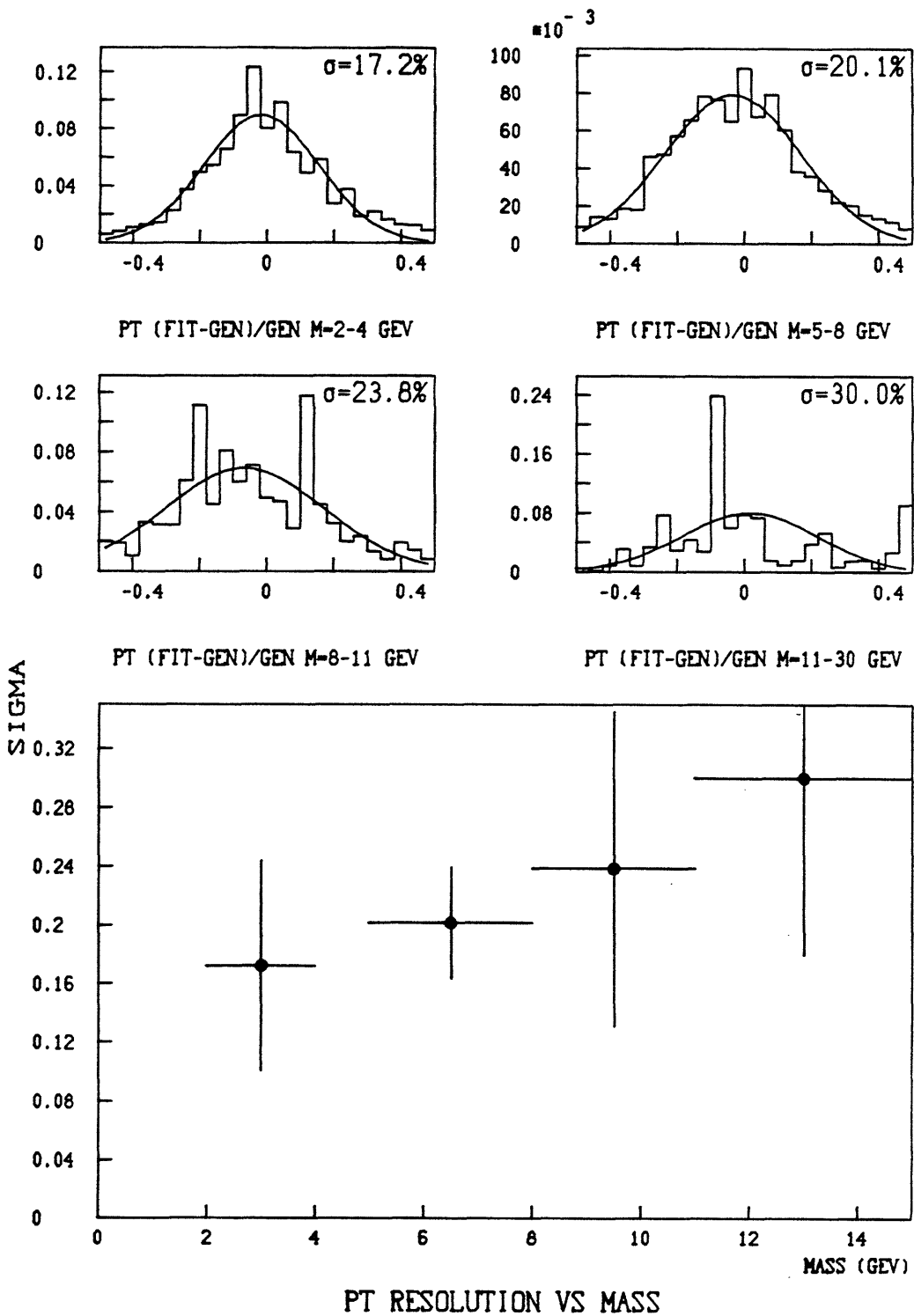


FIGURE II-12 X_F RESOLUTION

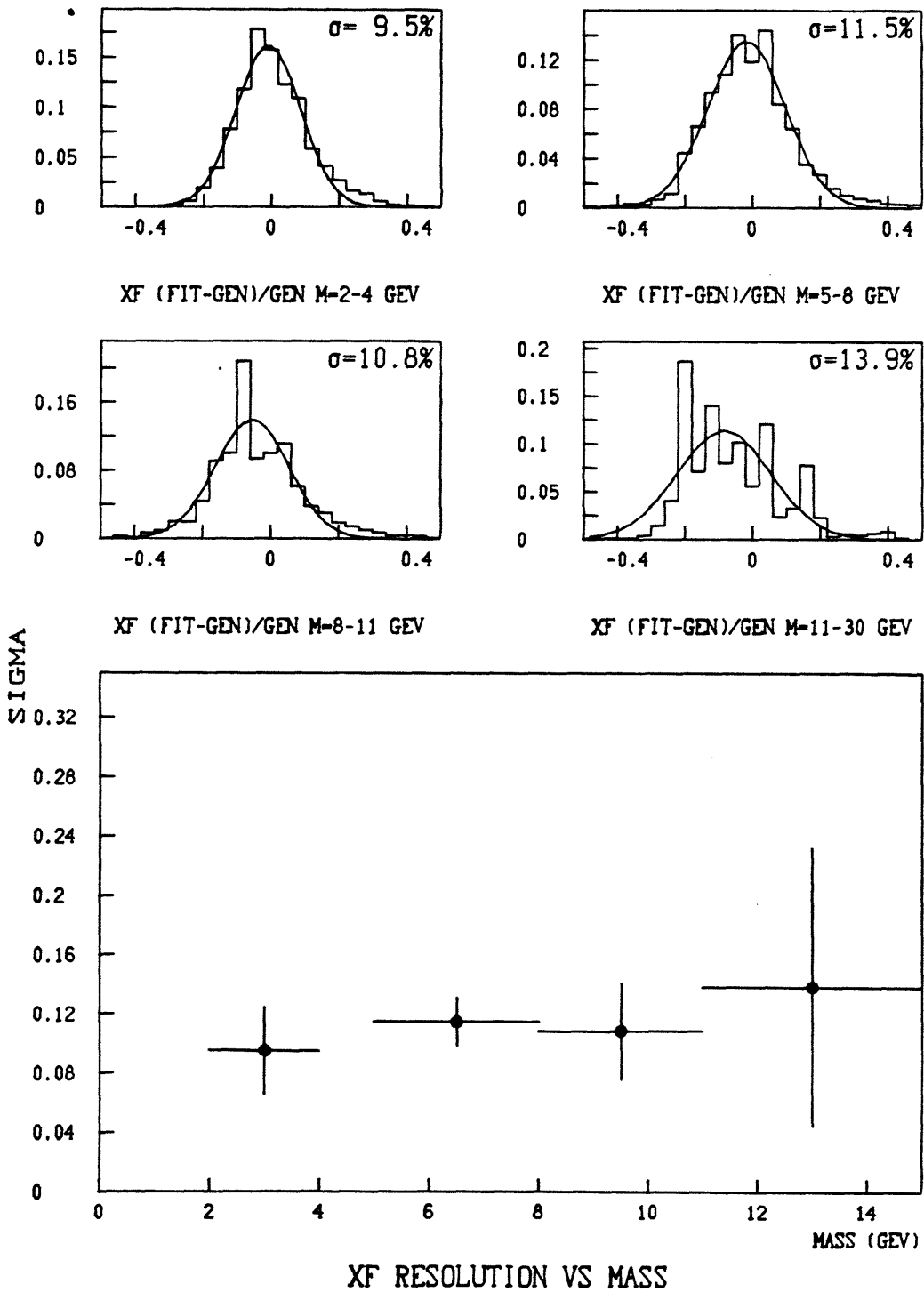


FIGURE II-13 $\text{COS}(\theta)_{\text{CS}}$ RESOLUTION

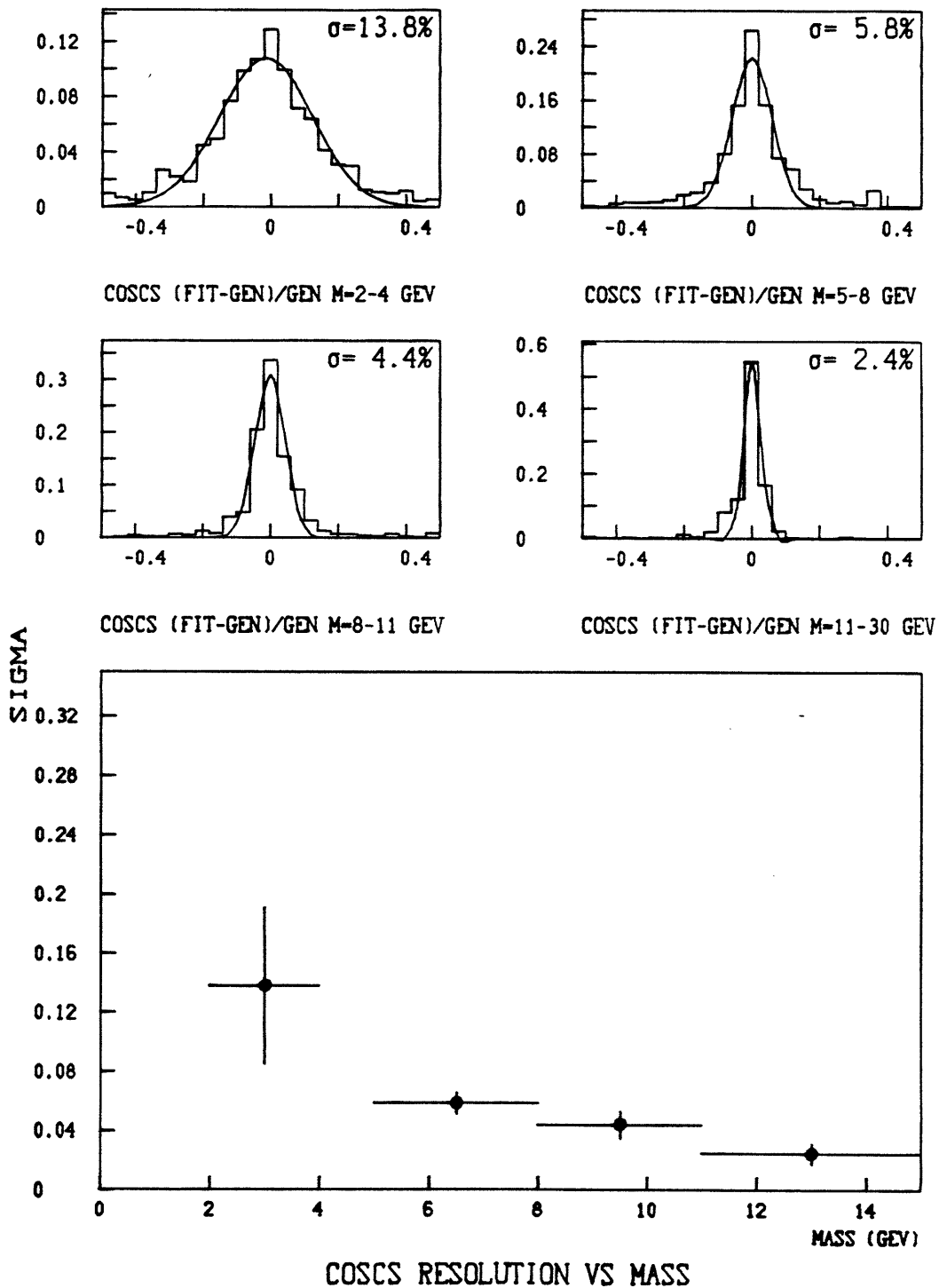
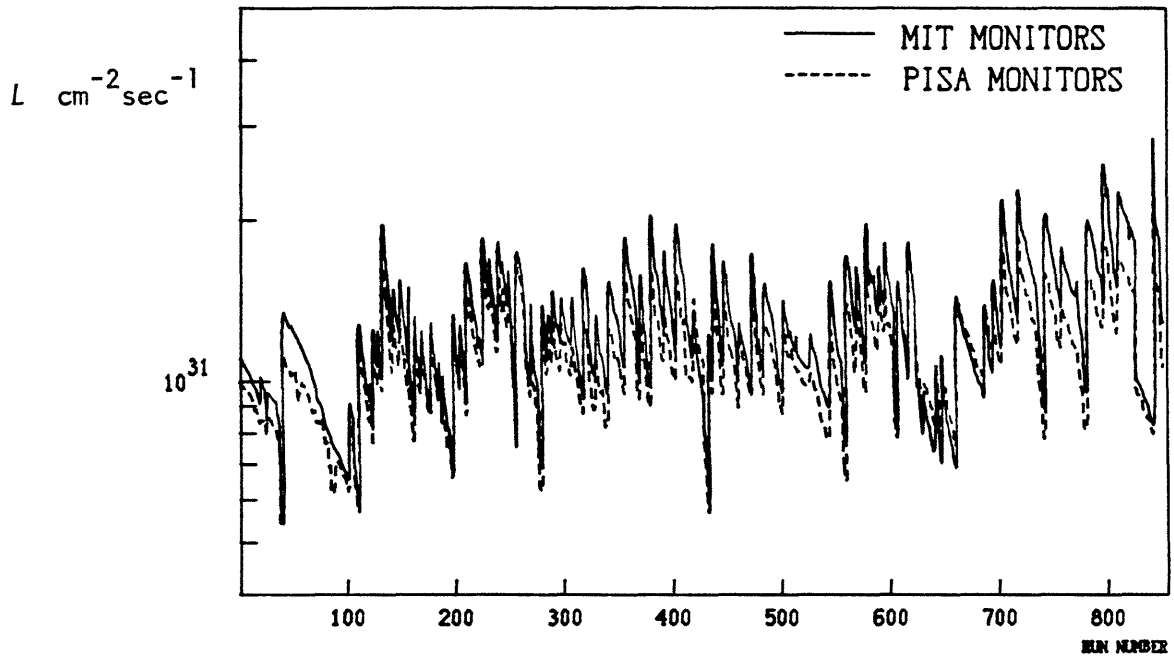
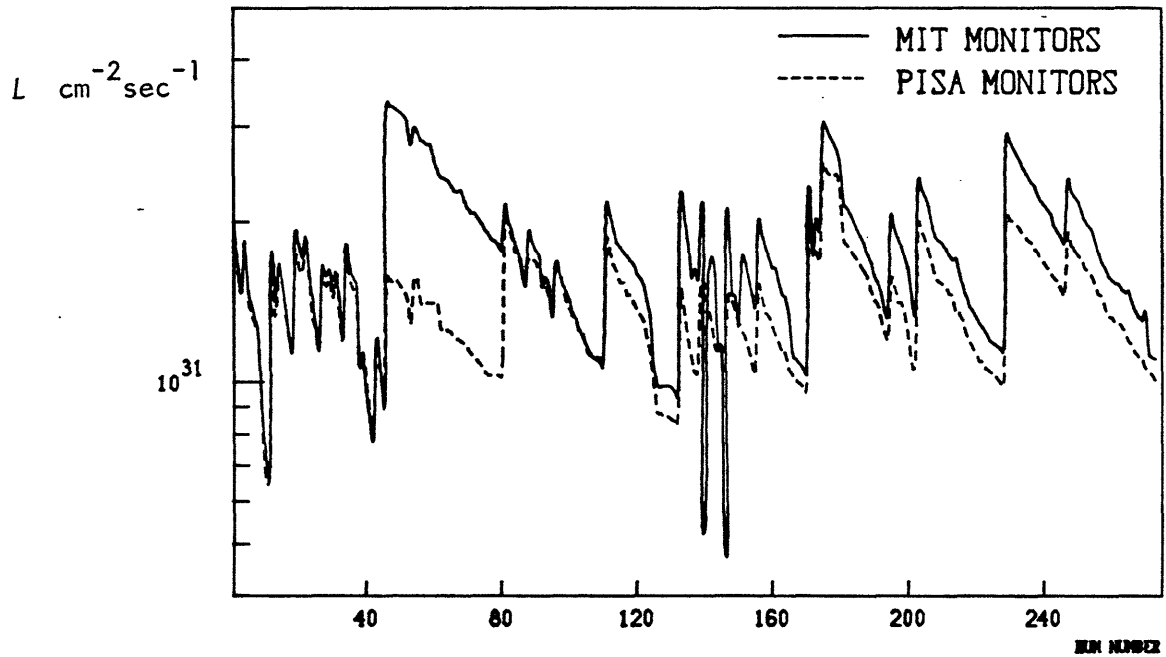


FIGURE II-14 DIFFERENTIAL LUMINOSITY



a) LUMINOSITY 62 GEV RUNS



b) LUMINOSITY 44 GEV RUNS

SECTION III DATA ANALYSIS

III-1) Overview

The experiment has accumulated 2900 hours worth of data at beam energy of 31-on-31 GeV ($\sqrt{s} = 62$ GeV) and 805 hours at $\sqrt{s} = 44$ GeV, yielding over 10^7 events on 1500 data tapes. Two separate analysis packages, which employ totally different approaches to event selection and track fitting, reduce and process the data in several stages (termed "Passes"). A comparison of results assists in estimating systematic errors.

The first two stages perform common functions in both analyses; Pass 1 filters accidental events out of the data stream, while Pass 2 performs the detailed track fitting. All subsequent stages apply fiducial cuts on the data, calculate and compensate for background, construct acceptance, produce cross-sections, and perform fits to the data. In the following text, one analysis chain* is explained in detail, and events are traced through from the raw data tapes to the final cross-sections output from Pass 6. Results from both programs are compared in Sec. III-8.

All event statistics mentioned at the end of each sub-section include data collected at both beam energies. Table III-1 illustrates the net event flow through the IBM analysis.

III-2) Pass 1, Tape Reduction

Due to the large amount of computer time required to fit tracks precisely through our geometry, it is desirable to pre-filter the data tapes and remove most accidental triggers before detailed reconstruction is attempted. Pass 1 checks the integrity of each event via the process summarized below:

- 1) Each muon track is defined as the coincidence of an inner hodoscope element with corresponding elements in an outer hodoscope. These tracks are located in the data buffer, and the time-of-flight between the inner and outer counter on each track is required to be consistent within

*) The two analysis chains are named in honor of their host computers; the program described here is the "IBM" analysis, and the "CDC" analysis is traced in Appendix III.

resolution with the distance between the counters, insuring that both hodoscopes were traversed by the same particle.

- 2) The drift chamber data is scanned, and spacepoints are constructed using the drift-time information and TDC calibrations. All chamber wires with drift times beyond fiducial limits are discarded. Each event is required to have spacepoints in at least six chamber modules.
- 3) At least 3 spacepoints are required to lie along each hodoscope track in the non-bending (ϕ) plane, and at least one of these 3 points must be located in a chamber interspersed within the magnet.
- 4) As a first approximation to 3-dimensional track reconstruction, a circle is fit to the spacepoints consistent with each hodoscope track. At least three of these spacepoints must be within 15 cm. of each circle.
- 5) If the D hodoscope was traversed by a track, the intercept along the incident counter is estimated from the difference in timing between the ends of the counter. This position is compared with a value calculated by an extrapolation of the circle fit, and they are required to agree within the fit accuracy and counter resolution (25cm).
- 6) The ϕ -match condition described in Sec. II-2 is enforced in a looser fashion; all hodoscope tracks are required to be back-to-back within ± 6 sectors.

If at least two tracks are approved via the above prescription, the event is considered potentially reconstructable and is written onto tape for later processing in Pass 2. A total of 1.08×10^7 triggers were input to the Pass 1 analysis, and only 1.03×10^5 events (1%) were accepted.

III-3) Pass 2, Momentum Reconstruction

Initially, hodoscope tracks are located and spacepoints are constructed as in Pass 1; however precise geometrical information is now input from the detector survey. Spacepoints are once again selected via a circle fit, and the angle of track incidence is employed in their calculation to enable a more precise determination. As a check of spacepoint integrity, the sum of the drift-times recorded at both parallel planes in each chamber module is required to approximate the 5 cm.

inter-wire spacing.

Next, a vertex search is initiated. Spacepoints are constructed in the chambers of the inner detector, and since there is no magnetic field, straight-line tracks are fit to all possible combinations of three such points. For each line acceptably fit, additional points are investigated and included in the track, provided they lie along the line. After all existing tracks are determined, a common vertex is established by calculating their closest distance of approach. If this calculation is acceptable, the tracks are re-fit as rays emanating from the vertex. The program then searches for additional tracks having at least two spacepoints collinear with the vertex.

Upon the completion of the vertex search, the muon track reconstruction begins. An analytical spline-fitting procedure is employed¹⁾ which numerically* calculates an optimum fit (as a function of track momentum). The track propagation accounts for the geometrical details of the detector, energy loss of the muons in iron,²⁾ and the magnetic field structure. Errors are assigned to spacepoints in accordance with multiple scattering; ie. points closer to the interaction have higher accuracy, hence greater weight over the fit, since the muons have penetrated less iron there than at the points in the chambers further removed. If a vertex was located in the inner detector, it is included in the fit and weighted according to its precision.

The detailed fit uses the coarse circle calculated earlier as an initial approximation, after which the spacepoints are re-evaluated using the angle-of-incidence derived from the more precise newly-fit track. The fitting procedure is invoked again, now using the previous fit as the initial approximation. The tracks are re-fit three times in this fashion before they are accepted, and the final momenta determined.

The Pass 2 program rejects events on the basis of poor fit quality. A total of 3.71×10^4 events (36%) were accepted and fitted. The muon-fit information, vertex/hadron-track data, chamber/spacepoint data, and hodoscope TOF's are all written onto a summary tape for continued processing via Pass 3.

*) The spline procedure fits mathematically via constructing and solving differential equations, as opposed to the iterative χ^2 minimization procedure applied in the CDC analysis (See Appendix III).

III-4) Pass 3, Data and Background Processing

The Pass 3 phase of analysis prepares the data output from Pass 2 for physical investigation and cross-section formulation. Remaining accidentals are rejected, like-sign muon events are separated from unlike-sign events, physical quantities are calculated from the muon momenta, and the kinematic distributions of background events are estimated.

Events are first subjected to the following scrutiny:

- 1) The difference in averaged timing between the D-counters intercepted by each track is evaluated for events where both muons traverse the D-hodoscope, and is required to be under 11 nsec.* This condition eliminates cosmic rays escaping the analogous trigger condition described in Sec. II-2, where multiple hits in the D-hodoscope can inhibit the effectivity of the brief on-line investigation.
- 2) The magnet polarity during each run is obtained by using the run/event index as a key into a tabulated summary file. Runs taken with the magnet off or with undefined polarity are eliminated. Test runs taken under altered triggering constraints and abnormal conditions are also removed.
- 3) All events without vertices established in the inner detector are eliminated. Most accidentals not arising from beam-beam interactions have no activity in the interaction region, hence lack a vertex and are eliminated by this cut. An example of such an accidental is portrayed in Figure III-1, which shows the computer reconstruction of a cosmic ray escaping all D-counter timing requirements due to "jitter" in the phototube pulses which reduced the difference in delay across the D-hodoscope to 7.1 nsec.; a value below restricted limits. There is no vertex (although linked tracks are well-defined along the muon trajectory in the inner detector).
- 4) The ϕ -matching condition discussed in the previous sections is once again applied; all hodoscope tracks are now required to be

*) The 11 nsec. cutoff was determined via observation of the distribution in D-counter TOF difference. Normal events peak at 0, and are contained within 11 nsec., while cosmic rays were seen to peak at 15 nsec.

back-to-back within ± 3 sectors (the original value enforced in the trigger constraints).

Another variety of accidental found in the fitted Pass 2 data is shown in Figure III-2. Here we see a pair of muons penetrating the magnet at a radius of about $1\frac{1}{2}$ meters and travelling almost exactly in the beam direction. By considering only chambers in the forward yokes, the Pass 2 reconstruction has produced a good fit to the event with reasonable kinematic parameters. Observing the picture, it is evident that the muons traced through the outer detector do not originate in a beam-beam interaction, even though a vertex is present.

These muons actually arise from collisions of beam protons with the collimator system upstream near intersection 3 (hence are termed "I3 muons"). They are generally of high momentum and are usually produced under bad beam conditions. I3 muons can penetrate the detector sufficiently often to be accidentally coincident with beam-beam interactions (as seen in Fig. III-2), thus defeating the vertex cut and contaminating the data.

A pattern-recognition scheme to eliminate these accidentals is initiated in Pass 3. In order to be considered for scrutiny, a track must have at least three associated spacepoints in the forward quarter of the detector. A linear least-squares fit is then attempted to all spacepoints within 45° of candidate tracks. The deviations of the fitted points are examined, and the line is re-fit after elimination of overlapping points with high residuals, due to multiple hits and noise in the chambers. The χ^2 of this fit, the $z=0$ intercept (distance from the intersection), the slopes (dy/dz and dx/dz), and the number of points actually used in the fit are all packed into one decimally coded word for further processing in Pass 5. The usage of these parameters is discussed in Section III-6.

The mass, P_t , X_F , $\cos \theta_{cs}$, and other relevant kinematic variables are calculated for each event using the fitted muon momenta. These quantities, along with various track quality parameters, are written onto mass-storage files for future analysis.

Three types of events are seen in the detector; events with muon tracks of opposite sign, events where both muon tracks are focused, and

events where both muon tracks are de-focused*. These event types are separated into three independent files.

Figure III-3 illustrates the appearance of like-sign events in the detector. All such events come from background processes such as hadron decay and punch-through, or accidentals as were described above, thus both tracks in a like-sign event arise independently of each other[†]. This is also extended to background events of unlike-sign, where we assume the focused and de-focused tracks to have no correlation. In order to estimate the behavior of the background in the unlike-sign data, simulated "background" events are fabricated by pairing all non-redundant combinations of focused tracks from focused/focused events with de-focused tracks from de-focused/de-focused events. This approximates the unlike-sign background, provided that the non-correlation assumption is correct. Pairing is done separately for each magnet polarity in order to avoid mixing tracks of different charge.[‡]

Kinematic variables are calculated for these simulated background events and are written onto a fourth mass-storage file along with quality parameters for the component tracks, in similar fashion to the actual data.

Figure III-4 presents a check on the accuracy of the background distributions calculated for both beam energies. Here we have randomly paired tracks of similar sign together from different like-sign events (focused tracks from one focused/focused event with focused tracks from another focused/focused event, and ditto for de-focused/de-focused events). Provided that our assumptions are correct, these simulated like-sign

-
- *) To avoid charge-dependent acceptance, half of the data is taken with reversed magnet polarity, which inverts the mapping of charge onto bending direction. Because they generally penetrate less iron, the acceptance for de-focused tracks is much greater than the acceptance for focused tracks.
 - †) Since both primaries decay independently after production, tracks due to hadron decay are not correlated. Most accidental and punch-through tracks are also unrelated; however not the I3 muons, which tend to be produced in pairs, as seen in Fig. III-2. These are removed via cuts described in Section III-6.
 - ‡) Since two protons collide in the initial state, there must be a net charge of +2 in the final state, which will yield a surplus of positively charged particles. Separating the data for opposite magnet polarities accounts for this asymmetry in the background.

distributions should match their analogous distributions in the actual data within statistical accuracy. Separate columns are given for focused/focused and de-focused/de-focused events; solid lines denote actual data, while dashed lines represent the randomly paired tracks (the randomized distributions are normalized to the data). We see quite reasonable agreement in most cases. A small shift may be present in the focused/focused mass and P_t distributions, however low statistics prevent a precise comparison. Effects due to background uncertainty are discussed in Appendix II.

The four summary files created in Pass 3 (one for unlike-sign events, focused/focused events, de-focused/de-focused events, and paired background events) are read by subsequent analysis stages. 28747 events (77.5%) were approved and written to mass-storage (not including paired background events).

III-5) Pass 4, Redundancy Check

Occasionally while processing unlabeled raw data tapes, operators will mount an identical volume twice in succession, creating a duplicate set of data on the output files. Pass 4 searches for and eliminates these redundancies in the data. 28747 events were on files before Pass 4, afterwards 28685 events (99.8%) remained.

III-6) Pass 5, Cross-Section Formulation

a) Monte-Carlo Re-weighting

The Monte-Carlo simulation program was introduced in Sec. II-3. The production mechanism models the behavior of the continuum seen in dimuon spectra for masses beyond 3 GeV, discounting the J, T, and associated resonances. Events are generated according to the ansatz:^{*}

*) These distributions are based on the data of Ref. 3.

$$\frac{d^4N}{dm dP_t^2 dX_F d\cos\theta_{cs}} \propto G(m) \cdot F(\alpha_0, \beta_0, \eta_0) \quad \begin{array}{l} \alpha_0 \equiv 1.1 \\ \beta_0 \equiv 2.8 \\ \eta_0 \equiv 0.0 \end{array}$$

where:

$$\text{Eq. III-1)} \quad G(m) \equiv \frac{e^{-0.299 m}}{m^3}$$

$$F(\alpha, \beta, \eta) \equiv e^{-\alpha P_t} (1 - |X_F|)^\beta (1 + \eta \cos^2 \theta_{cs})$$

The Pass 5 program reads summary files containing the kinematic properties of fitted Monte-Carlo events. In order to "fine-tune" the generated event distributions to those actually observed in the data, events are "re-weighted" to yield new parameters $\alpha_1, \beta_1, \eta_1$, and insert a more accurate mass dependence⁴⁾:

$$\text{Eq. III-2)} \quad G'(m) \equiv \frac{(1 - m/\sqrt{s})^{10}}{m^4/\sqrt{s}}$$

The reweighting method assigns a "weight" to each Monte-Carlo event of:

$$\text{Eq. III-3)} \quad W_i = \frac{G'(m) \cdot F(\alpha_1, \beta_1, \eta_1)}{G(m) \cdot F(\alpha_0, \beta_0, \eta_0)} \quad \begin{array}{l} \text{calculated at the generated} \\ P_{t_i}, m_i, X_{F_i}, \cos\theta_{cs_i} \text{ of the event} \end{array}$$

Instead of counting all events in a histogram with unity weight, each event will count as W_i events, hence the original dependence is effectively divided out, and the new relation is factored in. All re-weighted distributions are scaled such that they integrate to the same values as the original distributions.

The Monte-Carlo generates events at $\sqrt{s} = 62$ GeV. The distribution $F(\alpha, \beta, \eta)$ describes the data at both 62 and 44 GeV, and since scaling violations are expected to be small,⁵⁾ relation III-2 is also assumed valid for the 44 GeV data. These properties enable us to use the same Monte-Carlo data set for both 62 and 44 GeV; however the kinematic definition of X_F involves \sqrt{s} , and we

must re-define:

$$\text{Eq. III-4)} \quad X_{F(44 \text{ GeV})} = X_{F(62 \text{ GeV})} \cdot (62/44) = X_{F(62 \text{ GeV})} \cdot (1.408)$$

b) Fiducial Cuts

Four fiducial cuts are applied to the data in Pass 5 which remove remaining accidentals, eliminate badly fitted events, and increase the data/background ratio from 50 % to 80%. For consistency in acceptance calculation, the Monte-Carlo events are also processed through the same cuts. Event flow in Pass 5 is summarized in Table III-2, and the details of each cut are listed in the following discussion:

i) Bdl* Minimum

Both muons per event are required to penetrate at least 22 KG-meters[†] of magnetized iron. This insures that the tracks have traversed sufficient bending-path for reliable momentum fitting. Figure III-5 illustrates two common types of events plaguing the background which are eliminated by this cut. Part a) shows a "chimney" event, in which track 1 escapes the detector through the gap between yokes 1 and 2 (just forward of the intersection), thus bypassing much absorber. Part b) is a "seagull" event, where track 1 is bent around the rear of the magnet by the residual field there, and traverses very little iron. The Bdl's for the bad tracks in both of these events, as read from the figure, are well under 22 KG-m; hence they are rejected. The Bdl cut is instrumental in covering these "thin" spots in the detector which can fall prey to hadron punch-through.

Figure III-6 displays the distributions of minimum Bdl[†] for events at both beam energies. The data (unlike sign), background (like-sign), and

-
- *) The amount of magnetized iron (in KGauss-meters) traversed by a track is abbreviated "Bdl".
 - †) In deriving $d\sigma/dm$, a 22.5 KG-m cutoff is used; this value is marginally loosened to 22.0 KG-m for the other kinematic cross-sections because of the tighter χ^2 cut applied.
 - +) If one track in an event has a Bdl under the cutoff, the event is rejected; hence the parameter on which we cut is the "minimum" Bdl of the event, ie. the Bdl of the track penetrating least iron.

Monte-Carlo have all been normalized to the same peak value, thus are not plotted to the same scale. It is evident that the background generally tends toward lower Bdl than the data, supporting the existence of hadrons punching through "weak" areas in the detector. The Bdl distribution of the Monte-Carlo agrees with that of the data, and both exhibit the strong peak at Bdl \approx 26 KG-m due to the detector geometry.

The net normalization of data-background over acceptance was found to be constant for cuts up to Bdl > 27 KG-m, at which point a lack of statistics begins to affect background and acceptance calculations.

The imposed Bdl minimum of 22 \rightarrow 23 KG-m can be seen to cut a considerably higher percentage of background than data without significantly depriving statistics and affecting overall normalization, thus is one of the prime conditions imposed in the Pass 5 analysis. Numerical results are presented in Table III-2, where one can see drastic improvement in the background normalization after chimney events (such as shown in Fig. III-5 (a)) are eliminated from the de-focused/de-focused data.

ii) χ^2 Maximum

One of the track quality parameters generated by Pass 2 and stored on the Pass 3 summary files is the χ^2 of the momentum fit. Quantatively:

$$\text{Eq. III-5) } \chi^2 \equiv \sum_i (\Delta_i / \sigma_i)^2 \quad \text{where:}$$

Δ_i = Distance between spacepoint_(i) and fitted track

σ_i = Error allotted spacepoint_(i) from multiple scattering

The sum is taken over all spacepoints per track.

The χ^2 of a track is a measure of the "goodness" of its fit. Event pictures were scanned to ensure event selection as a function of a χ^2 -maximum* cut.

*) In the remainder of the text and figures, " χ^2 " denotes the sum of the χ^2 of both fitted tracks. In the event pictures, the χ^2 for each track are listed separately as "X1" and "X2".

The following resulted:

- $\chi^2 < 10$: All excellent fits, very little (<3%) accidentals
- $\chi^2 < 20$: Mainly good fits, few ($\approx 3\%$) accidentals.
- $\chi^2 < 50$: Most events are fitted reasonably. Accidentals pollute 5→10% of the data.
- $\chi^2 > 50$: Mostly misfitted events and accidentals.

The χ^2 distributions of data, background and Monte-Carlo events are shown in Fig. III-7. We can immediately see that the background has a higher average χ^2 than data, due to accidental processes and misfitting in many like-sign events.

The data has more events at high χ^2 than the Monte-Carlo. Much of this effect is due to background contaminating the data which has not yet been subtracted in the figure. In our complicated geometry, it is impossible to precisely imitate all processes influencing the data; this modeling inefficiency also contributes somewhat to the lower χ^2 tail of the Monte-Carlo.

The net normalization of data-background over acceptance is independent of the χ^2 cut applied down to $\chi^2 < 10$, before falling statistics appreciably affect results.

iii) P_t maximum

Accidentals such as cosmic rays often are fit with unphysical values of kinematic parameters. A P_t maximum of 12.5 GeV has been imposed on the data to intercept remaining events of this type, and the results are summarized in Table III-2. A detailed scan of event pictures has yielded no bona-fide, well-fitted events with $P_t > 12.5$ GeV.

iv) I3 Cut

The Pass 5 program employs the linear fit information output from Pass 3 to recognize and reject the I3 muons described in Section III-4. Figure III-2 shows a typical example, and the basic signatures of this type of accidental are readily obvious:

- 1) The I3 muons tend to travel in the beam direction, thus dx/dz and dy/dz of the fitted line are under 0.2.

- 2) The I3 muons are usually displaced from the intersection region at $z=0$,^{*} thus using the fit, we can expect $r_0 \equiv \sqrt{x^2+y^2} \Big|_{z=0}$ to be over $1\frac{1}{4}$ meters. Normal muons yield much smaller values of r_0 because they always originate in the intersection region.
- 3) The I3 muons are usually of high momenta (>6 GeV), thus bend very little and result in excellent straight-line fits with low residuals (under 5cm/point).
- 4) Any line fit to the spacepoints associated with a good track will always point toward the intersection as $z \rightarrow 0$. If the line leads away from the intersection, it generally belongs to an I3 muon bending outward.[†]

Conditions are applied to the linear fit parameters in order to identify and remove prospective I3 muons which fulfill the above prescriptions. 100 raw events not passing this cut were manually scanned to test its validity; over 95% were indeed due to I3 muons, and the remainder arose from other accidentals. The selection efficiency was also examined by isolating a sample of 25 I3 muons through handscan and applying the cut; all 25 events were flagged and rejected.

Since I3 muons plague focused/focused events, this cut aids in reducing background normalization. Results are summarized in Table III-2.

c) Event Scan

Pictures were made of all events output from Pass II having $m > 8$ GeV, and three physicists patiently scanned and commented on each one. A total of 2300 events were examined. The functions and results of the scan are discussed below:

i) Tracing of "BAD" events

A "BAD" event arises from an accidental process. Events voted "BAD" by the scanners were flagged and traced through the Pass 3 and Pass 5 analyses.

-
- *) The origin ($x=y=z=0$) is defined at the center of the intersection. The beam axis points in the z direction, and the x -axis points radially out of the ISR.
 - †) Most I3 muons exhibit little or no bending. Any I3 muons bent outward are recognized by condition (4), while those bent far inward cannot be discerned from normal tracks, however they will give worse momentum fits due to track propagation in the wrong direction.

As summarized in Table III-3, we originally saw BAD/total ratios of 30% (62 GeV) and 56% (44 GeV) in the data output from Pass 2. After Pass 5, these ratios drop to 4.2% (62 GeV) and 4.5% (44 GeV), and attest to the effectivity of the fiducial cuts. BAD events are eliminated for $m > 8$ GeV, and the lower mass data is normalized down by the final ratios.

ii) Correction for Vertex-finding Efficiency

All events lacking a vertex were eliminated in Pass 3. Events approved by the scanners, yet missing a vertex in the inner detector, were added back into the Pass 5 analysis, resulting in a 9% \rightarrow 14% correction for $m < 8$ GeV, as described in Table III-3.

iii) Investigation of "Misfit" Events

The scanners also noted the fit quality. In a small sample of good events (7% of the raw data), the fit was found to be perturbed considerably by various secondary processes (random hits in chambers, etc.). The IBM Pass 2 program allots three trials for a successful fit convergence; in many of these cases the final fit still was not completely optimized. The CDC analysis (described in Appendix III) employs totally different methods of momentum fitting, spacepoint weighting and energy-loss calculation. Many of the misfit events were fitted successfully by this package, and in these cases the results of the other analysis were substituted. If the event was not found in the alternative analyses, it was declared "ambiguous" and deleted from the actual data sample, although retained in its normalization.

iv) Correction for Event-finding Efficiency

A comparison of Pass 2 results from the two major analysis chains yielded a small sample of good-quality events which were accepted by the CDC analysis, but missed by the program discussed here. An investigation indicated that much of the discrepancy was due to differences in basic fitting methods, as discussed above.

A version of the IBM Pass 2 was created which loosened the weight on the inner chambers. Most of these "missing" events were now fitted by the new program. Little change was seen in the amount of accepted Monte-Carlo events; acceptances of both programs were compatible. The other analyses employed additional information from the Naples Telescopes (see Sec. II-1) in vertex determination; this also resulted in acceptable fits of previously "missing" events.

All events with $m > 8$ GeV which were found in other analyses, but missed in the original IBM Pass 2 output were subjected to the inquiry of the scanning physicists. Approved events were added into the Pass 5 data flow and yielded corrections of $10 \rightarrow 13\%$ for the unscanned data.

After all events tagged via the scan are traced through the analysis, we receive a net normalization of $1.18 \rightarrow 1.20$ (depending on the beam energy and the cuts applied) relative to the original "unscanned" sample, as summarized in Table III-3. All data and background distributions are scaled by this factor* for $m < 8$ GeV. Events eliminated by "BAD" determination or re-fitting are accounted for in Table III-2.

d) Background Subtraction

Assuming both tracks of like-sign events to be uncorrelated, an elementary statistical pairing relation may be invoked to estimate the quantity of unlike-sign background:

$$\text{Eq. III-6)} \quad N_{\text{BKG}} = 2\sqrt{N_{\text{FF}} \cdot N_{\text{UU}}} \quad \text{where:}$$

N_{BKG} = Estimated number of unlike-sign background events.
 N_{FF} = Number of focused/focused events.
 N_{UU} = Number of de-focused/de-focused events.

The randomly-paired background data is normalized to integrate to N_{BKG} . This is done separately for each magnet polarity, and re-scaled data from both polarities are summed to form the final background distributions which

*) We assign a systematic error of $\pm 5\%$ to this factor due to scan uncertainties.

are subtracted bin-by-bin from the corresponding histograms filled with unlike-sign data.

e) Acceptance and Cross-section Calculation

Histograms are filled with the kinematic parameters of accepted Monte-Carlo events, weighting each by W_1 as introduced in Eq. III-3. Figures III-8 through III-11 show the actual data-background distributions for mass, P_t , X_F , and $\cos\theta_{cs}$ (the latter three are presented in selected mass bins), compared with the distributions filled with Monte-Carlo events.* We see a very good agreement within statistical determination, which attests to accurate modeling in the Monte Carlo.

Histograms are also filled with the kinematic spectra of generated events, as described by:

$$\text{Eq. III-7} \quad \frac{d^4N}{dm dP_t^2 dX_F d\cos\theta_{cs}} \propto G'(m) \cdot F(\alpha_1, \beta_1, \eta_1)$$

(referencing Eq. III-1 thru III-3 and associated discussion)

Each histogram is normalized such that the above relation integrates to the total number of actual Monte-Carlo events generated (1.5 million). The acceptance is defined as the bin-by-bin ratio of histograms filled with accepted and fitted Monte-Carlo events over corresponding histograms filled with the generated spectra.

The data-background distributions are divided bin-by-bin by this acceptance, thus producing the cross-section. Statistical errors are propagated through each stage of the process, and appear with the final histograms.

*) The Monte-Carlo distributions shown in the figure are normalized to the data-background distributions. The values of $\alpha_1, \beta_1, \eta_1$ (see Eq. III-1) used in each plot are presented in Appendix II. In general, they are manually adjusted to be within one σ of the corresponding fits to the data. Sensitivity to the assumed production parameters is also discussed in Appendix II.

In summary, the cross-sections are calculated (bin-by-bin) as:

$$\text{Eq. III-8)} \quad \left. \frac{d\sigma}{d\lambda} \right|_i \propto \frac{N_{\text{data}} - N_{\text{bkg}}}{\text{ACC}} \Big|_i \quad \lambda = \text{Arbitrary parameter}$$

$$\text{ACC}_i \equiv \frac{N(\text{fitted MC})}{N(\text{gen. MC})} \Big|_i$$

(Calculated at bin # i of histogram)

Figures III-12 through III-19 present the step-by-step procedure sketched above for cross-section formulation. Three types of plots are presented; one showing data and background distributions,* another showing acceptance (the smoothed lines are only to guide the eye; the data points are actually used in the calculation), and the third presenting the actual cross-section (the curves are fits to the data, all listed in Appendix II). Such plots are presented for mass, P_t , X_F , and $\cos\theta_{cs}$ (the last 3 in appropriate mass bins[†]), at both beam energies. The amounts of data and background in each mass range are listed in Table III-4.

Because of the fall in acceptance with increasing $|\cos\theta_{cs}|$, there are generally few events in the tail of the $\cos\theta_{cs}$ distributions (see Figs. III-18 and III-19). These events bear considerable weight on fits to the form $(1 + \eta \cos^2\theta_{cs})$, since η is most clearly defined at high $\cos\theta_{cs}$. With the statistics so limited, the tail events are very sensitive to acceptance and background corrections. In order to reduce all possible

*)These plots are presented in absolute units, hence the y-axes represent the # of events per bin. All events plotted vs. P_t are weighted by $1/P_t$, thus the y-axes in these plots are in # events/GeV.

†)Due to the acceptance cutoff at low mass, sufficient statistics are not available in the Monte-Carlo for an exact acceptance calculation at 3.1 GeV. In the J region (2 → 4 GeV), the P_t acceptance is approximated by weighting all Monte-Carlo events which are both fitted and generated between $2 < m < 4$ GeV to a flat spectrum; this contributes to the large systematic error assigned to these fits. Cross-sections for X_F and $\cos\theta_{cs}$ cannot be produced in the J region due to the extremely limited span^{cs} of acceptance (see Fig. II-8). The range $4 < m < 5$ GeV was omitted from our mass slices due to the large background subtraction there.

systematic uncertainty in $\cos\theta_{cs}$, the following additional precautions were taken:

- 1) As seen in Figs. III-18 and III-19, the background is flat out to $|\cos\theta_{cs}| < 0.8$ and has a small peak at $|\cos\theta_{cs}| \approx 0.5$, while the data consistently drops for $|\cos\theta_{cs}| > 0.4$. This results in a low data/background ratio in the tail of the distribution, which has a large effect on the fit. In order to minimize uncertainty from the background, we have taken the low-mass "slice" of data from $6 \rightarrow 8$ GeV and omitted the $5 \rightarrow 6$ GeV region, which has considerable background contamination.
- 2) In order to minimize any possible discrepancy in acceptance, no events were added as misfit, vertex, or event-finding efficiency corrections for $m > 8$ GeV. The data was scaled by the factors described in part (c) of this section. All events flagged BAD were still eliminated.
- 3) One of the drift chambers between magnet yokes 1a and 1b (see Fig. II-3) had developed a small leak during the last 15% of data taken at 62 GeV, which had slightly lowered its efficiency. This 15% fraction had no significant effect on the other quantities presented, however a small shift in the tail of the $\cos\theta_{cs}$ distributions was noticed, so this portion was eliminated from the $\cos\theta_{cs}$ data sample to insure its integrity.

The above conditions yielded no significant changes in the shapes of other distributions, hence all data was retained in their derivation in order to maximize the statistics.

III -7) Pass 6, Normalization and Data Fitting

The Pass 6 program reads the stored Pass 5 histograms from disk, and first calculates scale factors for the cross-sections as summarized below:

$$\text{Eq. III-9) } \left(\frac{d\sigma}{d\lambda} \right)_{\text{absolute differential cross-section in cm}^2/\lambda\text{-units}} = \left(\frac{d\sigma}{d\lambda} \right)_{\text{Pass 5}} \cdot \left[\frac{R}{w \cdot L} \right]$$

where:

R = Scale factor from scan
1.00 (m > 8 GeV)
≈1.19 (m < 8 GeV)

w = Bin-width of histogram

L = Integrated Luminosity
1.12 · 10 ³⁸ cm ⁻² (62 GeV)
0.45 · 10 ³⁸ cm ⁻² (44 GeV)

Detailed fits are made to the cross-sections, plots are constructed, and the underlying physics is investigated. More specific details of pass 6 programs are discussed in Section IV.

III-8) Analysis Comparison

Figure III-20 presents a direct comparison of results between the two analysis procedures. We plot the ratio:

$$\text{Eq. III-10) } \delta_m = \frac{2(m_{\text{IBM}} - m_{\text{CDC}})}{m_{\text{IBM}} + m_{\text{CDC}}}$$

for the mass values, and a similar δ_{p_t} , δ_{x_F} , $\delta_{\cos\theta_{cs}}$ for the other quantities. δ is equal to the percentage difference between the analysis results. The histograms in Fig. III-20 are filled with the values of δ for all of the events common to both analyses.* The overlaid gaussians are fits to these distributions, and we notice that the σ 's for all quantities at both beam energies agree excellently with the averaged resolutions quoted in Sec. II-3 and Figs. II-10 thru II-13. The $\cos\theta_{cs}$ distributions seem to have finite

*) To insure the integrity and quality of the fit, these events are strained through $\chi^2 < 50$ and Bdl > 22.5 KG-m cuts in both analyses before being plotted. The events are required to be fitted as unlike-sign in both analyses.

tails; these are due to the decline in resolution in $\cos\theta_{cs}$ at low mass (and are mainly from J's at 3.1 GeV). Events not in common between the analyses were checked for fitting biases, but their distributions were also seen to agree within resolution.

The above discussion indicates a satisfactory agreement on the event level, and a comparison of cross-sections was next attempted to determine systematic error in final results. The cross-sections $d\sigma/dm$ were in complete agreement. We also found good agreement in the X_F , P_t , and $\cos\theta_{cs}$ cross-sections in a bin-by-bin comparison, however these fits were more sensitive to systematics, fitting biases, and statistics over the selected mass ranges. The cross-sections for these quantities resulting from the two analyses were averaged together bin-by-bin to account for any systematic differences. The averaging procedure is described in Appendix III. Due to the good agreement between the different analyses, the unaltered $d\sigma/dm$ values from one procedure are quoted (the IBM values are used due to the higher statistics).

SECTION III - REFERENCES

- 1) H. Wind, Nuc. Inst. and Methods, 115, 431 (1974).
- 2) P.M. Joseph, Nuc. Inst. and Methods, 75, 13 (1969).
- 3) K.J. Anderson et. al., Phys. Rev. Lett. 42, 944 (1979).
G. E. Hogan et. al., Phys. Rev. Lett. 42, 948 (1979)
J. K. Yoh et. al., Phys. Rev. Lett. 41, 684 (1978).
- 4) K. Kinoshita et. al., Phys. Rev. D, 17, 1834 (1977).
- 5) D. Antreasyan et. al, Phys. Rev. Lett., 45, 863 (1980).

In the above publication, the scaling prediction in ref. 4 was shown to describe both our data at 62 GeV and data from:

D. M. Kaplan et. al., Phys. Rev. Lett. 40, 435 (1978).
which was taken at $\sqrt{s} = 27.4$ GeV. (See also Sec. IV of this thesis).

We also thank R. Horgan from the CERN theory division for discussions concerning this topic.

TABLE III-1

EVENT FLOW THROUGH THE IBM ANALYSIS CHAIN

Analysis Stage	$\sqrt{s} = 62 \text{ GeV}$			$\sqrt{s} = 44 \text{ GeV}$		
	# Events					
Raw events on data tapes	7.7×10^6			3.1×10^6		
Pass 1	80,104			22,812		
Pass 2	28,371			8,700		
Pass 3	23,558			5,189		
	FF	FU	UU	FF	FU	UU
	1,046	13,799	8,713	453	3,184	1,552
Pass 4	1,045	13,766	8,685	453	3,184	1,552
Hand Scan added evts.	1,045	14,070	8,685	453	3,208	1,552
Pass 5 (see Table III-2)	239	7,827	2,389	62	1,509	341
	6,330			1,225		
	Data-Background					

FF: Focused/Focused events
 UU: De-focused/De-focused events
 FU: Unlike-sign events

TABLE III-2

EVENT FLOW IN THE IBM PASS 5

Definitions:

FU: Unlike-sign events

FF: Focused/Focused events

UU: De-focused/De-focused events

BK: Paired background events created in Pass 3

MC: Monte Carlo events

NRM: Normalized Background events (see Eq. III-6)

% NRM/FU: Background/Data ratio

The "cut#" refers to the number given to the particular cut in part (b) of Sec III-6.

Four tables are presented for the two cut-values imposed on data at both beam energies.

All cuts are listed in the order actually applied in the Pass 5 program.

The percentages given under the event values are relative to the number of events passed by the previous cut.

The percentages listed under "Total Events Passed" are the ratios of the number of events accepted after all cuts to the number of events originally input from Pass 4.

THE TABLES ARE PRESENTED ON THE FOLLOWING TWO PAGES

TABLE III-2 (Cont.)

1) Cuts used for $d\sigma/dm$

a) $\sqrt{s} = 62$ GeV

Cut #	Cut Desc.	# Events						
		FU	FF	UU	BK	MC	NRM	ZNRM/FU
-----	Input from Pass 4	13766	1045	8685	54475	31980	5997	43.6%
-----	Hand-scan additions (m > 8)	+304						
2	$\chi^2 < 50$	-1445 10.3%	-382 36.6%	-967 11.1%	-12698 23.3%	-464 1.5%	4505	35.7%
1	Bdl > 22.4 KGm	-4565 36.2%	-220 33.2%	-5300 68.7%	-23487 56.2%	-7734 24.5%	2058	25.5%
3	$P_t < 12.5$ GeV	-36 0.4%	-4 0.9%	-10 0.4%	-129 0.7%	-21 0.1%	2044	25.5%
4	I3 elimination	-150 1.9%	-200 45.6%	-19 0.8%	-5233 28.8%	0	1497	19.0%
-----	BAD event elimination (from scan)	-25						
-----	Misfit and ambiguous elimination (from scan)	-23						
-----	Total Events Passed	7827 56.9%	239 22.9%	2389 27.5%	12928 23.7%	23761 74.3%	1497 25.0%	19.1%

b) $\sqrt{s} = 44$ GeV

Cut #	Cut Desc.	# Events						
		FU	FF	UU	BK	MC	NRM	ZNRM/FU
-----	Input from Pass 4	3184	453	1552	55090	31964	1665	52.3%
-----	Hand-scan additions (m > 8)	+24						
2	$\chi^2 < 50$	-506 15.9%	-206 45.5%	-238 15.3%	-17100 31.0%	-464 1.5%	1128	41.7%
1	Bdl > 22.5 KGm	-1106 40.9%	-84 34.0%	-961 73.1%	-22866 60.2%	-7505 23.8%	471	29.5%
3	$P_t < 12.5$ GeV	-5 0.3%	-3 1.8%	0	-85 0.6%	-22 0.1%	466	29.3%
4	I3 elimination	-79 5.0%	-98 61.3%	-12 3.4%	-7743 51.5%	0	284	18.8%
-----	BAD event elimination (from scan)	-3						
-----	Misfit and ambiguous elimination (from scan)	0						
-----	Total Events Passed	1509 47.4%	62 13.7%	341 22.0%	7296 13.2%	23973 75.0%	284 17.1%	18.8%

TABLE III-2 (Cont.)

ii) Cuts used in other cross-sections

a) $\sqrt{s} = 62$ GeV

Cut #	Cut Desc.	# Events						ZNRM/FU
		FU	FF	UU	BK	MC	NRM	
-----	Input from Pass 4	13766	1045	8685	54475	31980	5997	43.6%
-----	Hand-scan additions	+304 (m > 8)						
2	$\chi^2 < 20$	-2881 20.9%	-629 60.2%	-2154 24.8%	-22154 42.2%	-1279 4.0%	3272	29.2%
1	Bdl > 22.0 KGm	-3445 30.8%	-127 30.5%	-4207 64.4%	-16554 52.6%	-6284 20.5%	1789	23.1%
3	$P_t < 12.5$ GeV	-21 0.3%	-1 0.3%	-2 0.1%	0	-20 0.1%	1785	23.3%
4	I3 elimination	-116 1.5%	-99 34.4%	-14 0.6%	-4052 27.1%	0	1302	17.1%
-----	BAD event elimination (from scan)	-16 (m > 8)						
-----	Misfit and ambiguous elimination (from scan)	-20 (m > 8)						
-----	Total Events Passed	7571 55.0%	189 18.1%	2308 26.6%	10888 20.0%	24397 76.3%	1302 21.7%	17.1%

b) $\sqrt{s} = 44$ GeV

Cut #	Cut Desc.	# Events						ZNRM/FU
		FU	FF	UU	BK	MC	NRM	
-----	Input from Pass 4	3184	453	1552	55090	31980	1665	52.3%
-----	Hand-scan additions	+24 (m > 8)						
2	$\chi^2 < 20$	-896 36.0%	-305 67.3%	-471 30.3%	-28305 51.4%	-1279 4.0%	791	34.2%
1	Bdl > 22.0 KGm	-832 36.0%	-46 31.1%	-758 70.1%	-15105 56.4%	-6284 20.5%	334	22.5%
3	$P_t < 12.5$ GeV	-3 0.2%	-2 2.0%	0	-61 0.5%	-20 0.1%	330	22.4%
4	I3 elimination	-53 3.6%	-60 60.0%	-10 3.1%	-6114 52.6%	0	212	14.9%
-----	BAD event elimination (from scan)	-2 (m > 8)						
-----	Misfit and ambiguous elimination (from scan)	0 (m > 8)						
-----	Total Events Passed	1422 44.7%	40 8.8%	313 20.2%	5505 10.0%	24397 76.3%	212 12.7%	14.9%

TABLE III-3

Breakdown of Scan Normalization Factors

a) $\sqrt{s} = 62 \text{ GeV}$

Operation	# Events approved by Pass 5	% Correction to Normalization	
Original Events at $m > 8 \text{ GeV}$	599	----	
BAD Event Deletion	-25	-4.2%	
Misfit Adjustment	+1	+0.2%	
Missing Vertex Corr.	+53	+8.8%	
Event-finding Eff.	+78	+13.0%	
Final Events at $m > 8 \text{ GeV}$	706	+17.9%	Scale factor for $m < 8 \text{ GeV}$

304 events were added to the Pass 5 input:

80 Re-fit events, 69 Missing-Vertex Events, and 155 Finding-eff. Events

$$\frac{\text{BAD Events } (m > 8)}{\text{total Events } (m > 8)} = \frac{334}{1150} = 30\% \text{ Before Pass 5 cuts}$$

$$" = \frac{25}{599} = 4.2\% \text{ After Pass 5 cuts}$$

$d\sigma/dm$ cuts are used here.

For cuts used in deriving the other cross-sections, the final scale factor for $m < 8 \text{ GeV}$ is, +19.9%

b) $\sqrt{s} = 44 \text{ GeV}$

Operation	# Events approved by Pass 5	% Correction to Normalization	
Original Events at $m > 8 \text{ GeV}$	67	----	
BAD Event Deletion	-3	-4.5%	
Misfit Adjustments	0	0	
Missing Vertex Corr.	+9	+13.4%	
Event-finding Eff.	+7	+10.4%	
Final Events at $m > 8 \text{ GeV}$	80	+19.4%	Scale factor for $m < 8 \text{ GeV}$

24 Events were added to the Pass 5 input:

4 Re-fit Events, 11 Missing-Vertex Events, and 9 Finding-eff. Events

$$\frac{\text{BAD Events } (m > 8)}{\text{tot Events } (m > 8)} = \frac{112}{200} = 56\% \text{ Before Pass 5 cuts}$$

$$" = \frac{3}{67} = 4.5\% \text{ After Pass 5 cuts}$$

$d\sigma/dm$ cuts are used here.

For cuts used in deriving the other cross-sections, the final scale factor for $m < 8 \text{ GeV}$ is, +18.5%

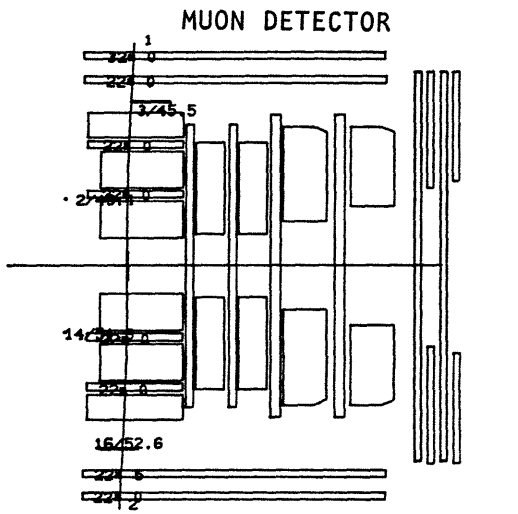
TABLE III-4

Total Events used in Cross-section Derivation

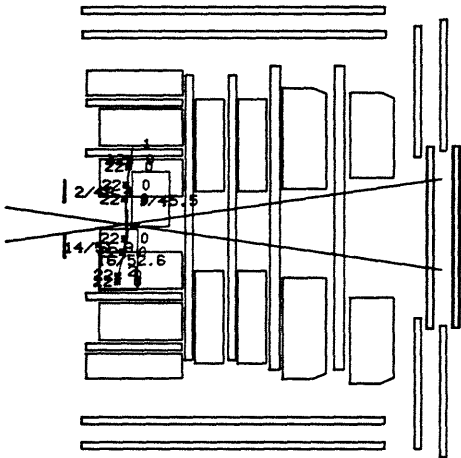
\sqrt{s}	Mass Range (GeV)	# Events			
		IBM data	IBM background	CDC data	CDC background
62 GeV	$d\sigma/dm$ (2 < m < 25 GeV)	7827	1497	1517	281 (2 < m < 15 GeV)
	2 → 4	4389	582	----	----
	5 → 8	1457	275	1136	276
	8 → 11	536	19	318	6.4
	11 → 25	143	4	54	0 (11 < m < 15 GeV)
44 GeV	$d\sigma/dm$ (2 < m < 17 GeV)	1509	284	608	140 (2 < m < 11 GeV)
	2 → 4	897	126	----	----
	5 → 8	259	26	168	28
	8 → 17	77	1	31	0 (8 < m < 11 GeV)

NOTE: Due to limited acceptance and statistics, the CDC Analysis does not present any results in the 2 → 4 GeV mass range.

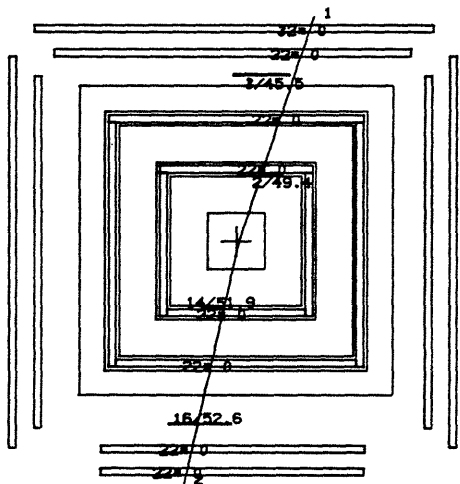
FIGURE III-1 A COSMIC RAY



Side View

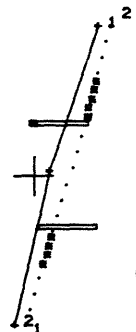
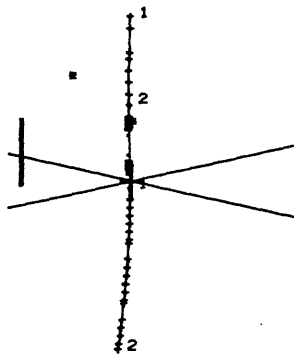
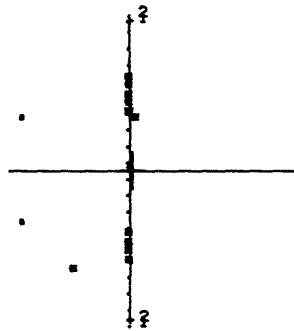


Top View



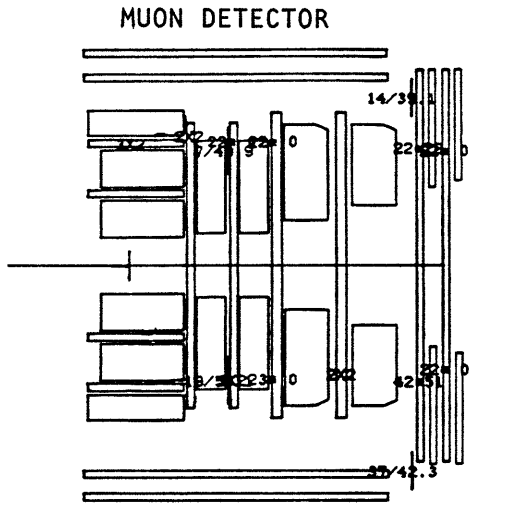
Rear View

INNER DETECTOR

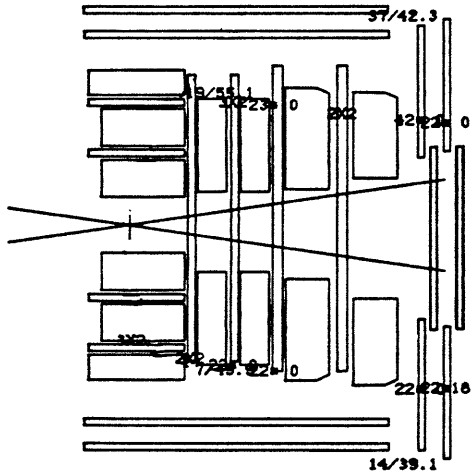


RUN NO 1497 EVENT 10080
 MASS=28.214 PPERP= 5.062 XF=-.006
 P1= 13.13 X1= 4.82 P2=-15.20 X2= 9.43
 BDL1= 25.96 BDL2= 25.77

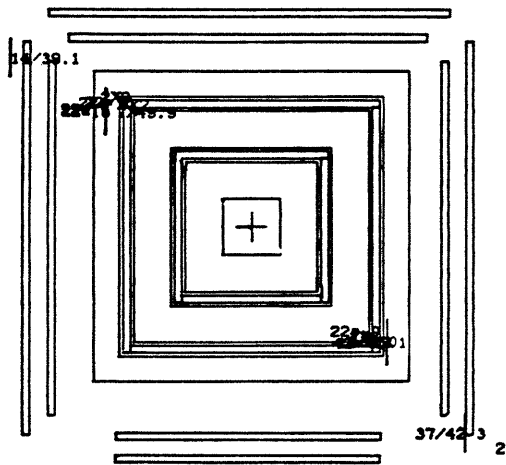
FIGURE III-2 A TYPICAL "13 MUON" EVENT



Side View

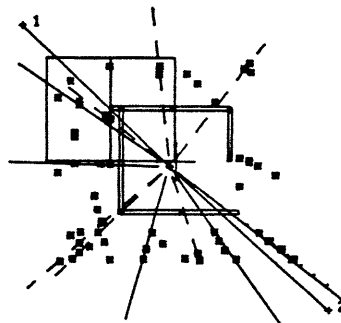
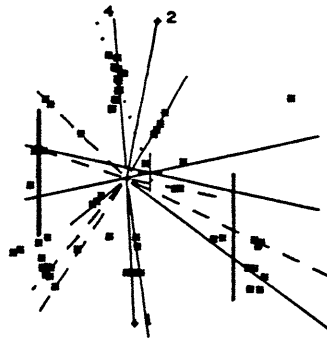
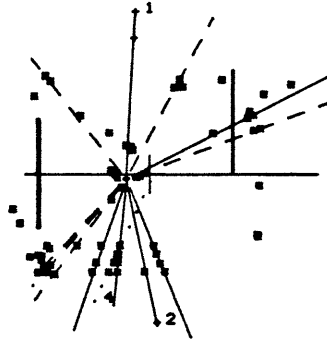


Top View



Rear View

INNER DETECTOR



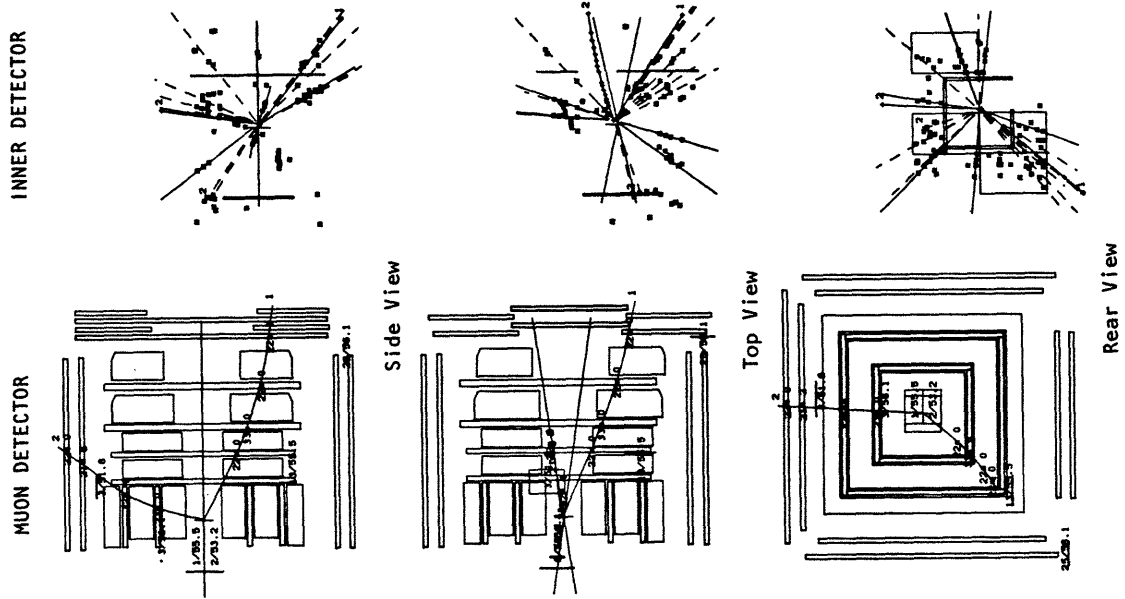
RUN NO 744 EVENT 1977
 MASS= 5.736 PPERP= 1.383 XF=0.030
 P1= 2.54 X1= 3.48 P2= 3.31 X2= 3.76
 BDL1= 13.11 BDL2= 19.76

FIGURE III-3 LIKE-SIGN DIMUON EVENTS

RUN NO 547 EVENT 11010

MASS= 6.045 PPERP= 0.799 XF=0.186
 P1= 6.00 X1= 0.98 P2= 2.53 X2= 5.10
 BDL1= 43.10 BDL2= 23.06

b) A Focused-focused Event



RUN NO 543 EVENT 4204

MASS= 3.037 PPERP= 0.713 XF=0.249
 P1= -5.97 X1= 3.11 P2= -2.41 X2= 0.79
 BDL1= 39.84 BDL2= 29.86

a) A Defocused-defocused Event

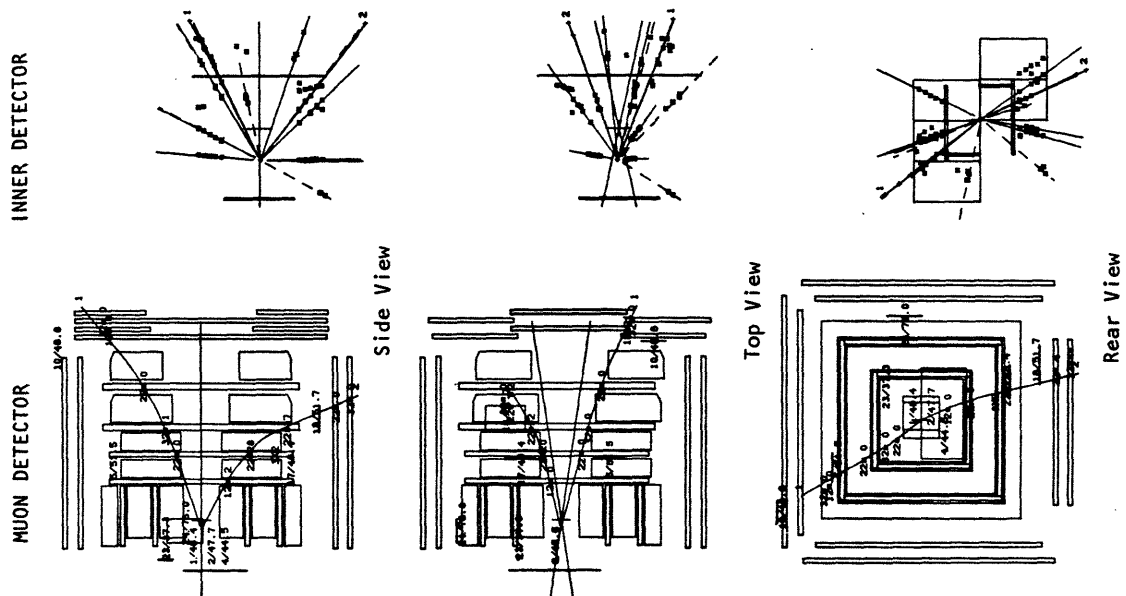
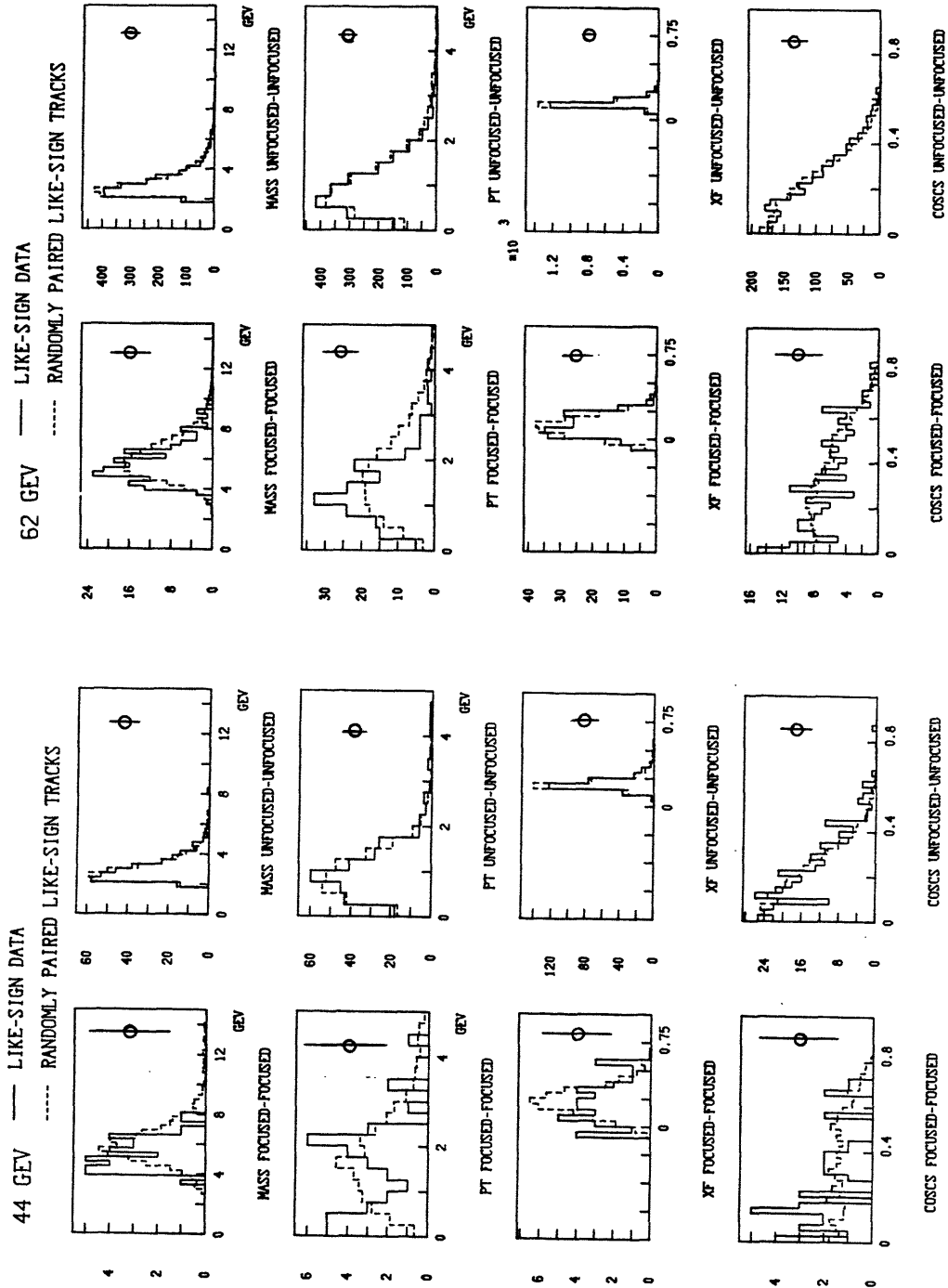


FIGURE III-4 BACKGROUND INVESTIGATION



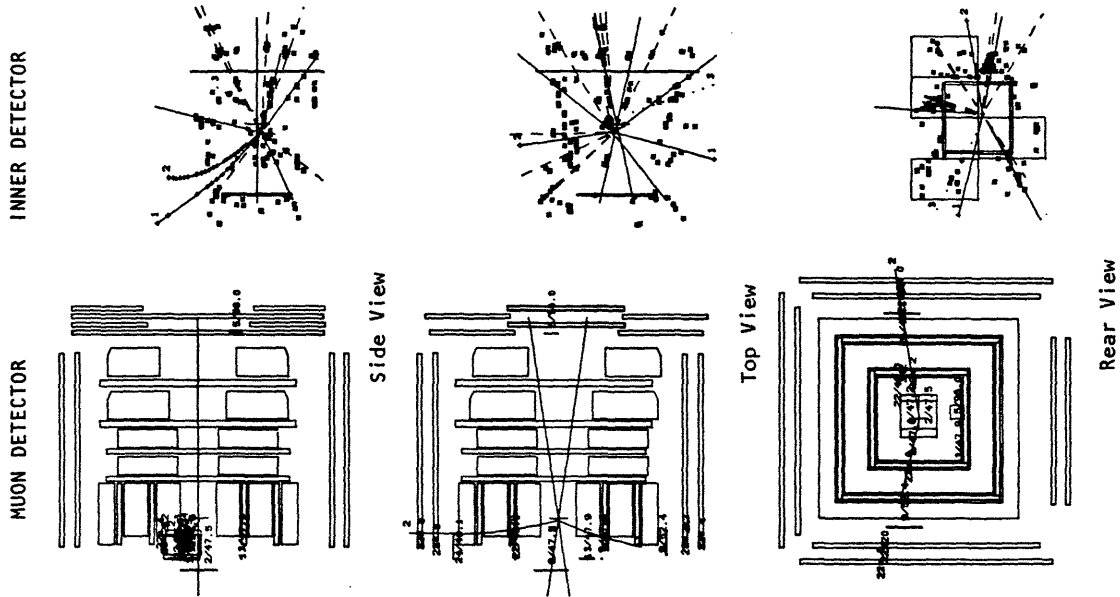
Provided that background tracks are not correlated, the like-sign distributions should match those of randomly paired like-sign tracks, as sketched above. One sample error-bar is drawn on each plot to illustrate the statistical significance of the like-sign data. See Sec. III-4.

FIGURE - III-5 TYPICAL EVENTS ELIMINATED BY THE BDL CUT

RUN NO 559 EVENT 12043

MASS= 5.899 PPERP= 2.897 XF=-.064
 P1= 2.45 X1= 40.67 P2= 4.13 X2= 66.81
 BDL1= 17.65 BDL2= 26.52

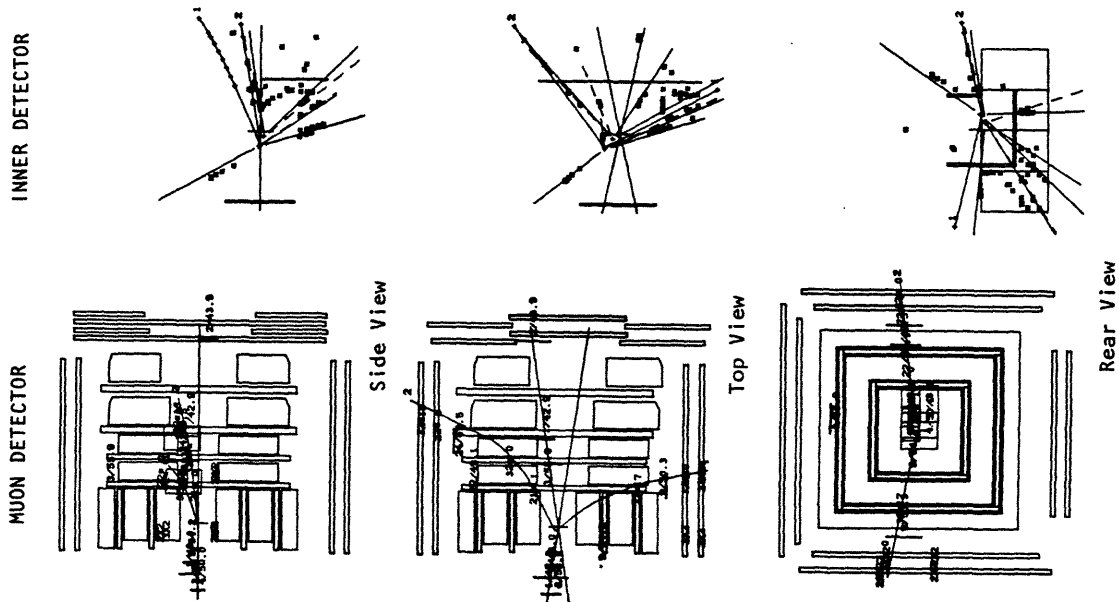
b) A "Seagull" Event



RUN NO 542 EVENT 7905

MASS= 2.532 PPERP= 0.554 XF=0.110
 P1= -1.97 X1= 0.39 P2= -2.36 X2= 1.61
 BDL1= 17.50 BDL2= 29.47

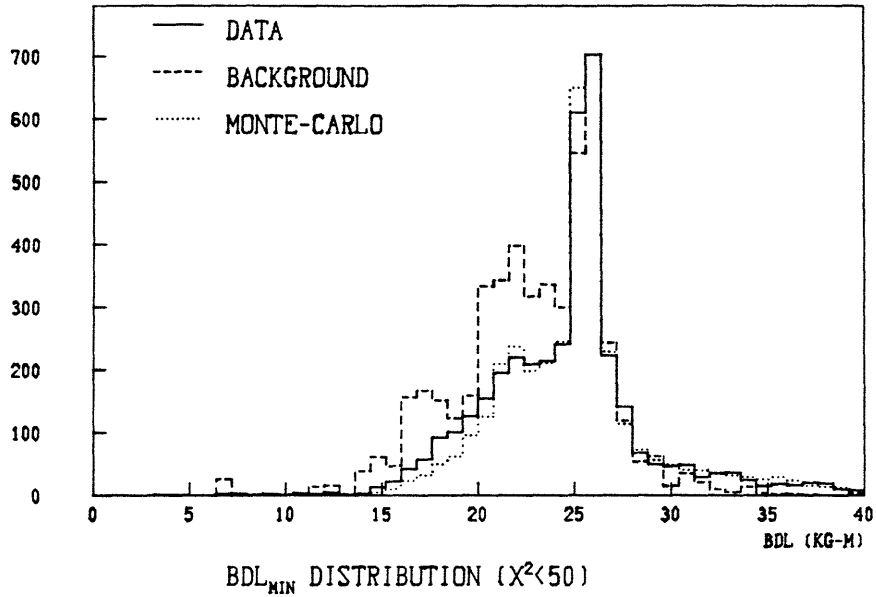
a) A "Chimney" Event



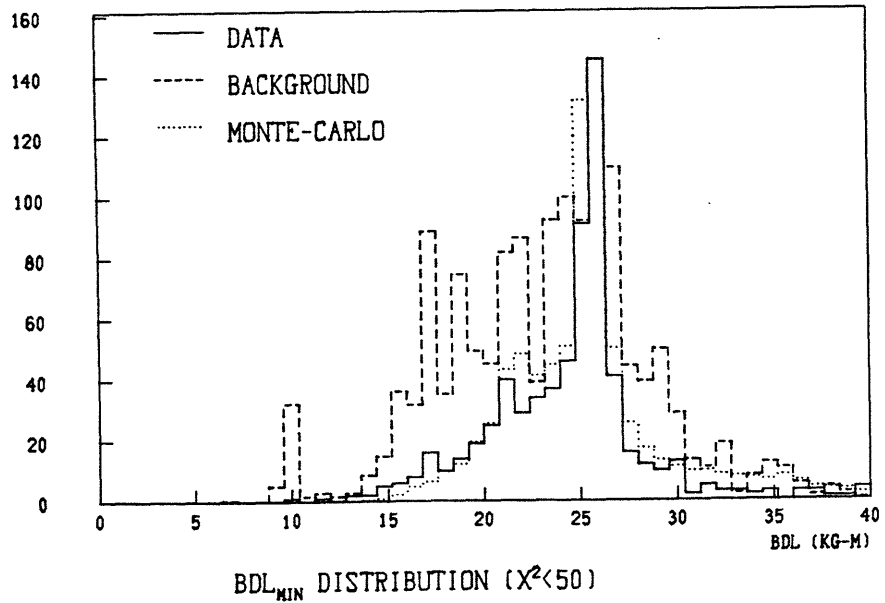
In both events, Muon #1 escapes the detector without traversing sufficient iron.

FIGURE III-6 BDL DISTRIBUTIONS

62 GEV DATA - $M > 4.5$ GEV



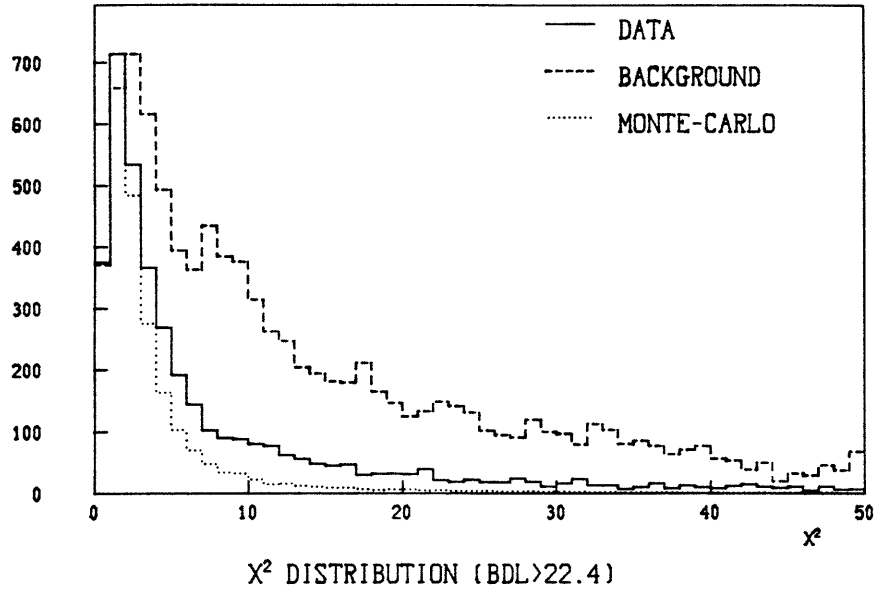
44 GEV DATA - $M > 4.5$ GEV



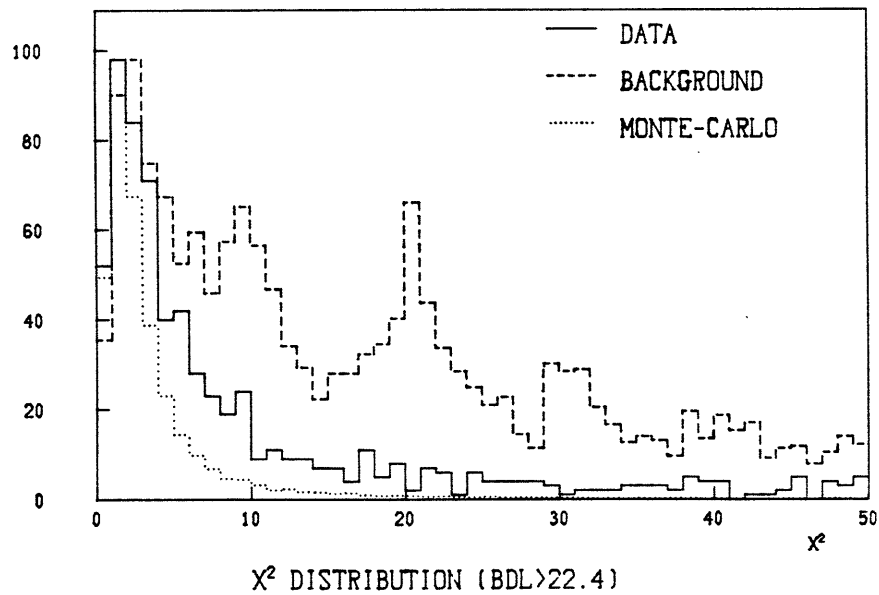
The data, background, and Monte-Carlo are all normalized to the same peak value, thus are not plotted on a common scale (the scale on the vertical axis is for the data). The cut $Bdl > 22$ can be seen to cut a greater percentage of background than data. See Sec. III-6 part b.

FIGURE III-7 χ^2 DISTRIBUTIONS

62 GEV DATA - $M > 4.5$ GEV

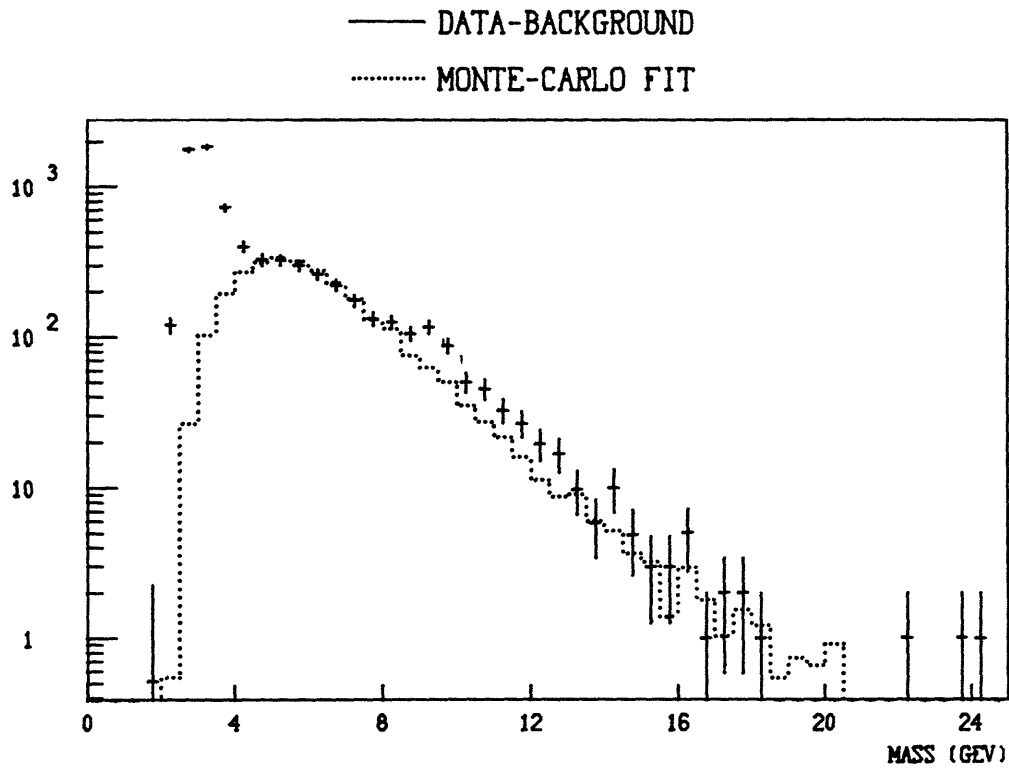


44 GEV DATA - $M > 4.5$ GEV

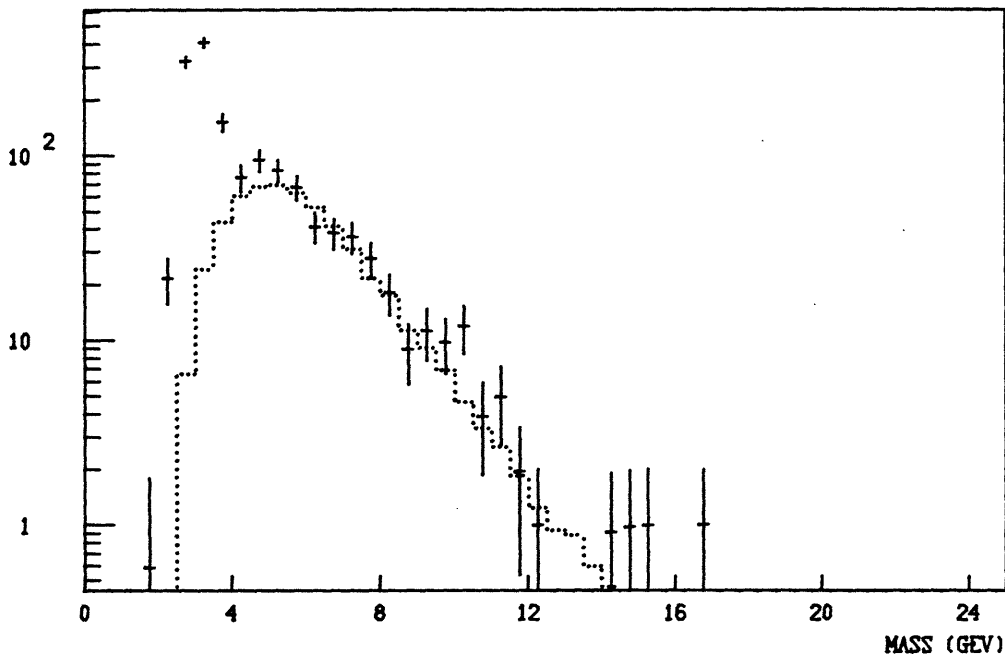


The data, background, and Monte-Carlo are all normalized to the same peak value, thus are not plotted on a common scale (the scale on the vertical axis is for the data). The higher χ^2 tail of the background is evident. See Sec. III-6 part b.

FIGURE III-8 Mass: Data-Background vs. Fitted Monte Carlo



MASS - 62 GEV DATA



MASS - 44 GEV DATA

FIGURE III-11 $\cos\theta_{CS}$: Data-Background vs. Fitted Monte Carlo

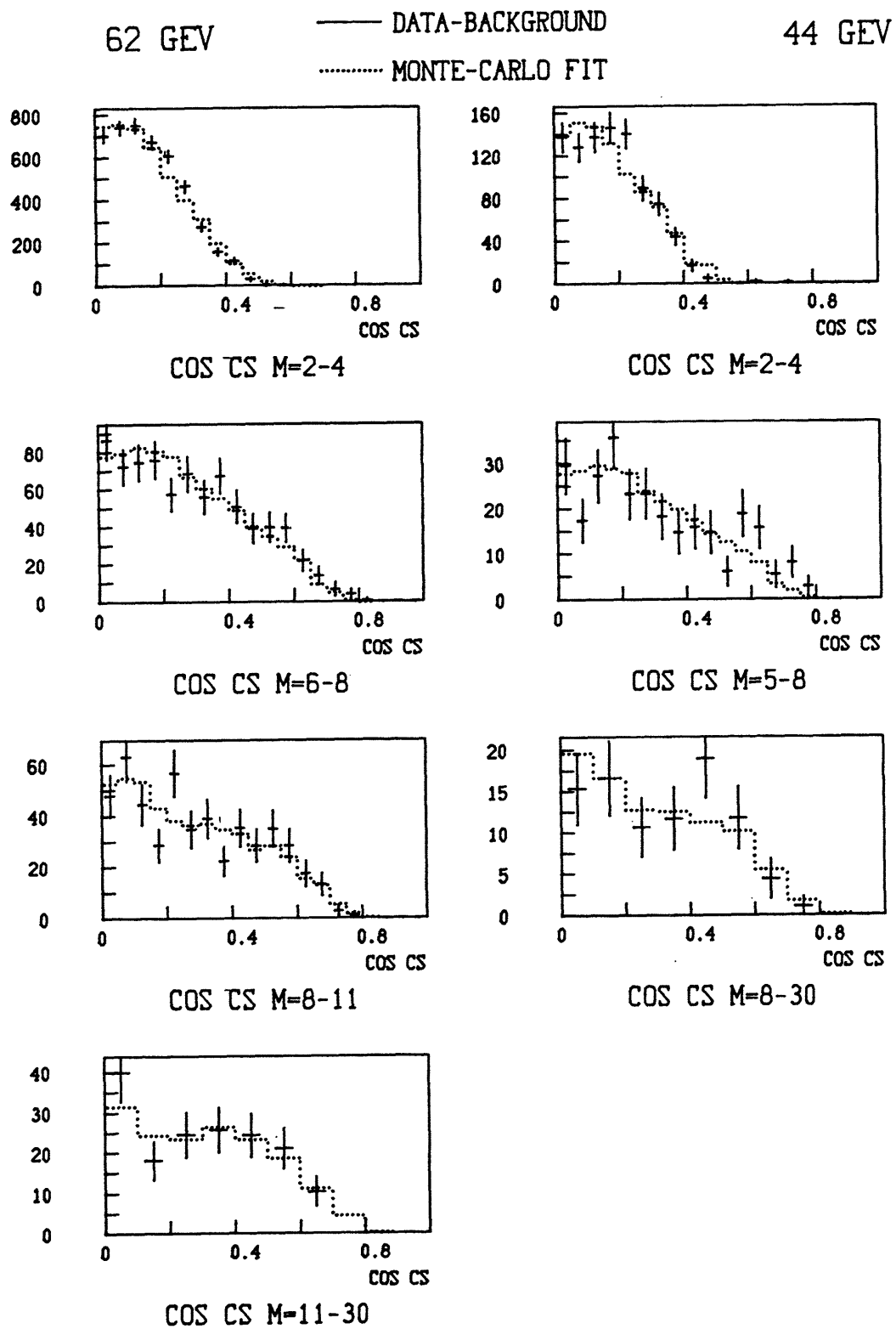


FIGURE III-12 MASS ANALYSIS $\sqrt{s} = 62$ GeV

● DATA
 ■ BACKGROUND

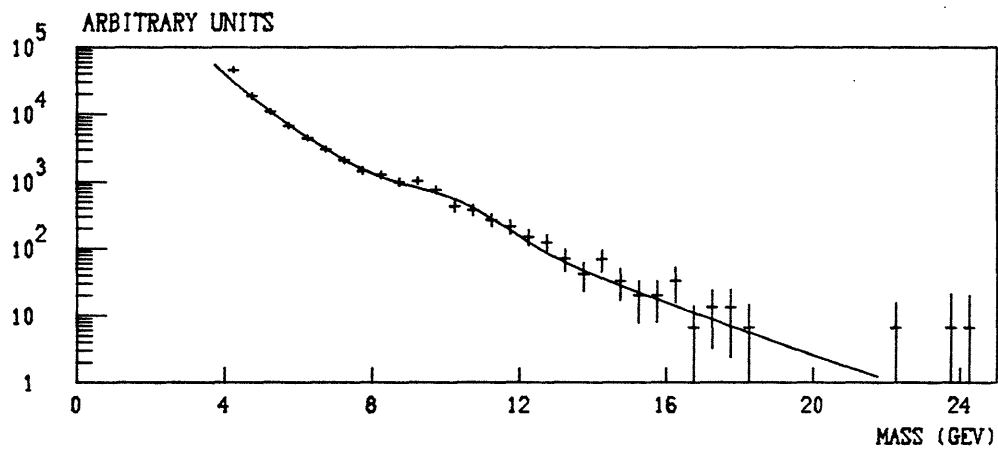
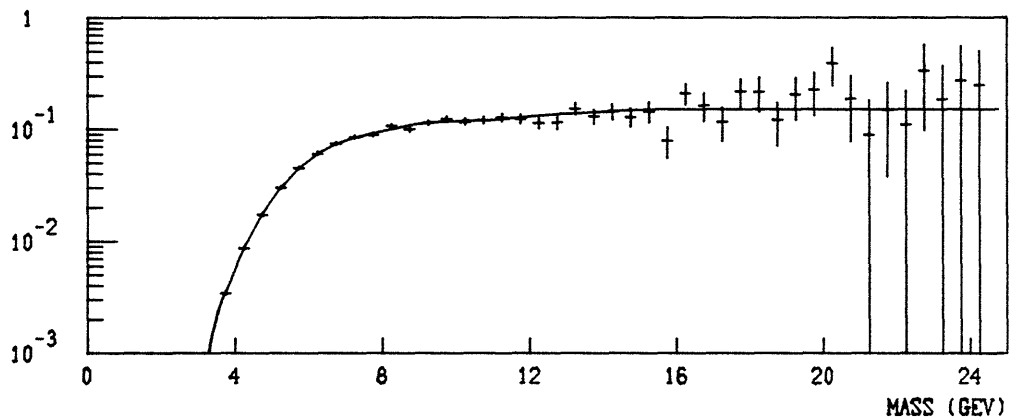
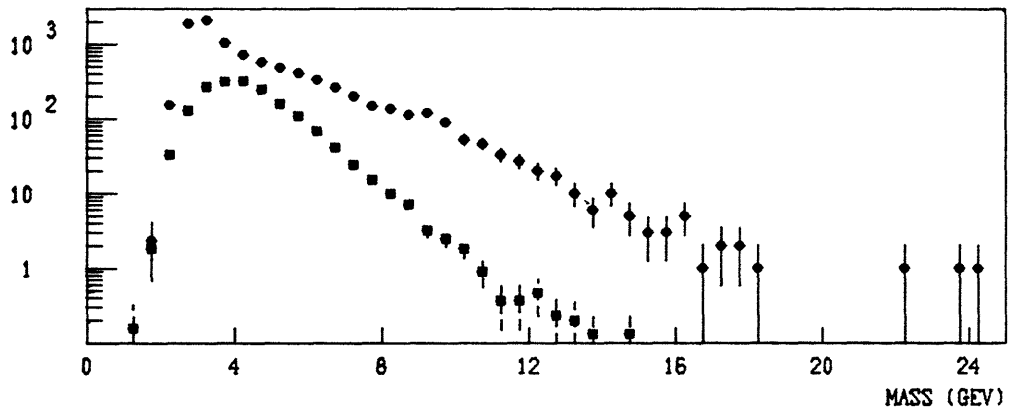


FIGURE III-13 MASS ANALYSIS $\sqrt{s} = 44$ GeV

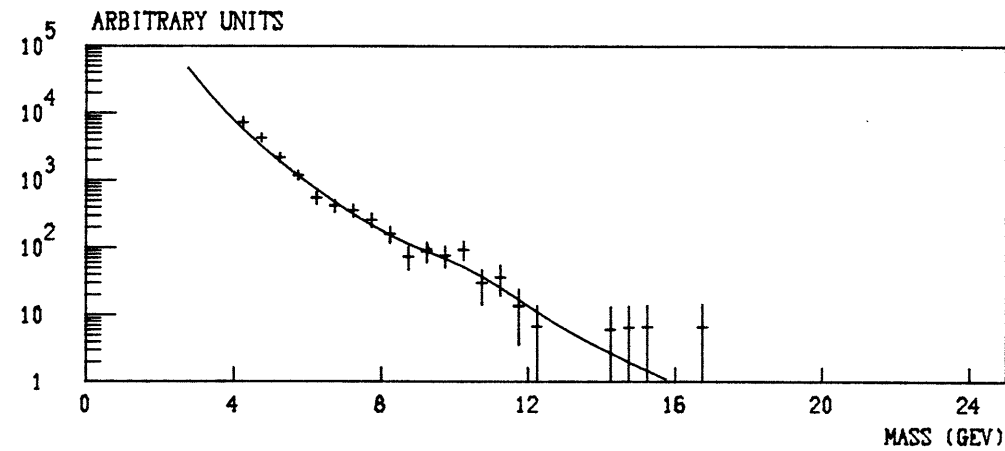
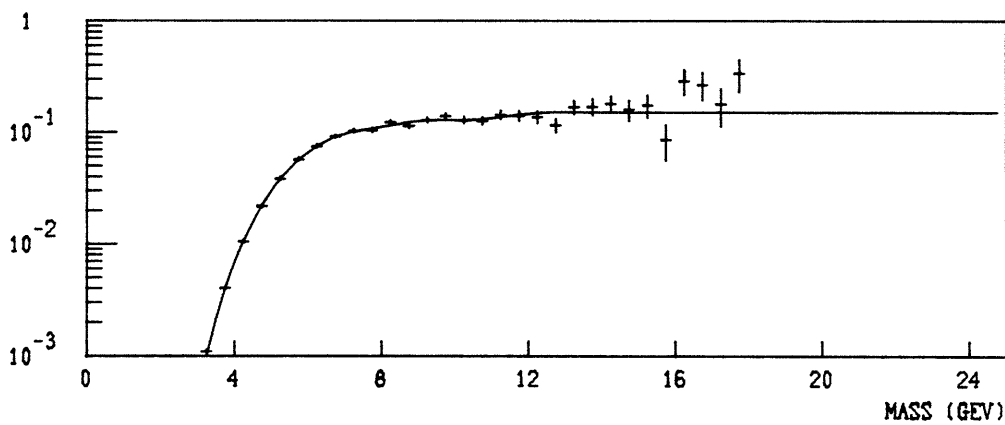
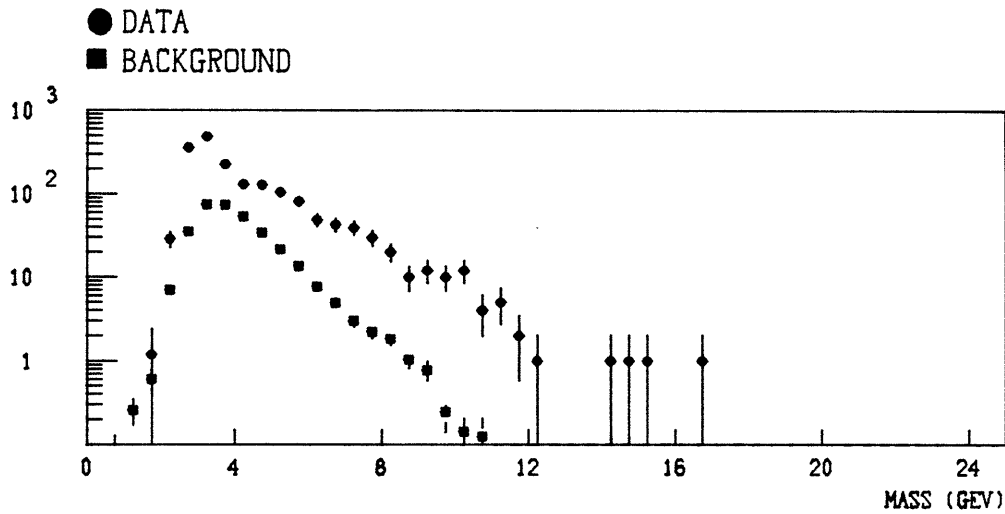


FIGURE-III-14 P_T ANALYSIS

$\sqrt{s}=62$ Gev

ARBITRARY UNITS

● DATA
■ BACKGROUND

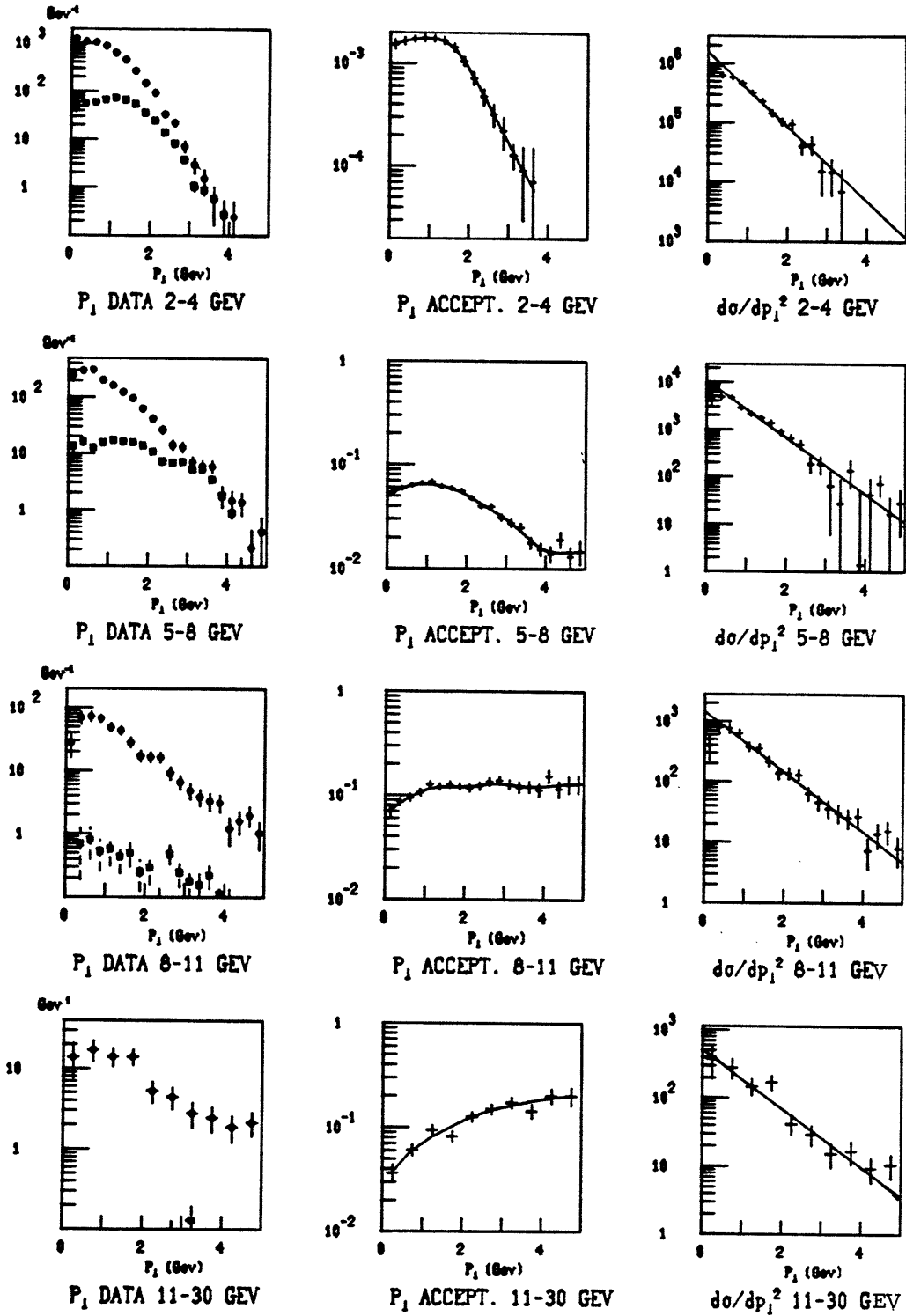


FIGURE III-15 P_T ANALYSIS

$\sqrt{s}=44 \text{ Gev}$

ARBITRARY UNITS

● DATA
■ BACKGROUND

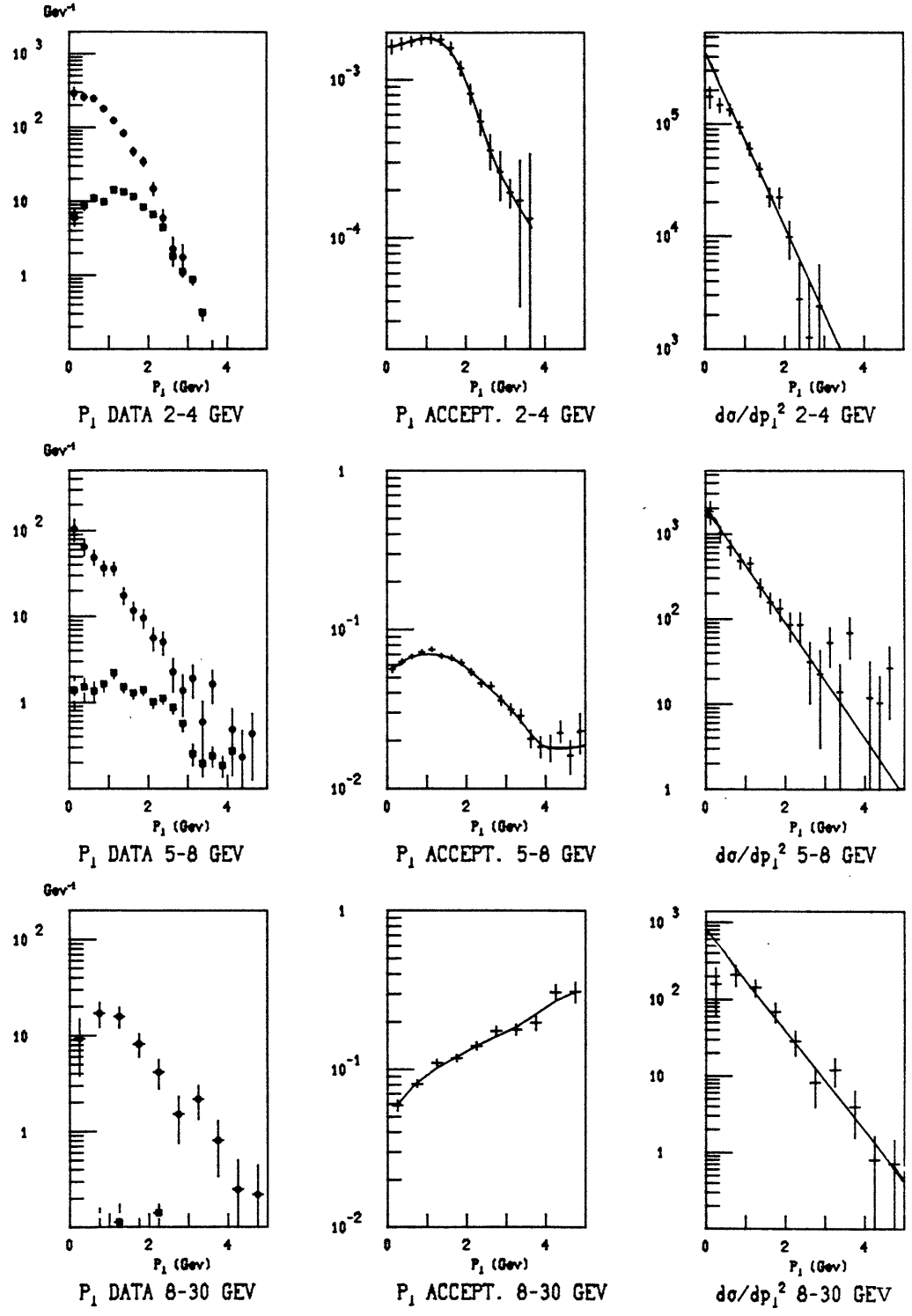
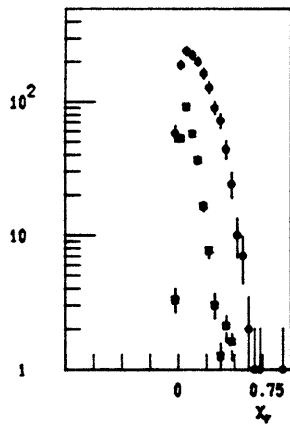


FIGURE III-16 X_F ANALYSIS

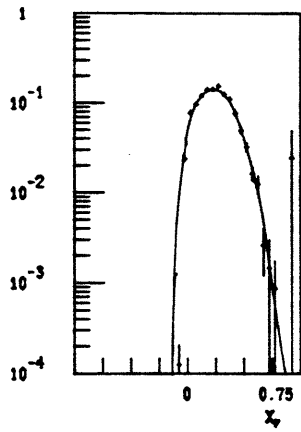
● DATA
 ■ BACKGROUND

$\sqrt{s}=62$ Gev

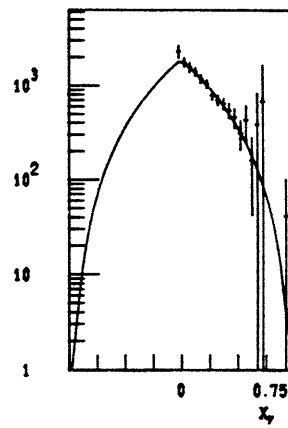
ARBITRARY UNITS



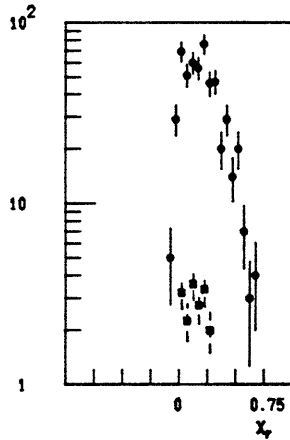
X_F DATA 5-8 GEV



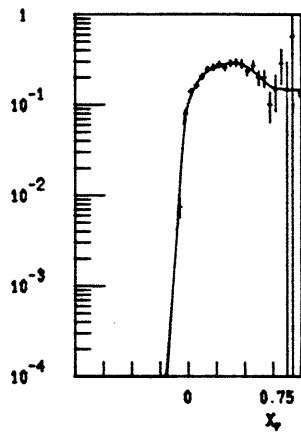
X_F ACCEPT. 5-8 GEV



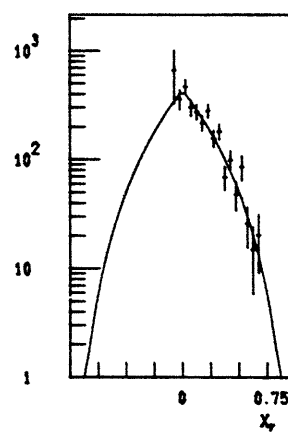
$d\sigma/dx_F$ 5-8 GEV



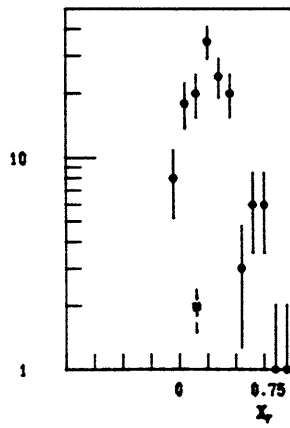
X_F DATA 8-11 GEV



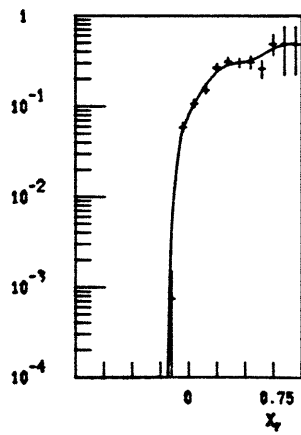
X_F ACCEPT. 8-11 GEV



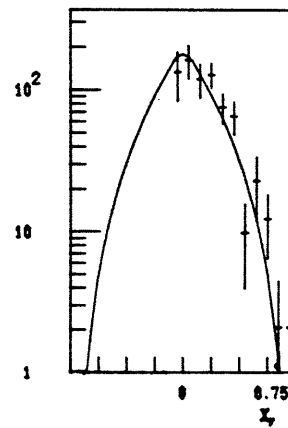
$d\sigma/dx_F$ 8-11 GEV



X_F DATA 11-30 GEV



X_F ACCEPT. 11-30 GEV



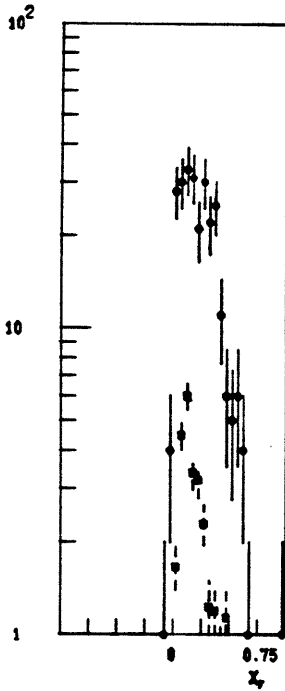
$d\sigma/dx_F$ 11-30 GEV

FIGURE III-17 X_F ANALYSIS

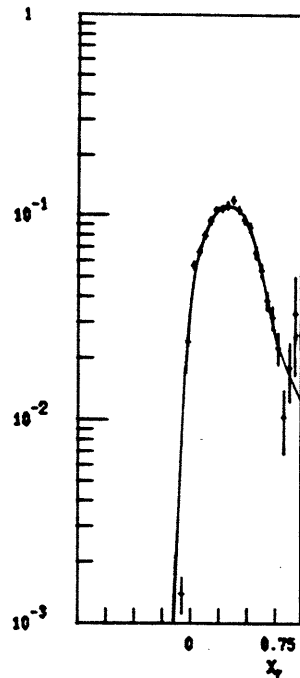
● DATA
 ■ BACKGROUND

$\sqrt{s}=44$ GeV

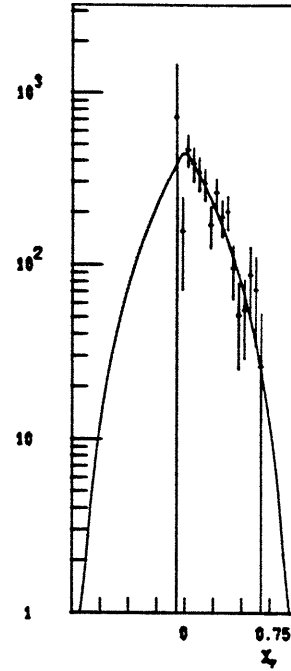
ARBITRARY UNITS



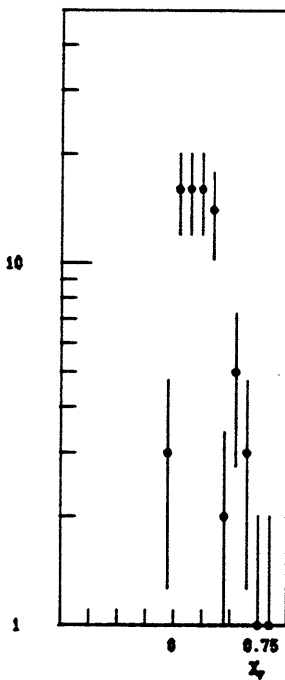
X_F DATA 5-8 GEV



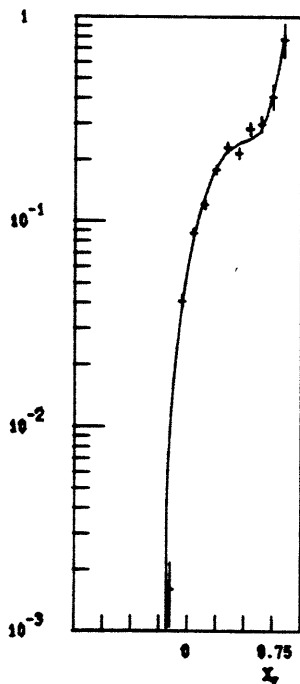
X_F ACCEPT. 5-8 GEV



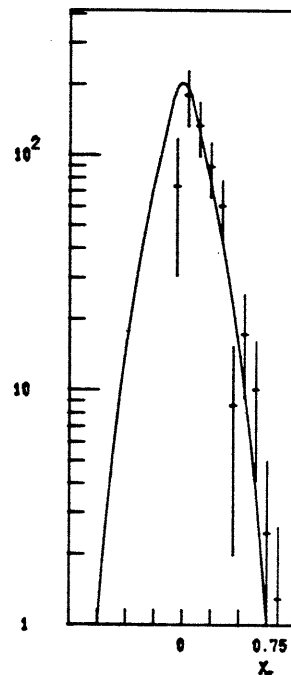
$d\sigma/dx_F$ 5-8 GEV



X_F DATA 8-30 GEV



X_F ACCEPT. 8-30 GEV



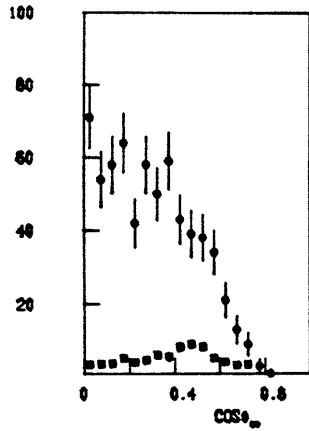
$d\sigma/dx_F$ 8-30 GEV

FIGURE III-18 $\cos\theta_{CS}$ ANALYSIS

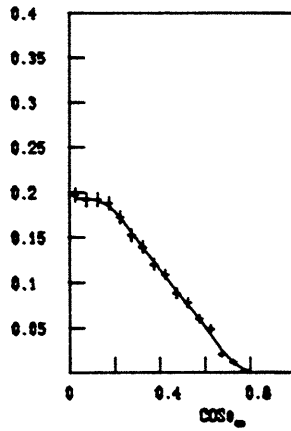
● DATA
■ BACKGROUND

$\sqrt{s}=62$ GeV

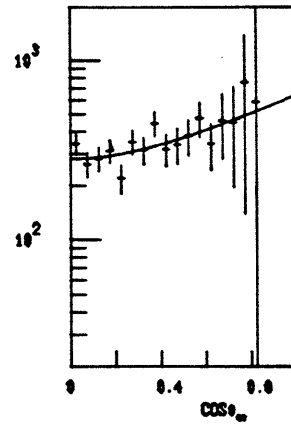
ARBITRARY UNITS



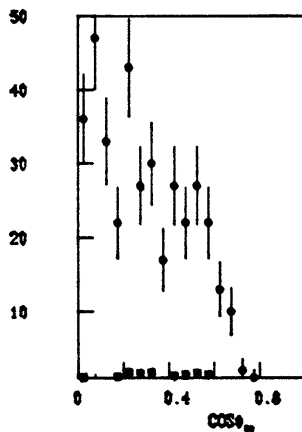
$\cos\theta_{CS}$ 6-8 GEV



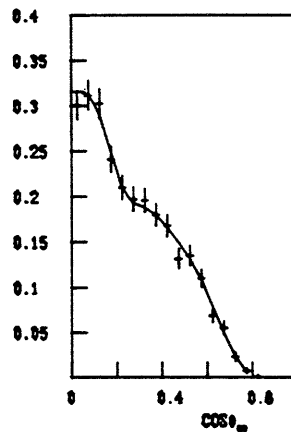
$\cos\theta_{CS}$ ACCEPT. 6-8 GEV



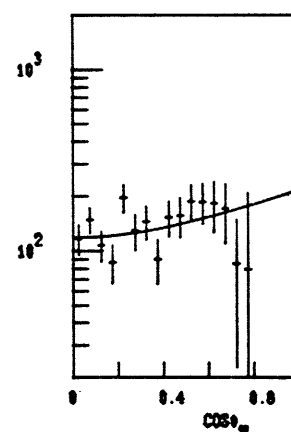
$d\sigma/d\cos\theta_{CS}$ 6-8 GEV



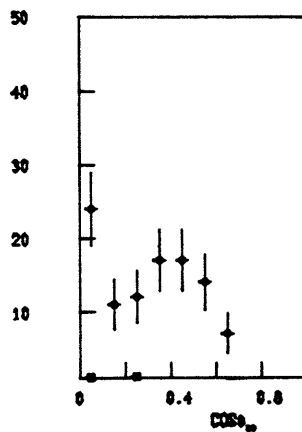
$\cos\theta_{CS}$ 8-11 GEV



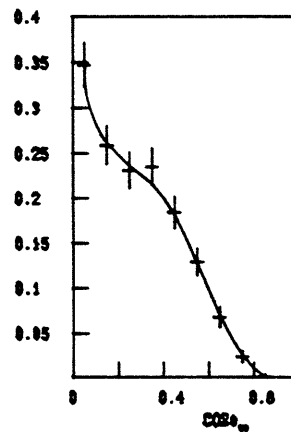
$\cos\theta_{CS}$ ACCEPT. 8-11 GEV



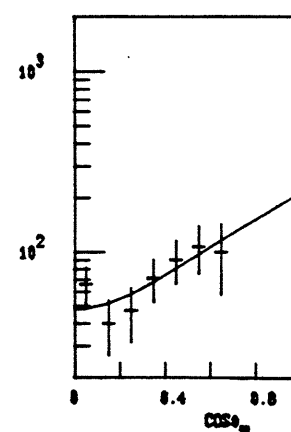
$d\sigma/d\cos\theta_{CS}$ 8-11 GEV



$\cos\theta_{CS}$ 11-30 GEV



$\cos\theta_{CS}$ ACCEPT. 11-30 GEV



$d\sigma/d\cos\theta_{CS}$ 11-30 GEV

FIGURE III-19 $\cos\theta_{CS}$ ANALYSIS

● DATA
■ BACKGROUND

$\sqrt{s}=44$ GeV

ARBITRARY UNITS

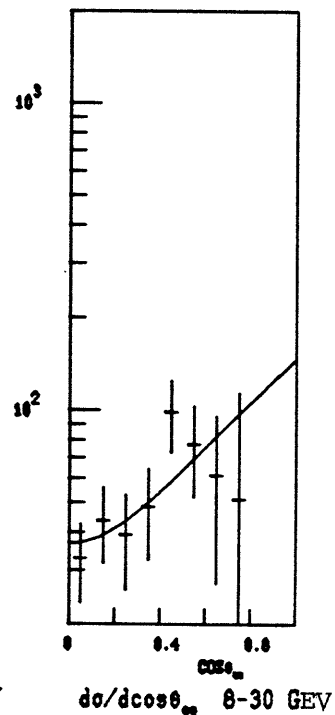
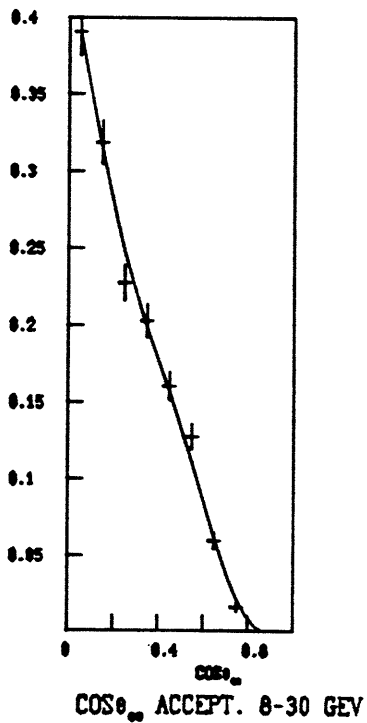
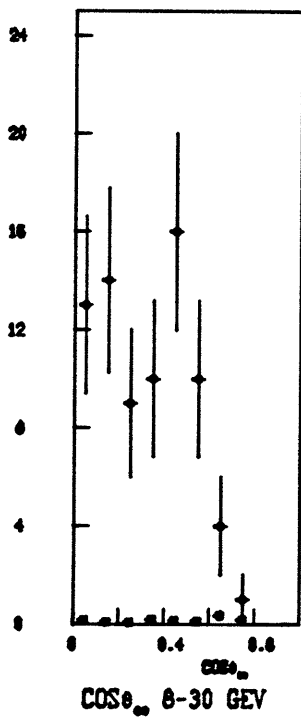
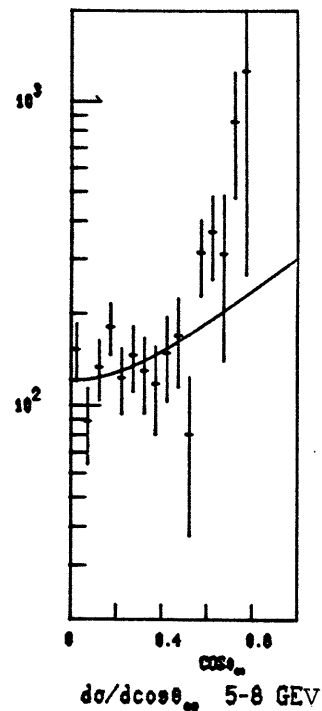
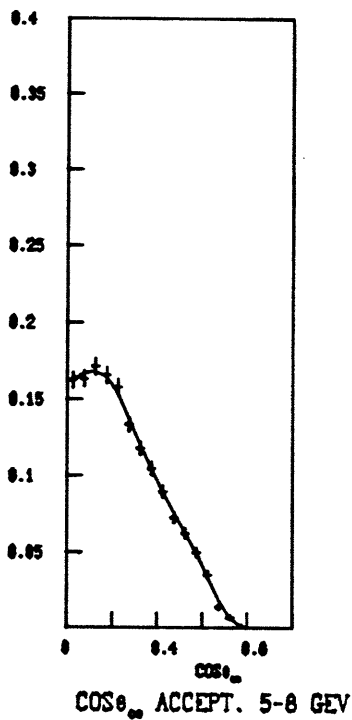
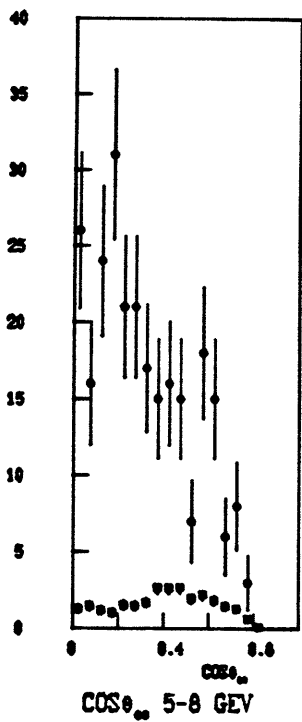
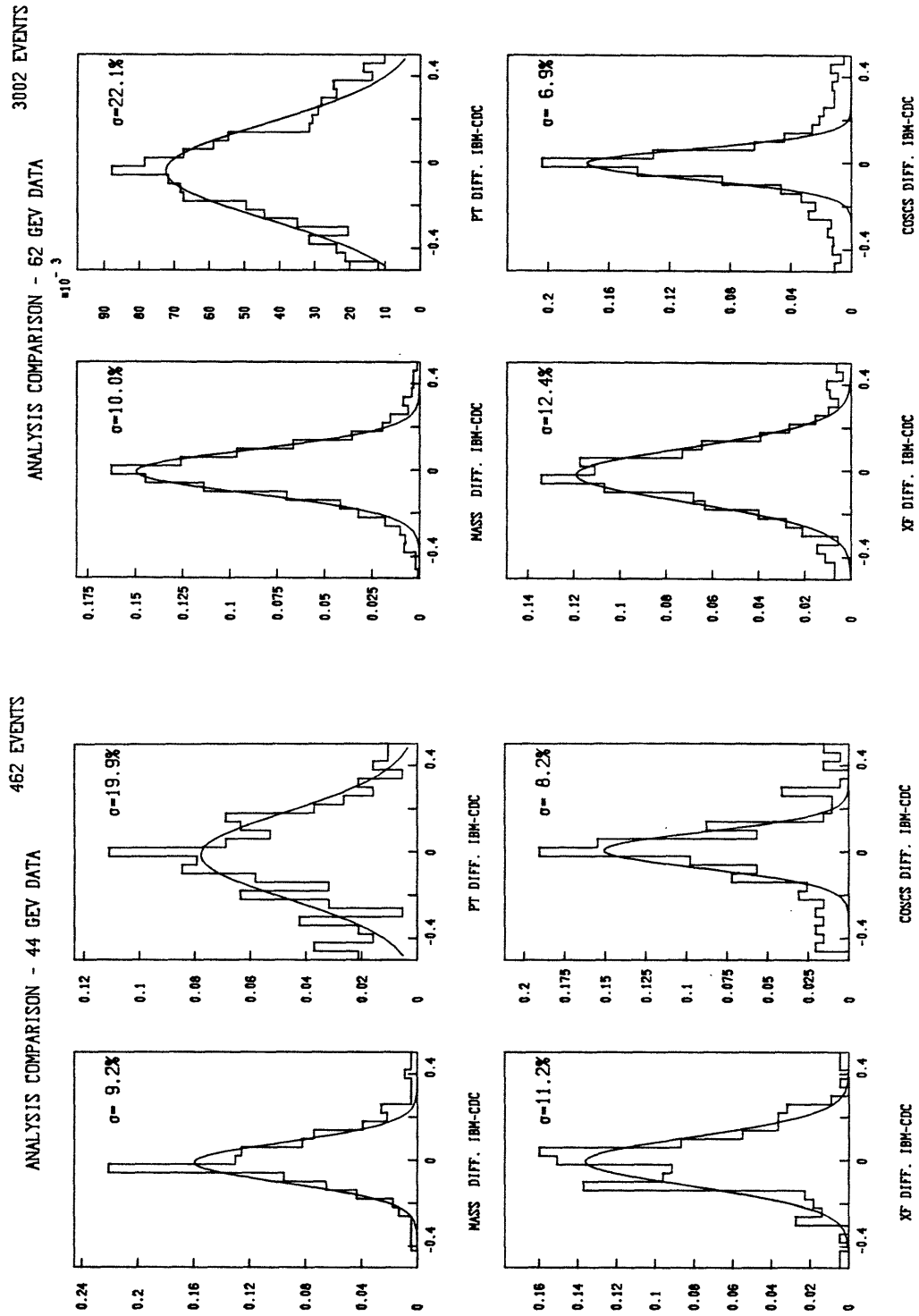


FIGURE III-20 ANALYSIS COMPARISON



These histograms present the percentage difference between the two analyses.
See Sec. III-8.

SECTION IV RESULTS

IV-1) The Mass Spectra

a) Parameterization

Figure IV-1 shows the spectra $d\sigma/dm$ of the observed muon pairs at $\sqrt{s} = 62$ and 44 GeV. We have fit the data at each energy to the form¹⁾:

$$\text{Eq. IV-1)} \quad \frac{d\sigma}{dm} = A \frac{(1-m/\sqrt{s})^{10}}{m^4/\sqrt{s}} + B \cdot F_T(m)$$

where $F_T(m)$ is a sum of gaussian distributions caused by the $\sigma_m = 11.5\%$ mass resolution at the T, T', and T'' masses, ie:

$$\text{Eq. IV-2)} \quad F_T(m) = e^{-\frac{1}{2} \left(\frac{m - m_0}{m_0 \sigma_m} \right)^2} + 0.31 \cdot e^{-\frac{1}{2} \left(\frac{m - m_1}{m_1 \sigma_m} \right)^2} + 0.15 \cdot e^{-\frac{1}{2} \left(\frac{m - m_2}{m_2 \sigma_m} \right)^2}$$

$$m_0 = 9.46 \text{ GeV} \quad m_1 = 10.02 \text{ GeV} \quad m_2 = 10.30 \text{ GeV}$$

The masses and relative branching ratios of the T family are taken from the data of reference 2. Eq. IV-1 is fit to all points with $4.5 < m < 20$ GeV. The resulting A and B values are:

$\sqrt{s} = 62 \text{ GeV}$	$\sqrt{s} = 44 \text{ GeV}$
$A = 5.76 \pm .17 \text{ nb} \cdot \text{GeV}^2$	$A = 5.47 \pm .34 \text{ nb} \cdot \text{GeV}^2$
$B = 3.65 \pm .55 \text{ pb/GeV}$	$B = 0.69 \pm .42 \text{ pb/GeV}$
$\chi^2/\text{DF} = 16.3/26$	$\chi^2/\text{DF} = 16.7/18$

The continuum portion of these fits (ie. $B \equiv 0$) is drawn on Fig. IV-1. The cross-sections $d\sigma/dm$ are listed in Table IV-1. We have assigned a systematic normalization error of 10% to these measurements, based on studies of dependence upon the assumed production model in acceptance calculation, investigations into background sensitivity, and luminosity error (see Appendix II).

b) Resonances

By integrating $F_T(m)$ in Eq. IV-2, cross-sections for the T family are obtained. Using the fitted B values and correcting for the steeper X_F dependence and isotropic angular distribution measured at the T (see Secs.

IV-2, IV-3, and App. II), we receive:

$$\sigma (T + T' + T'' \rightarrow \mu^+ \mu^-) = \begin{array}{l} 10.6 \pm 3.5 \text{ pb at } \sqrt{s} = 62 \text{ GeV} \\ 2 \pm 2 \text{ pb at } \sqrt{s} = 44 \text{ GeV} \end{array}$$

I have also fit Eq. IV-1 without fixing the exponent on $(1 - m/\sqrt{s})$, allowing it to be determined by the data. The results do not differ significantly from the exponent of 10 predicted in ref. 1 and are portrayed in Appendix II. I have widened the errors allotted to the above cross-sections to account for the B values from these "free exponent" fits.

The mass spectrum in Figure IV-1 was obtained as described in Sec. III for $m > 4$ GeV. Below this mass, the data is dominated by $J \rightarrow \mu^+ \mu^-$ at 3.1 GeV, smeared by the 11% mass resolution. In order to calculate the cross-section in this region, we first subtracted contributions from background (as described in Sec. III-6) and continuum events (based on the fit in eq. IV-1, propagated through acceptance and extrapolated to $m < 4$ GeV) from the total $\mu^+ \mu^-$ data, thus obtaining a sample of pure J events. This process is sketched in Fig. II-9. An acceptance at 3.1 GeV was calculated by taking the ratio of total accepted/generated Monte-Carlo events with generated mass between 3.05 and 3.15 GeV; these were weighted to an isotropic angular distribution as observed in previous experiments.³⁾ The distribution of pure J events was divided by this acceptance and added onto an extrapolation of the continuum for $m < 4$ GeV via the fit of Eq. IV-1, yielding the result in Fig. IV-1.

The J cross-section is obtained by integrating $d\sigma/dm$ between $2 \rightarrow 4$ GeV and subtracting the continuum contribution. Due to the limited range of acceptance (see Sec. II-3), we measure J's produced with $0.1 < X_F < 0.35$; thus we have removed the assumed X_F dependence from the acceptance calculations, and present $d\sigma/dX_F$ at $\langle X_F \rangle = 0.2$:

$$\frac{d\sigma (J \rightarrow \mu^+ \mu^-)}{dX_F} \Big|_{\langle X_F \rangle = 0.2} = \begin{array}{l} 41 \pm 12 \text{ nb at } \sqrt{s} = 62 \text{ GeV} \\ 15 \pm 10 \text{ nb at } \sqrt{s} = 44 \text{ GeV} \end{array}$$

The quoted errors include systematic uncertainty from acceptance and luminosity measurement.

The J and T cross-sections have been plotted* in Fig. IV-2 along with the results of other experiments† as a function of $\sqrt{\tau} = m/\sqrt{s}$. The curves are derived from our continuum fit, and have the form $(1 - \sqrt{\tau})^{10}/\sqrt{\tau}$, arbitrarily normalized to the data points. The general agreement of the data with these curves indicates that the J and T cross-sections scale with $\sqrt{\tau}$ in a fashion similar to the continuum.

At $\sqrt{s} = 62$ GeV, we find 3 events with mass over 20 GeV, while only one would be expected by integrating the continuum fit. This allows us to set an upper limit on production of new resonances "X" with $m_X > 20$ GeV of:

$$\sigma (X \rightarrow \mu^+ \mu^-) \leq 40 \cdot 10^{-38} \text{ cm}^2$$

at a 95% confidence level.

c) Scaling Comparison

As mentioned in Sec. I, the phenomenon of scaling (ie. $m^3 d^2\sigma/dm dX_F = F(\tau)$) is a direct consequence of the Drell-Yan formula. Figure IV-3 portrays $d^2\sigma/dm dX_F$ at $X_F=0$ as a function of $\sqrt{\tau}$ for our data at 62 and 44 GeV, together with the 27.4 GeV data from ref. 4. The J and T regions ($m < 4.5$ and $8 < m < 12.5$ GeV) are excluded. I have extrapolated our data to $X_F=0$ by:

$$\text{Eq. IV-4) } \left. \frac{d^2\sigma}{dm dX_F} \right|_{X_F=0} = \frac{d\sigma}{dm} \left(\frac{\beta+1}{2} \right) \quad \text{assuming: } \frac{d\sigma}{dX_F} \propto (1 - |X_F|)^\beta$$

The value $\beta=2.5$ is taken for both 62 and 44 GeV as an average† over the continuum (see Sec. IV-2). The CFS data was converted from $y=0$ to $X_F=0$ by means of eq. IV-3.

*) The cross-sections are plotted in the form $d\sigma/dX_F$ at $X_F = 0$. In the T region, the measured X_F distributions are used to convert the data (see Sec. IV-2). In the J region, I have assumed the form $(1 - |X_F|)^\beta$, with $\beta = 4.0$ for 62 GeV and $\beta = 3.5$ for 44 GeV. The error bars have been widened by 20% to account for possible inaccuracy in this assumption.

†) For results given in the form $d\sigma/dy$ at $y = 0$, where y is the rapidity variable (see App. I), I have used the relation:

$$\text{Eq. IV-3) } \left. \frac{d\sigma}{dX_F} \right|_{X_F=0} = \frac{\sqrt{s}}{2m} \left. \frac{d\sigma}{dy} \right|_{y=0}$$

+) The variation of β over the mass range considered will have under 15% effect on eq. IV-4.

The 62 and 44 GeV data overlap between $0.10 < \sqrt{\tau} < 0.13$, and in this region the coincidence of the plotted values support scaling within experimental significance. For $\sqrt{\tau} \approx 0.2 \rightarrow 0.3$, our 62 GeV data overlaps with the 27.4 GeV Fermilab data. Although the cross-sections differ by two orders of magnitude, we can see no significant* scaling violations.

We have constructed an $F(\tau)$ based on the continuum term of eq. IV-1:

$$\text{Eq. IV-5)} \quad m^3 \frac{d^2\sigma}{dm dX_F} = F(\tau) = C(1 - \sqrt{\tau})^{10}/\sqrt{\tau}$$

The C values have been fit to the data as plotted in Fig. IV-3, Fits are made separately at $\sqrt{s} = 62$ and 44 GeV. The results of both fits are listed and their corresponding curves are drawn on the figure. The agreement between C_{62} and C_{44} supports the use of scaling ansatz eq. IV-5 in this energy range.

We have also plotted the 27.4 GeV fit of ref. 5, which becomes:

$$\text{Eq. IV-6)} \quad m^3 \left. \frac{d^2\sigma}{dm dX_F} \right|_{X_F=0} = (27.8 \cdot 10^{-30}) \tau e^{-26.6\sqrt{\tau}} \text{ cm}^2 \cdot \text{GeV}^2$$

Observing Fig. IV-3, it can be seen that eq. IV-6 does not describe our data at smaller τ and can not be extended into the region $\sqrt{\tau} < 0.2$.

d) Comparison with the Drell-Yan Formula

The Drell-Yan model was introduced in Section I, and Eq. I-1 states the resulting cross-section for $d^2\sigma/dmdX_F$. By using the proton structure functions adapted from the deep-inelastic neutrino scattering data of Ref. 6 as quoted in Ref. 7.

$$\begin{aligned} \text{Eq. IV-7)} \quad u_v(x) &= 2.13 \sqrt{x} (1-x)^{2.8} \\ d_v(x) &= 1.26 \sqrt{x} (1-x)^{3.8} \\ \bar{u}(x) &= \bar{d}(x) = 0.27 (1-x)^{8.1} \\ s(x) &= \bar{s}(x) = \frac{1}{4} (\bar{u}(x) + \bar{d}(x)) \end{aligned}$$

(Sea contributions from charmed and heavier quarks are assumed negligible)

*) The ISR data seems to be systematically higher than the corresponding Fermilab data in this region, but the difference is within our experimental error and the 25% systematic normalization error quoted in ref. 4.

the Drell-Yan cross-section can be calculated from Eqs. I-1 and IV-7 (setting $X_F = 0$).

$$\text{Eq. IV-8) } \left. \frac{d^2\sigma}{dm dX_F} \right|_{X_F=0} = \frac{8\pi\alpha^2\sqrt{s}}{9m^4} \left[\frac{1}{9} \bar{u}(x) \right] \left[4u_V(x) + \frac{21}{4} \bar{u}(x) \right] + d_V(x)$$

where $x_1 \rightarrow x_2 \rightarrow \sqrt{\tau}$ as $X_F \rightarrow 0$ (see Eqs. I-2)

The $d\sigma/dm$ for $m > 4.5$ GeV has been extrapolated to $X_F=0$ as in Eq. IV-4 and associated discussion, and is displayed in Fig. IV-4 for both beam energies. The plotted curve is the Drell-Yan prediction resulting from Eqs. IV-8 and IV-7. We see that the Drell-Yan formula satisfactorily describes the general shape of the continuum (discounting the effects of T resonances between 8 and 12 GeV).

Our measured cross-sections are systematically higher than the Drell-Yan estimates. We define a factor K, such that:

$$\text{Eq. IV-9) } K \equiv \frac{\text{measured cross-section}}{\text{Drell-Yan prediction (using DIS. Structure fcn.)}}$$

By looking at Fig. IV-4 at 62 GeV, we see a K factor of 1.6 for $m < 8$ GeV, a higher K of ≈ 2.2 at $10 < m < 12$ GeV^{*}, and again a somewhat lower K for $m > 12$ GeV (determination limited by statistics). At 44 GeV, we also find a factor $K \approx 1.5$ for $m < 8$ GeV, and a lack of statistics prohibits a quantitative investigation beyond the T mass.

Lower energy experiments have found K factors ranging from 1.6 (Ref. 8) to 2.2 (Ref. 7), however suffer from normalization uncertainty introduced by nuclear targets. Theoretical arguments based on the perturbative effect of QCD contributions predict a (very approximate) factor of two⁹⁾, but depend heavily on the (presently unknown) effects of higher-order QCD processes.

The use of nucleon structure functions derived in lepton scattering experiments assume the probing of nucleons in space-like and time-like fashion to be equivalent. The structure functions quoted in Eq. IV-7 were derived at $Q^2 \approx -20 \text{ GeV}^2$. By using eq. IV-8 over the span

*) The 11% mass resolution causes $\approx 20\%$ T contamination in this interval due to the exponentially dropping cross-section.

$m^2 = |q^2| = 20 \rightarrow 400 \text{ GeV}^2$, we neglect scaling violations which are expected¹⁰⁾ to be under 15% and within the error allotted to eqs. IV-7 in Ref. 7.

IV-2) Dependence on X_F

Figures IV-5 and IV-6 present $d\sigma/dX_F$ in the stated mass intervals. The solid lines are fits of the form:

$$\text{Eq. IV-10)} \quad \frac{d\sigma}{dX_F} = A_x (1 - |X_F|)^\beta$$

The resulting A_x and β values are listed in Table IV-2. For the 62 GeV data, we notice a significantly steeper X_F behavior in the region $8 < m < 11 \text{ GeV}$ (50% contribution from T resonances) than in the two adjacent intervals. This also is seen to a lesser extent in the 44 GeV data, where we find a steeper X_F dependence (via the fits of eq. IV-10) in the region $m > 8 \text{ GeV}$. At 62 GeV, we notice the high-mass interval $m > 11 \text{ GeV}$ to have a broader X_F distribution than the lower mass $5 > m > 8 \text{ GeV}$ region, as indicated in lower energy experiments³⁾.

The dashed lines in Figs. IV-5 and IV-6 are Drell-Yan calculations scaled up by 1.6 (the K factor discussed earlier). We have used the structure functions of Eq. IV-7 in the Drell-Yan formula (eq. I-1) and numerically integrated over the mass ranges considered to yield the $d\sigma/dX_F$ curves. The shape of the predictions generally agree with the data (excluding T effects), and support the flatter distributions at higher mass.

IV-3) Dependence on $\cos\theta_{cs}$

Figure IV-7 shows $d\sigma/d|\cos\theta_{cs}|$ at $\sqrt{s} = 62 \text{ GeV}$ over the labeled mass intervals. The curves are fits of the form:

$$\text{Eq. IV-11)} \quad \frac{d\sigma}{d|\cos\theta_{cs}|} = A_c (1 + \eta \cos^2\theta_{cs})$$

The resulting values of A_c and η are listed in Table IV-3. At 62 GeV, we find polarizations of $\eta \approx 1$ in the intervals $m < 11 \text{ GeV}$, as expected from the Drell-Yan mechanism (see Sec. I). In the interval $m > 11 \text{ GeV}$,

a steeper polarization of $\eta > 1$ seems indicated, but the fit is statistically limited. We see a smaller value of η in the region $8 < m < 11$ GeV (50% contribution from T resonances) than in the surrounding continuum. We also fit successfully to the form of eq. IV-11 at $\sqrt{s} = 44$ GeV, however statistical fluctuation and lack of events at high $|\cos\theta_{cs}|$ rule out more precise statements.

The results of the IBM analysis are used here; precautions taken to avoid systematic error are outlined in Sec. III-6 (e). The CDC results are in agreement.

IV-4) Transverse Momentum

Figures IV-8 and IV-9 show the transverse momentum distributions $d\sigma/dp_t^2$ for different mass intervals (as labeled). Omitting the first bin(s) ($p_t < 0.5$ GeV) dominated by the effects of quark confinement,¹⁴⁾ we obtain good fits to a simple exponential:

$$\text{Eq. IV-12)} \quad \frac{d\sigma}{dp_t^2} = A \frac{e^{-\alpha p_t}}{p}$$

as drawn on the figure. The fit results are summarized in Table IV-4, where we quote $2/\alpha \approx \langle p_t \rangle$. The average transverse momentum has also been calculated over these mass ranges in more detail by summing all events with $p_t < 4$ GeV and correcting each for acceptance. The resulting average is adjusted for background subtraction, and contributions from tail events at $p_t > 4$ GeV are calculated by integrating the fitted exponential. The $\langle p_t \rangle$ values resulting from this method (averaged between both analyses) are also listed in Table IV-4 and are plotted versus mass (together with lower energy data) in Fig. IV-10.

A comparison of our data with results of previous experiments supports the increase of $\langle p_t \rangle$ with CM energy. The increase of $\langle p_t \rangle$ with mass is also evident; $\langle p_t \rangle$ reaches 1.9 GeV ($\sqrt{s} = 62$ GeV) and 1.5 GeV ($\sqrt{s} = 44$ GeV) at the higher mass intervals. This can not be explained within the framework of Drell-Yan annihilation, where the p_t from quark confinement reaches only ≈ 300 MeV¹¹⁾ and is independent of beam energy.

The curves drawn on Fig. IV-10 are QCD predictions from Ref. 12, in which estimated contributions from the "Compton process" (see Fig. I-2) are included in determining the $\langle p_t \rangle$ of the lepton pair.

The high-mass ISR data overlaps in τ with the lower-energy Fermilab data at $\sqrt{\tau} = 0.2$. We have plotted $\langle p_t \rangle$ at fixed $\sqrt{\tau} = 0.2$ as a function of \sqrt{s} in Figure IV-11. The data indicates a linear increase in $\langle p_t \rangle$ with \sqrt{s} , as predicted at fixed τ by QCD calculations.¹²⁾

Figure IV-12 shows the results of QCD calculations¹³⁾ describing the shape of the p_t distribution for $5 < m < 8$ GeV at $\sqrt{s} = 62$ GeV. The dotted line is a gaussian of $\sigma = 680$ MeV representing the effects of primordial quark motion (measured to be $\sigma_q \approx 300$ MeV per quark at e^+e^- colliders, see Ref. 11) and low p_t pairs produced from multiple gluon emission in higher-order QCD processes.¹⁴⁾ As seen in the figure, these effects alone do not describe the shape of the observed p_t spectrum, particularly the tail of the distribution at $p_t > 2$ GeV. Contributions from the two first-order perturbative QCD corrections (Compton and Annihilation processes; see Fig. I-2) are separately sketched on Fig. IV-12. The annihilation process dominates at $p_t < 1$ GeV, but the Compton process supercedes this correction at higher p_t and accounts for the observed tail. Both of these terms diverge as $p_t \rightarrow 0$, where effects of confinement momentum dominate and the perturbative approach loses validity. To account for the confinement effects, the author of Ref. 12 has convoluted the first-order QCD corrections with the primordial gaussian (widened by the effect of higher-order QCD), obtaining the solid curve* drawn on Fig. IV-12. We see that the form of this curve agrees well with our data over the range of p_t observed.

IV-5) Fits to the Sea Quark Distribution

Using the Drell-Yan formula at $X_F=0$ (eq. IV-8) and the valence quark distributions originating from the neutrino scattering data as quoted in eq. IV-7, I have performed fits to the sea quark distributions using the form of Ref. 7:

$$\begin{aligned} \bar{u}(x) &= \bar{d}(x) = A_S (1-x)^b \\ \text{Eq. IV-13)} \quad s(x) &= \bar{s}(x) = \frac{1}{4} [\bar{u}(x) + \bar{d}(x)] \end{aligned}$$

The data was extrapolated to $X_F=0$ by Eq. IV-4, using the measured β values (Table IV-1). The errors associated with the corresponding X_F

*) The curve was not produced in absolute units and has been normalized to the data.

fits were propagated into the data points. To avoid resonance contamination, we use only points with $5 < m < 8$ GeV and $m > 12.5$ GeV.

At $\sqrt{s} = 62$ GeV, we find $A_s = 0.42 \pm .05$ and $b = 8.3 \pm 1.0$ with a $\chi^2/DF = 6/17$. Using this fitted sea parameterization in the Drell-Yan formula (eq. IV-8), we see good agreement with the data in Fig. IV-13. Fits at $\sqrt{s} = 44$ GeV confirm this result, but their significance is limited by the lower statistics. The value of b stated above agrees with the sea exponent of 8.1 obtained from the deep-inelastic scattering data (eqs. IV-7).

The K factor (see eq. IV-9) is implicit in the fitted value of A_s . Ignoring the relatively small contribution from double sea quark annihilation in eq. IV-8 and taking $K=1.6$, we find $A_o = A_s/1.6 = 0.26 \pm .03$, in good accordance with the sea normalization of 0.27 as obtained from the DIS. data (eq. IV-7).

Basing arguments upon the differing content of up and down quarks in the proton and the effects of the Pauli principle, Feynman and Field have proposed¹⁵⁾ that the up and down distributions in the proton sea are not identical. We take the form:

$$\begin{aligned} \bar{u}(x) &= A_s (1-x)^{b_u} \\ \bar{d}(x) &= A_s (1-x)^{b_d} \\ \text{and } s(x) = \bar{s}(x) &= \frac{1}{4}[\bar{u}(x) + \bar{d}(x)] \end{aligned}$$

Eq. IV-14)

Using this parameterization with the valence distributions of eq. IV-7, we have fit our 62 GeV data to A_s , b_u , and b_d . Our fit has yielded $A_s = 0.43 \pm .08$, $b_u = 9.1 \pm 3.3$, and $b_d = 5.5 \pm 4.6$ with $\chi^2/DF = 6/16$. These values show steeper behavior of the up sea as indicated by similar fits to Fermilab data by the CFS collaboration,¹⁶⁾ which gave (without q^2 correction) $b_u = 11.10 \pm .26$ and $b_d = 7.62 \pm .08$.

*)The small errors allotted to the CFS fit results indicate that they do not include systematic uncertainty, and are statistically derived from the χ^2 behavior of the fit.

SECTION IV - REFERENCES

- 1) K. Kinoshita et. al., Phys. Rev. D 17, 1834 (1977).
- 2) K. Ueno et. al., Phys. Rev. Lett. 42, 486 (1979).
- 3) K.J. Anderson et. al., Phys. Rev. Lett. 42, 944 (1979).
- 4) D.M. Kaplan et. al., Phys. Rev. Lett. 40, 435 (1978).
- 5) J.K. Yoh et. al., Phys. Rev. Lett. 41, 684 (1978).
- 6) J.G.H. De Groot et. al., Z. Phys. C1, 143 (1979).
R. Turlay, Proc. of the EPS Int. Conf. on High Energy Phys., Vol. 1, 50 (1979).
- 7) J. Badier et. al., Phys. Lett. 89B, 145 (1979).
- 8) L. Lederman, Proc. of the Int. Lepton-Photon Symposium, FNAL, 575 (1979).
- 9) G. Altarelli et. al., Nucl. Phys. B 143, 521 and 146 544 (1978) and 157, 461 (1979).
J. Kubar et. al., Nucl. Phys. B 175, 251 (1980).
- 10) R. Horgan, private communication.
- 11) The MARK-J Collaboration, Phys. Reports 63, 337-391 (1980).
R. Brandelik et. al., DESY Preprint 80/40 (1980).
- 12) H. Fritzsch and P. Minkowski, Phys. Lett. 73B, 80 (1978)
- 13) R.D. Field, "Applications of Quantum Chromodynamics", Cal. Tech. preprint CALT-68-696 (1978) and "Perturbative Quantum Chromodynamics and Applications to Large Momentum Transfer Processes", Cal Tech. preprint CALT-68-739 (1979).
I thank Dr. Field for helpful discussions and calculations.
- 14) G. Parisi and R. Petronzio, Nucl. Phys. B 154, 427 (1979).
- 15) R.P. Feynman and R.D. Field, Phys. Rev. D 15, 2590 (1977).
- 16) A.S. Ito et. al., "Measurements of the Continuum of Dimuons Produced in High-energy Proton-Nucleus Collisions", FERMILAB-PUB-80/19-EXP (1980).
- 17) A.L.S. Angelis et. al., Phys. Lett. 87B, 398 (1979).
- 18) C. Kourkoumelis et. al., Phys. Lett. 91B, 481 (1980).
- 19) L. Lederman, Proc. of the 19'th Int. Conf. on High Energy Phys., Tokyo, 706, (1978).

- 20) J. Badier et. al., Proc. of the Int. Lepton-Photon Symposium, FNAL, 161 (1979).
- 21) F.W. Busser et. al., Phys. Lett. 56B, 482 (1975).
- 22) H.D. Snyder et. al., Phys. Rev. Lett. 36, 1415 (1976).
- 23) K.J. Anderson et. al., Phys. Rev. Lett. 36, 237 (1976).
J.G. Branson et. al., Phys. Rev. Lett. 38, 1331 (1977).
- 24) Yu. M. Antipov et. al., Phys. Lett. 60B, 309 (1976).
- 25) U. Becker, Phys. Rev. Lett. 38, 140 (1977).
- 26) J.G. Branson et. al., Phys. Rev. Lett. 38, 1334 (1977).

TABLE IV-1 MEASURED CROSS-SECTION VS. MASS

Mass Range (GeV)	$d\sigma/dm$ $\sqrt{s} = 62$ GeV ($\times 10^{-36}$ cm ² /GeV)	$d\sigma/dm$ $\sqrt{s} = 44$ GeV ($\times 10^{-36}$ cm ² /GeV)
2.2 - 2.3	10800 ± 4700	6000 ± 5800
2.3 - 2.4	10200 ± 3000	6000 ± 3000
2.4 - 2.5	15000 ± 2400	7100 ± 2100
2.5 - 2.6	20400 ± 2800	8800 ± 1400
2.6 - 2.7	31400 ± 3700	13100 ± 2100
2.7 - 2.8	38200 ± 3500	16000 ± 2400
2.8 - 2.9	47800 ± 2400	18500 ± 2800
2.9 - 3.0	50200 ± 2400	20600 ± 3000
3.0 - 3.1	45200 ± 2400	22500 ± 3300
3.1 - 3.2	40500 ± 2300	22400 ± 3300
3.2 - 3.3	38000 ± 2200	15500 ± 2600
3.3 - 3.4	30800 ± 2100	13900 ± 2500
3.4 - 3.5	23300 ± 1900	10000 ± 2100
3.5 - 3.6	19900 ± 1800	10000 ± 2100
3.6 - 3.7	12800 ± 1600	2600 ± 1330
3.7 - 3.8	12000 ± 1500	-----
3.8 - 3.9	7900 ± 1500	-----
3.9 - 4.0	4000 ± 1300	-----
4.0 - 4.5	822 ± 64	345 ± 57
4.5 - 5.0	335 ± 28	206 ± 28
5.0 - 5.5	195 ± 15	105 ± 40
5.5 - 6.0	120 ± 9	57.6 ± 8.5
6.0 - 6.5	76.9 ± 6.0	26.6 ± 5.0
6.5 - 7.0	52.6 ± 4.5	20.2 ± 3.9
7.0 - 7.5	36.8 ± 3.4	17.4 ± 3.3
7.5 - 8.0	25.7 ± 2.7	12.4 ± 2.7
8.0 - 8.5	22.4 ± 2.2	7.7 ± 1.9
8.5 - 9.0	17.5 ± 1.8	3.5 ± 1.3
9.0 - 9.5	18.4 ± 1.9	4.3 ± 1.3
9.5 - 10.0	13.5 ± 1.7	3.7 ± 1.2
10.0 - 10.5	7.73 ± 1.19	4.5 ± 1.4
10.5 - 11.0	6.89 ± 1.13	1.44 ± .75
11.0 - 11.5	4.84 ± .93	1.75 ± .80
11.5 - 12.0	3.78 ± .80	0.66 ± .32
12.0 - 12.5	2.67 ± .66	0.33 ± .42
12.5 - 13.0	2.23 ± .59	-----
13.0 - 13.5	1.28 ± .45	-----
13.5 - 14.0	0.75 ± .33	-----
14.0 - 14.5	1.25 ± .44	0.29 ± .32
14.5 - 15.0	0.60 ± .29	0.31 ± .33
15.0 - 15.5	0.36 ± .22	0.32 ± .33
15.5 - 16.0	0.36 ± .21	-----
16.0 - 16.5	0.60 ± .31	-----
16.5 - 17.0	0.12 ± .12	0.32 ± .36
17.0 - 17.5	0.24 ± .18	-----
17.5 - 18.0	0.24 ± .20	-----
18.0 - 18.5	0.12 ± .13	-----
18.5 - 19.0	-----	-----
19.0 - 19.5	-----	-----
19.5 - 20.0	-----	-----
20.0 - 20.5	-----	-----
20.5 - 21.0	-----	-----
21.0 - 21.5	-----	-----
21.5 - 22.0	-----	-----
22.0 - 22.5	0.12 ± .15	-----
22.5 - 23.0	-----	-----
23.0 - 23.5	-----	-----
23.5 - 24.0	0.12 ± .18	-----
24.0 - 24.5	0.12 ± .24	-----
24.5 - 25.0	-----	-----

TABLE IV-2 FITS TO X_F DISTRIBUTIONS

$$d\sigma/dx_F = \frac{A_x}{x}(1 - |x_F|)^\beta$$

\sqrt{s} (GeV)	Mass Range (GeV)	A_x ($\times 10^{-35} \text{ cm}^2$)	β	χ^2/DF
	5 \rightarrow 8	43.5 \pm .3	2.71 \pm .24	9.9/15
62	8 \rightarrow 11	8.5 \pm .8	3.26 \pm .33	11.7/14
	11 \rightarrow 25	1.5 \pm .3	2.09 \pm .27	5.1/9
44	5 \rightarrow 8	16.3 \pm .3	2.09 \pm .39	2.0/7
	8 \rightarrow 17	2.4 \pm .5	2.57 \pm .32	3.3/8

TABLE IV-3 FITS TO $\cos\theta_{CS}$ DISTRIBUTIONS

$$d\sigma/d\cos\theta_{CS} = A_c(1 + \eta \cdot \cos^2\theta_{CS})$$

\sqrt{s} (GeV)	Mass Range (GeV)	A_c ($\times 10^{-36} \text{ cm}^2$)	η	χ^2/DF
62	6 → 8	67.2 ± 4.5	1.24 ± .56	11.7/15
	8 → 11	29.2 ± 2.3	0.82 ± .55	11.3/6
	11 → 25	5.9 ± 1.1	3.38 ± 1.94	3.2/5
44	5 → 8	70 ± 8	1.95 ± 1.09	9.3/6
	8 → 17	8.8 ± 1.6	3.02 ± 1.79	4.0/6

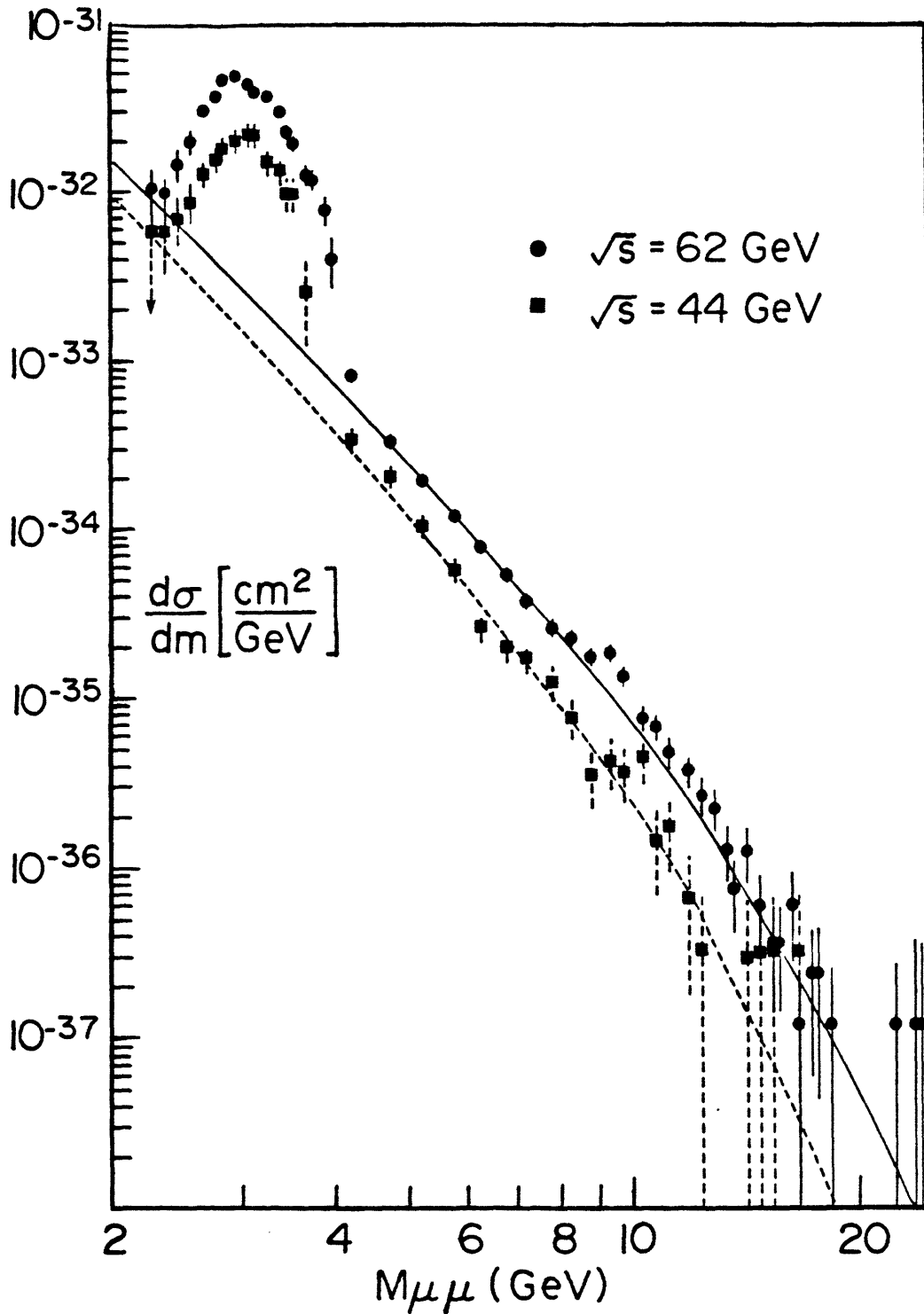
TABLE IV-4

Fits to $A_p e^{-\alpha \cdot p_T}$, and average transverse momenta.

The errors include estimates of systematic uncertainties.

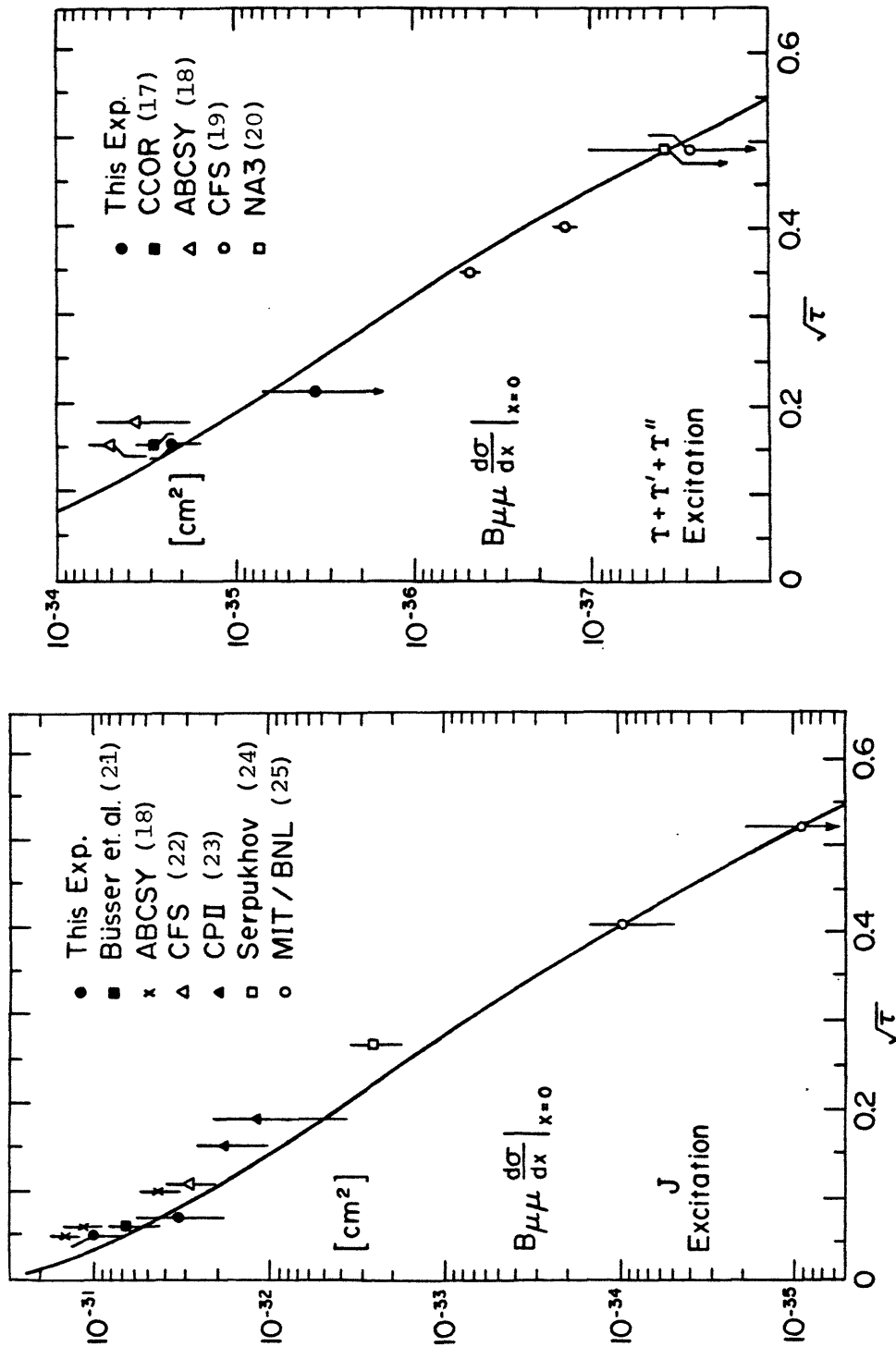
\sqrt{s}	Mass Range (GeV)	A_p 10^{-35} (cm ² /GeV ²)	FIT		
			χ^2/DF	$\frac{2}{\alpha} \approx \langle p_T \rangle$ (GeV)	$\langle p_T \rangle$ from events (GeV)
62 GeV	2 → 4	3300 ± 1000	7.9/10	1.4 ± 0.2	1.40 ± 0.20
	5 → 8	22. ± 2.	8.2/10	1.5 ± 0.1	1.60 ± 0.10
	8 → 11	2.3 ± 0.3	2.9/10	1.9 ± 0.2	2.05 ± 0.15
	11 → 25	0.54 ± 0.23	6.5/7	1.9 ± 0.4	1.95 ± 0.25
44 GeV	2 → 4	2500 ± 1000	5.1/8	1.1 ± 0.2	1.10 ± 0.20
	5 → 8	9.3 ± 2.3	4.3/7	1.5 ± 0.2	1.50 ± 0.15
	8 → 17	0.9 ± 0.4	0.9/7	1.9 ± 0.4	1.50 ± 0.15

FIGURE IV-1



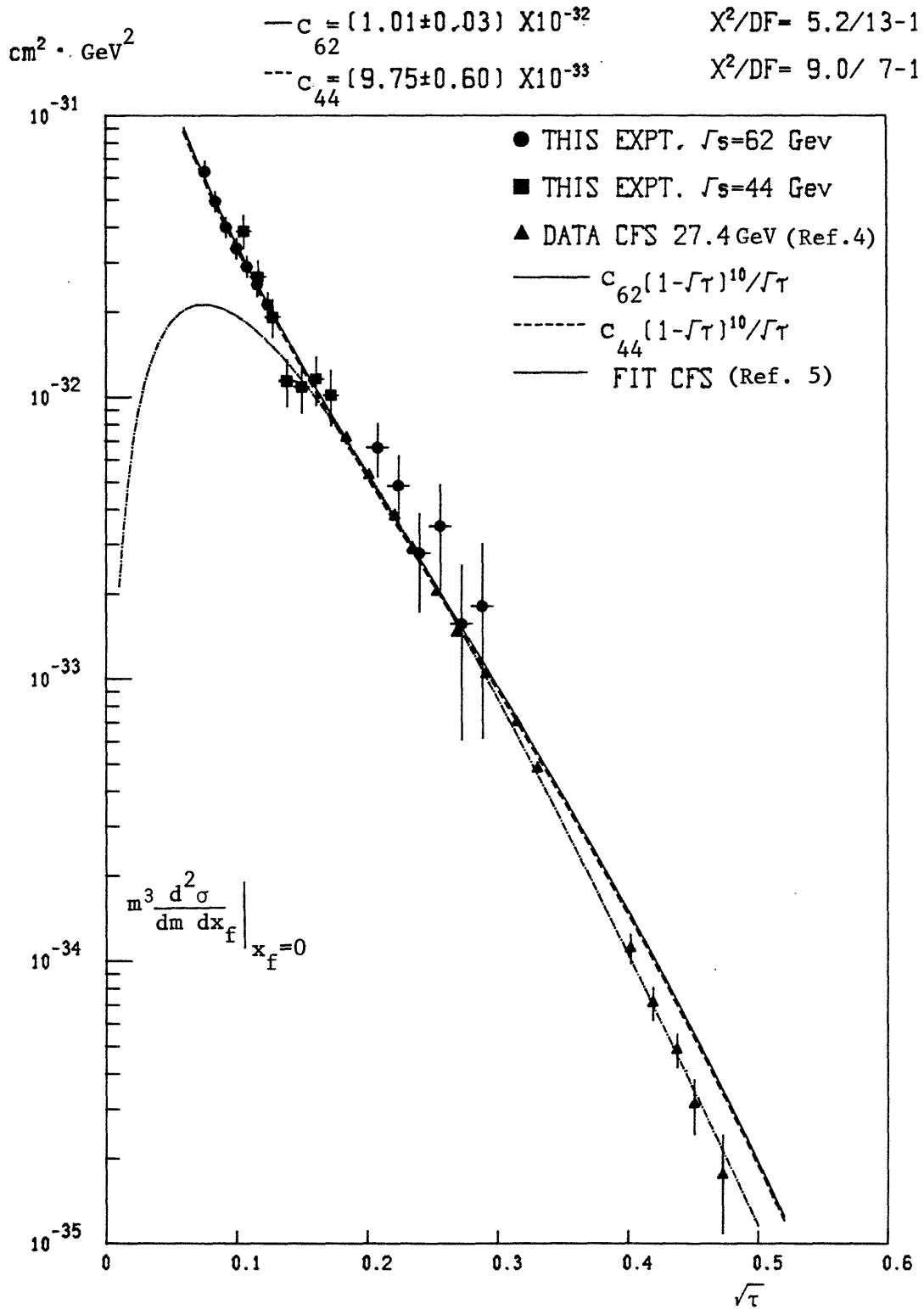
Measured cross-section as a function of mass.
The curves are continuum fits, listed in Sec. IV-1.

FIGURE IV-2 J AND T EXCITATION



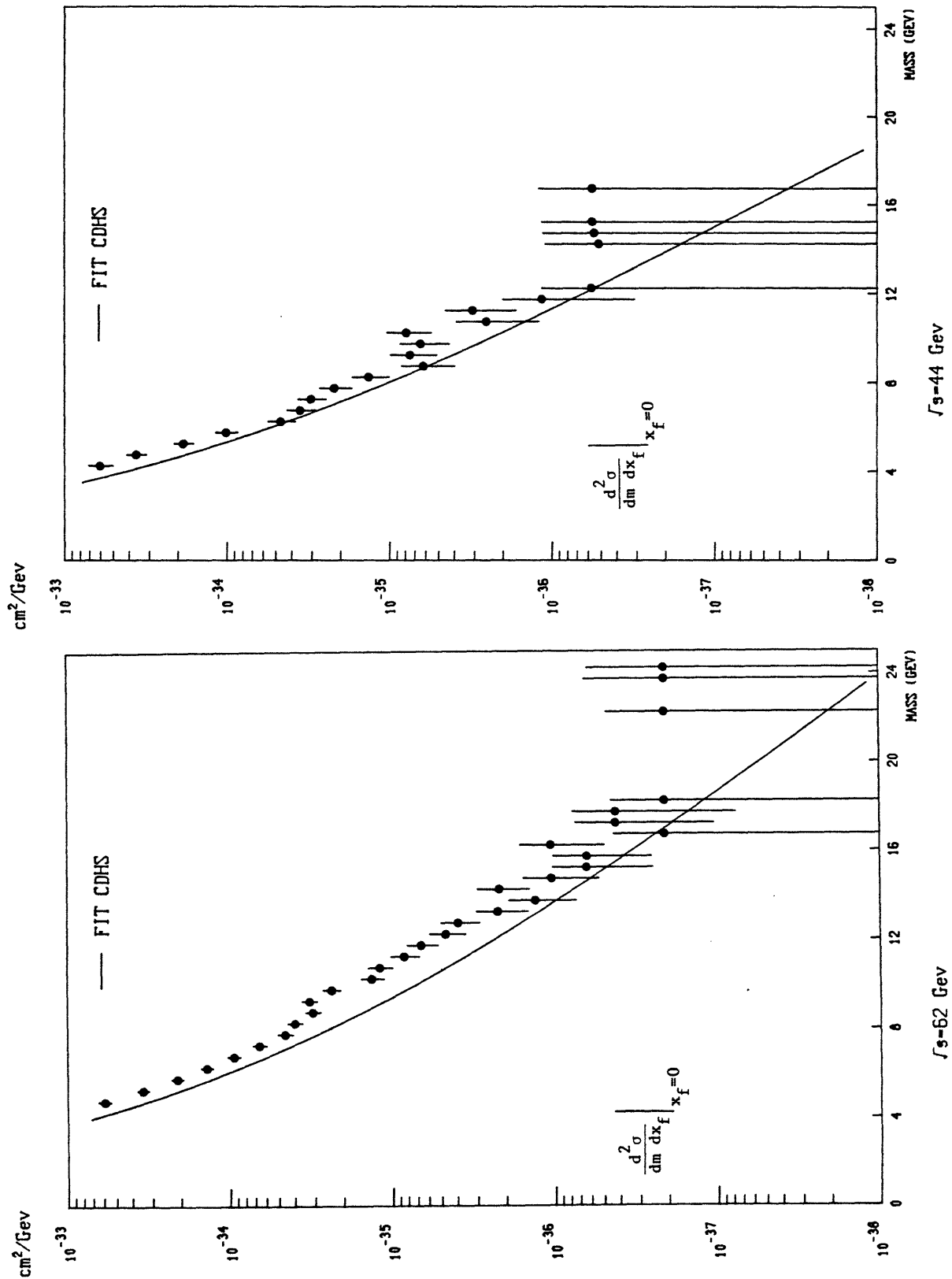
The curves are the continuum fit of Fig. IV-3, arbitrarily normalized to the data points. It can be seen that the J and T cross-sections scale with \sqrt{T} in a similar fashion to the continuum. References to previous experiments are enclosed in parentheses.

FIGURE IV-3



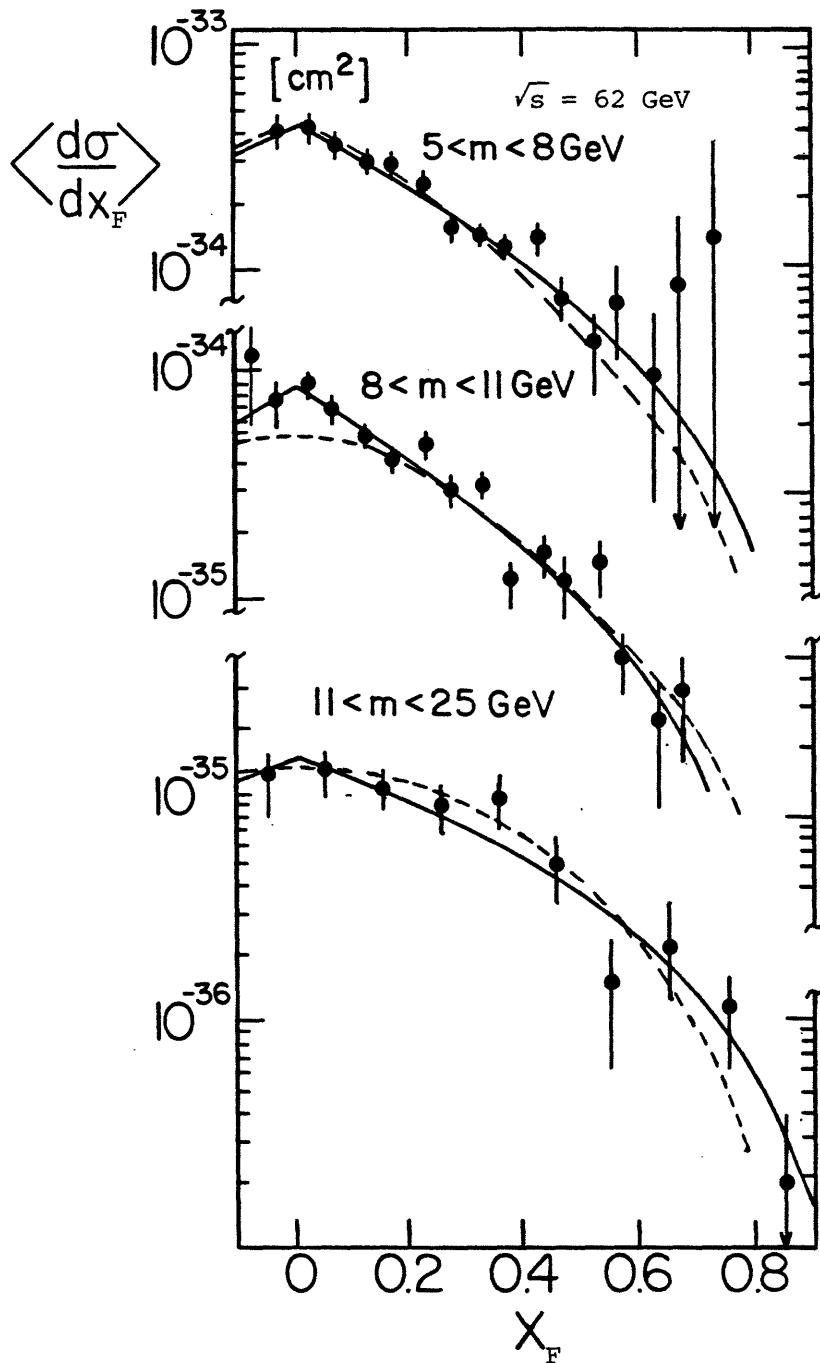
The scaling function $F(\tau)$. See Sec. IV-1 (c).

FIGURE IV-4



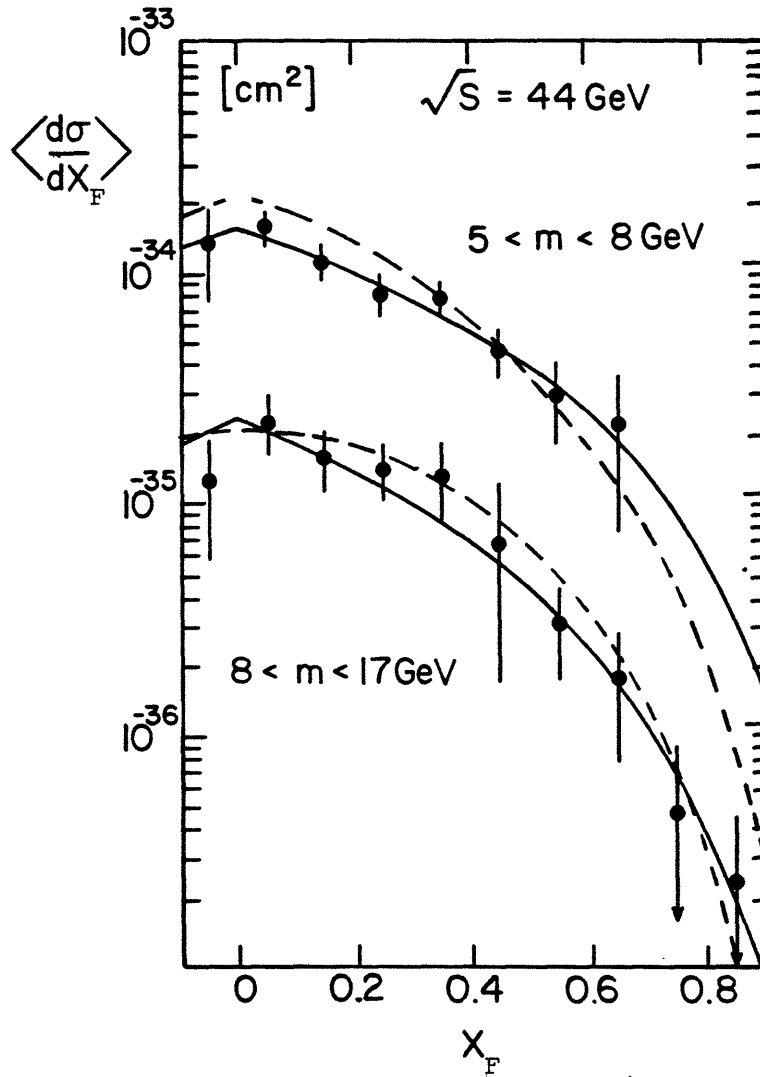
Comparison of measured cross-sections with Drell-Yan predictions.
 A factor of 1.6 is needed for agreement. See Sec. IV-1 (d).

FIGURE IV-5



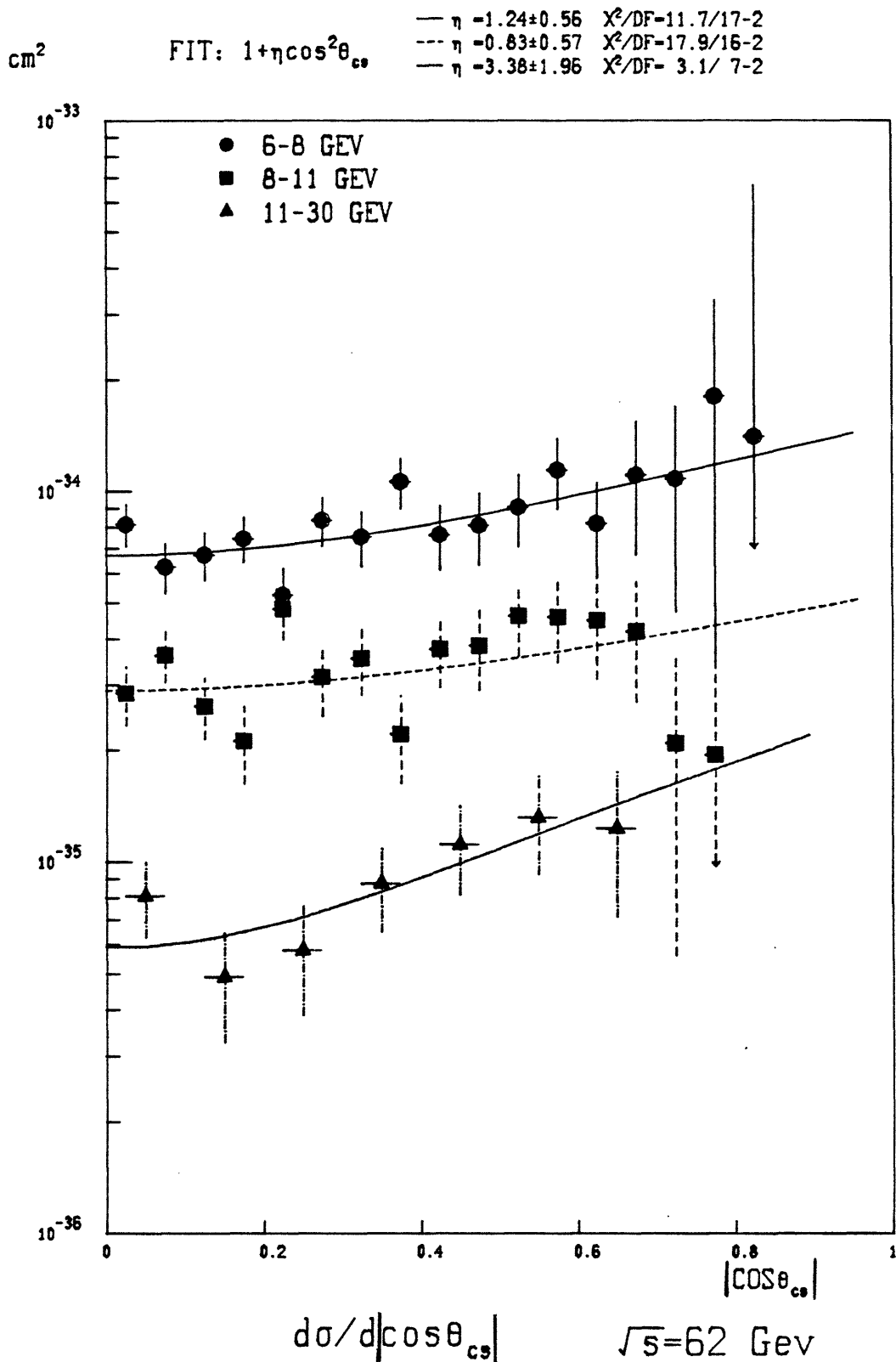
Measured cross-section in X_F at $\sqrt{s} = 62 \text{ GeV}$. The solid lines are fits to the data listed in Table IV-2. The dashed lines are Drell-Yan predictions, scaled up by a factor of 1.6.

FIGURE IV-6



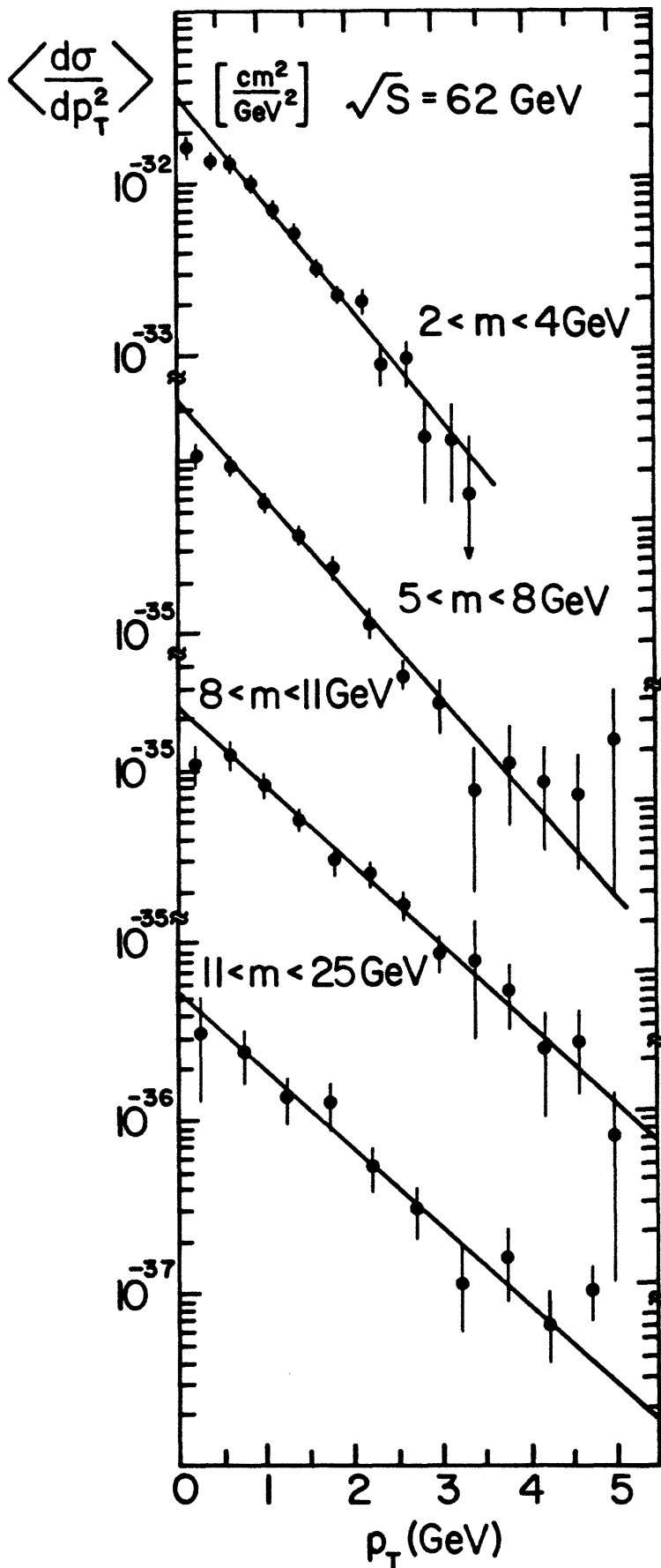
Measured cross-section in X_F at $\sqrt{s} = 44 \text{ GeV}$. The solid lines are fits to the data listed in Table IV-2. The dashed lines are Drell-Yan predictions, scaled up by a factor of 1.6.

FIGURE IV-7



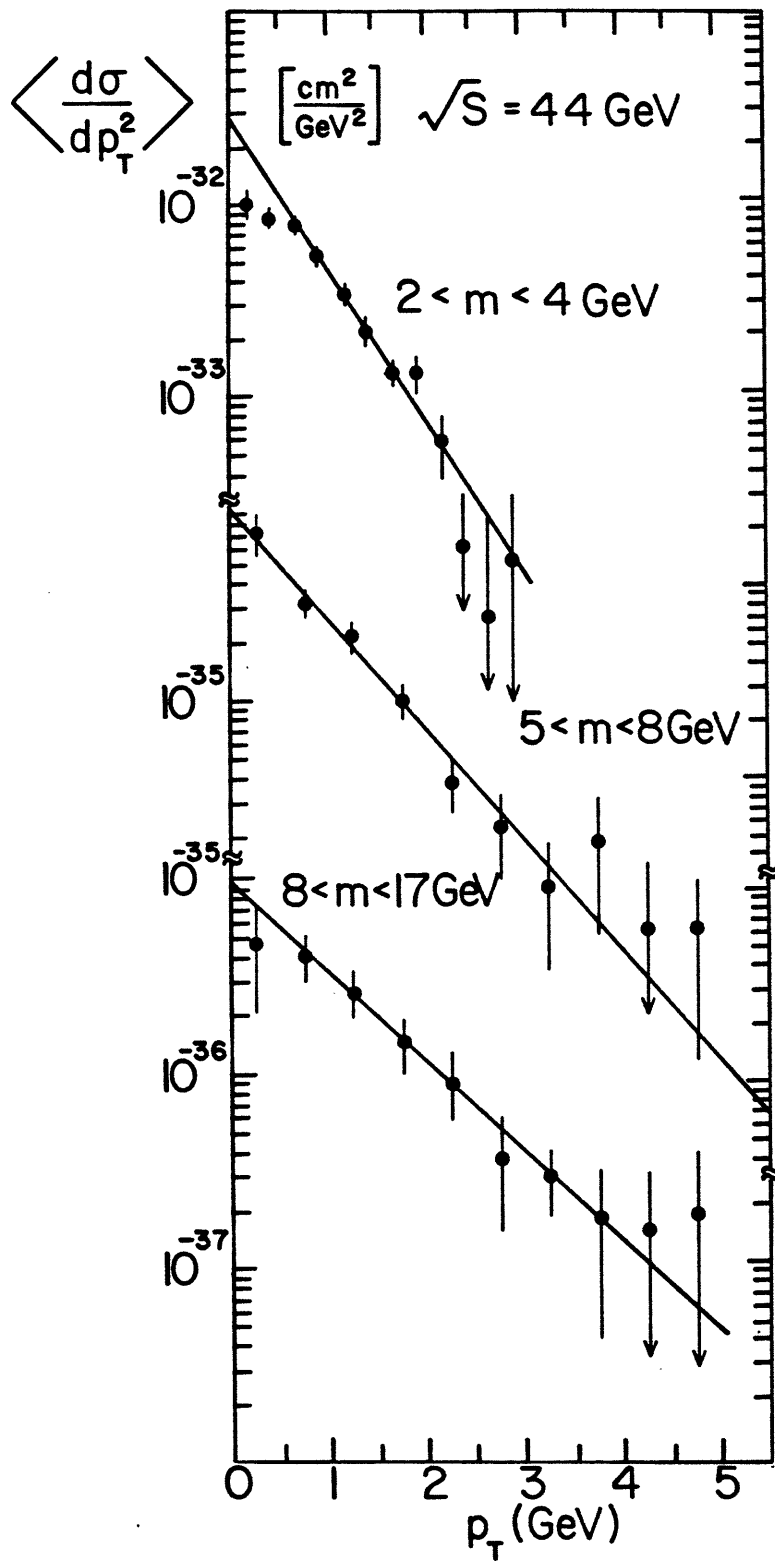
Angular distributions of dimuons relative to the Collins-Soper axis (see App. I). The curves are fits to the data (Table IV-3).

FIGURE IV-8



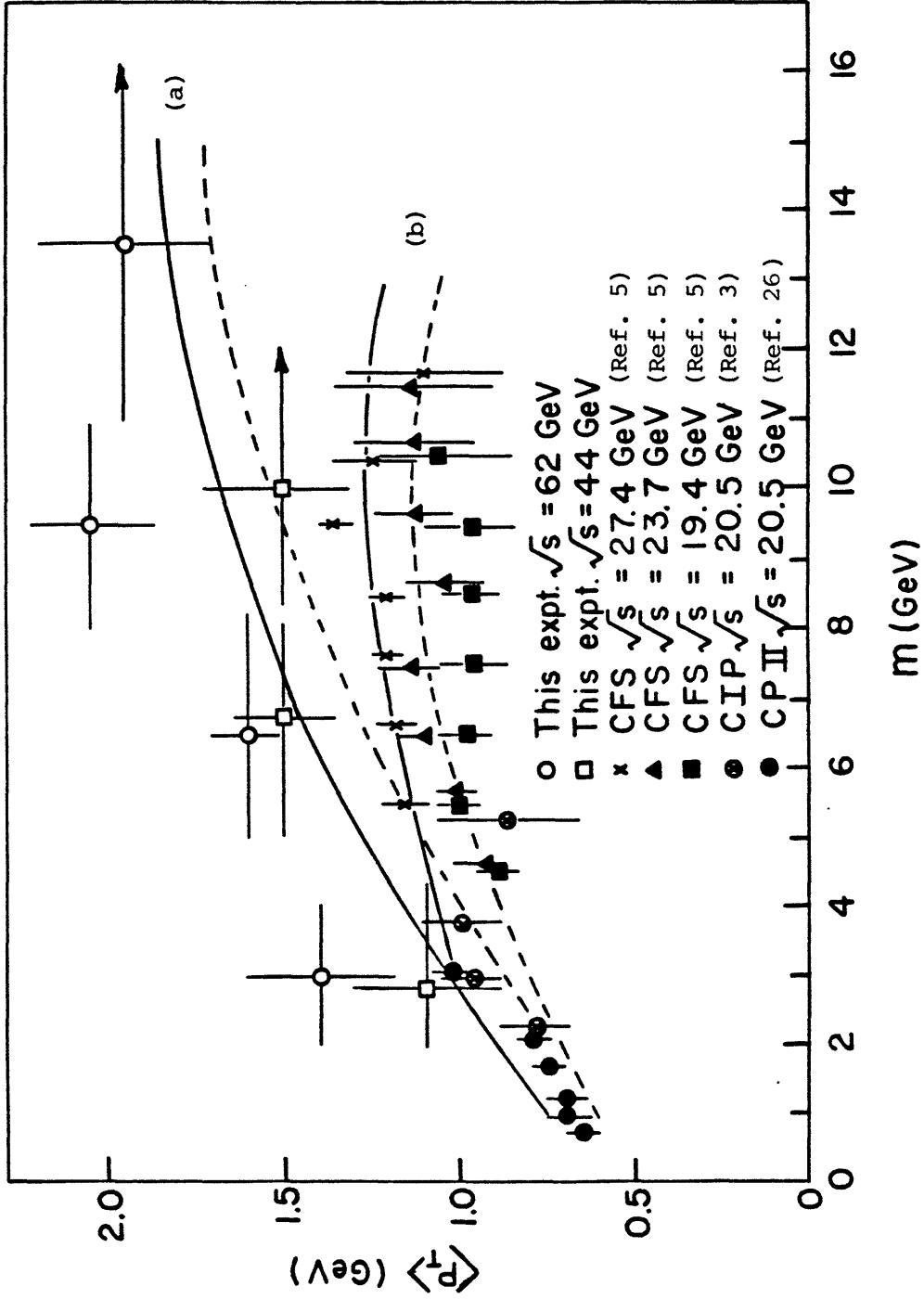
Transverse momentum distributions at $\sqrt{s} = 62$ GeV. The lines are fits to a simple exponential (omitting bins with $p_T < 0.5$ GeV); See Table IV-4.

FIGURE IV-9



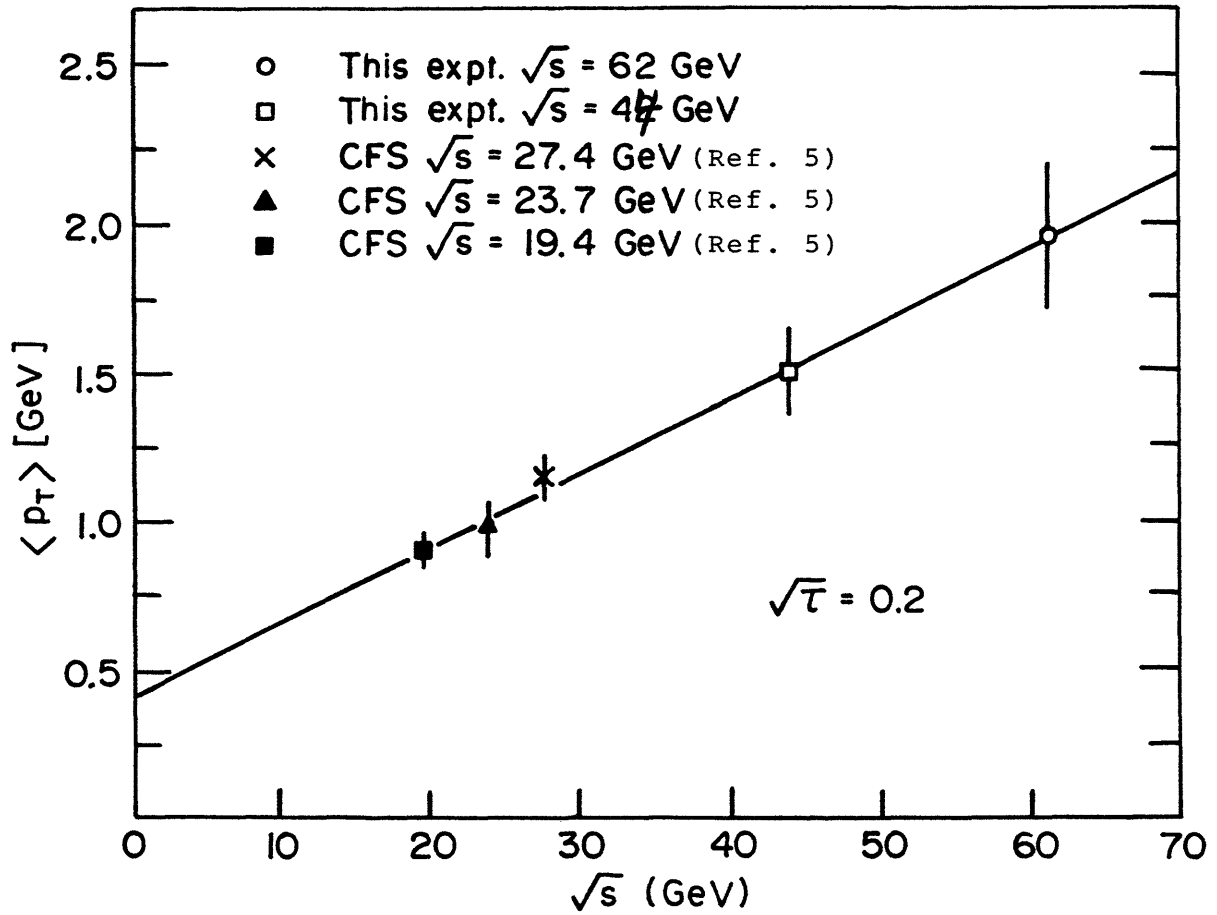
Transverse momentum distributions at $\sqrt{s} = 44 \text{ GeV}$. The lines are fits to a simple exponential (omitting bins with $p_t < 0.5 \text{ GeV}$); See Table IV-4.

FIGURE IV-10



Average transverse momentum as a function of pair mass. The ISR and the lower energy results are compared with QCD predictions for $\sqrt{s} = 58$ GeV (a), and $\sqrt{s} = 27.4$ GeV (b) respectively. In each case, two hypotheses of quark momentum spread have been made; 500 MeV (solid line) and 300 MeV (dotted line).

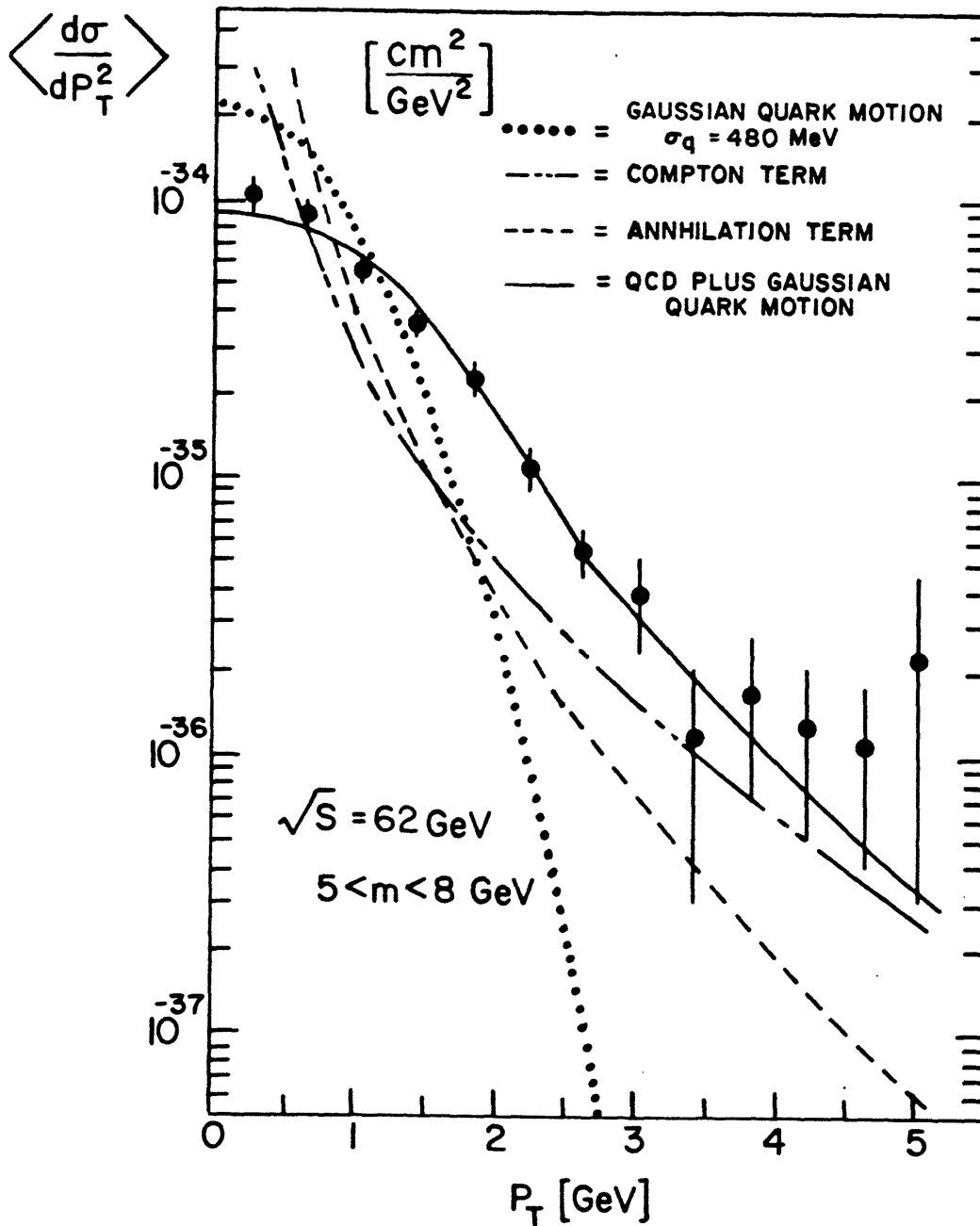
FIGURE IV-11



Average transverse momentum vs. \sqrt{s} at a common $\sqrt{\tau} = 0.2$.

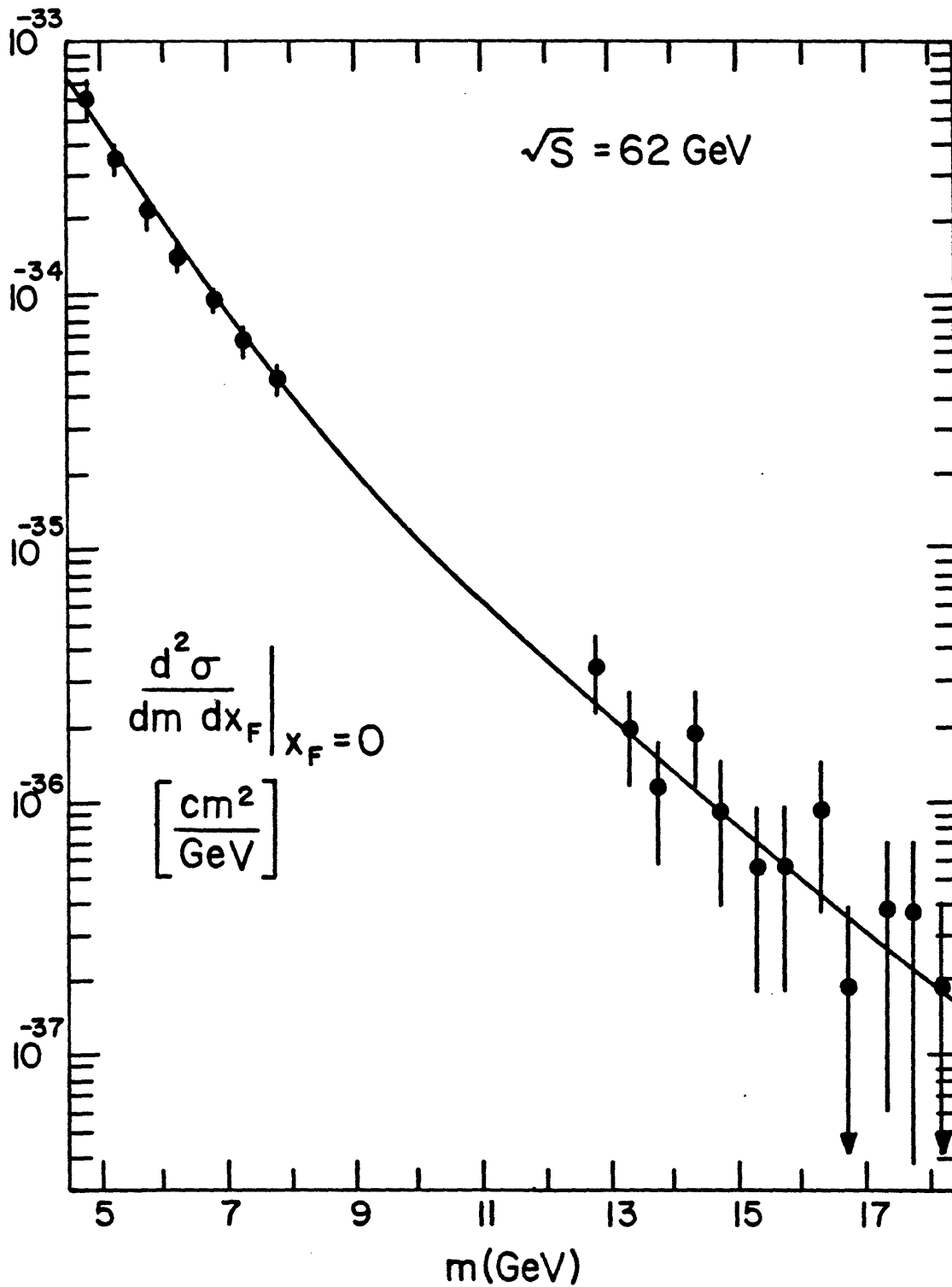
A linear increase of $\langle p_t \rangle$ with \sqrt{s} at fixed τ is predicted by QCD calculations. The line sketched above was visually fit to the data points.

FIGURE IV-12



Transverse momentum distribution for $5 < m < 8$ GeV, $\sqrt{s} = 62$ GeV. Results of QCD calculations from ref. 13 are overlaid. The first order processes in α_s are dashed lines. The dotted curve is a gaussian of $\sigma=680$ MeV, representing non-perturbative effects of quark confinement, and higher-order QCD processes producing low- p_T pairs. The QCD terms are convoluted with the gaussian to yield the solid curve.

FIGURE IV-13



Plot of the data vs. Drell-Yan prediction using the fitted sea function from Sec. IV-5.

CONCLUSIONS

We have seen that the shape of the mass spectra and X_F distributions presented in this thesis agree well with the predictions of the Drell-Yan model. The measured cross-sections are a factor of 1.6 above Drell-Yan estimates, which is in agreement with QCD normalization corrections within the accuracy of present calculations.

The addition of first-order QCD gluon processes to Drell-Yan annihilation can describe the high average transverse momenta (up to 2 GeV) observed in this experiment, as well as the increase of $\langle p_t \rangle$ with mass and \sqrt{s} . The shape of our measured p_t distributions agrees with first-order QCD predictions for $p_t > 1$ GeV; at smaller p_t , non-perturbative effects must be introduced for an adequate description.

We find no indications of scaling violation within the significance of experimental errors in a comparison between our measurements at 62 and 44 GeV and lower energy data.

The sea-quark distribution extracted by fitting our measured cross-section to the Drell-Yan formula agrees with that derived from neutrino scattering data (see Refs. 6 and 7 of Sec. IV) after accounting for the factor 1.6 normalization correction, indicating the equivalence between weak and electromagnetic probing of proton structure.

The measured J and T cross-sections, together with lower energy data, scale with $\sqrt{\tau}$ in a similar fashion to the continuum. The T region appears to have a steeper X_F dependence and flatter polarization than the surrounding continuum. No evidence is found for new vector mesons beyond the T mass, and we set an upper limit of $B_{\mu\mu} \sigma_x < 40 \cdot 10^{-38} \text{ cm}^2$ on new heavy resonances with mass over 20 GeV, which possess decay channels into muon pairs.

APPENDIX I DEFINITIONS

We describe the final state of the dimuons in terms of the quantities m , X_F , P_t , and $\cos\theta_{cs}$. These are defined below:

$$m \equiv \text{invariant mass of muon pair} = |P_{\mu 1} + P_{\mu 2}| = [2m_{\mu}^2 + E_1 E_2 - \vec{p}_1 \cdot \vec{p}_2]^{1/2}$$

$$P_{\mu 1}, P_{\mu 2} = 4\text{-momenta of muons}$$

$$\vec{p}_1, \vec{p}_2 = 3\text{-momenta of muons}$$

$$m_{\mu} = \text{muon rest mass}$$

$$E_1, E_2 = \text{Energy of muons}$$

$$X_F \equiv \text{Feynman scaling variable} = p_{11}/p_{(\max)} = \frac{2\sqrt{s} (\vec{p}_1 + \vec{p}_2)_{11}}{\sqrt{\Delta(m^2, 4m_p^2, s)}}$$

$$\Delta(A, B, C) \equiv A^2 + B^2 + C^2 - 2AB - 2AC - 2BC$$

$$m_p = \text{proton rest mass}$$

$$\sqrt{s} = \text{total CM energy of proton-proton system}$$

$$p_{11} = \text{longitudinal momentum of dimuon in CM frame.}$$

$$p_{(\max)} = \text{Maximum kinematically allowable momentum of dimuon in CM frame.}$$

Occasionally the rapidity (y) of the dimuon is used in place of X_F :

$$y \equiv \frac{1}{2} \ln\left(\frac{E + p_{11}}{E - p_{11}}\right) \quad \text{and the fractional momenta become: } \begin{array}{l} x_1 = \sqrt{\tau} e^y \\ x_2 = \sqrt{\tau} e^{-y} \end{array}$$

(see Sec. I)

$$P_t \equiv \text{Transverse momentum of dimuons in CM frame} = p_{t(1)} + p_{t(2)}$$

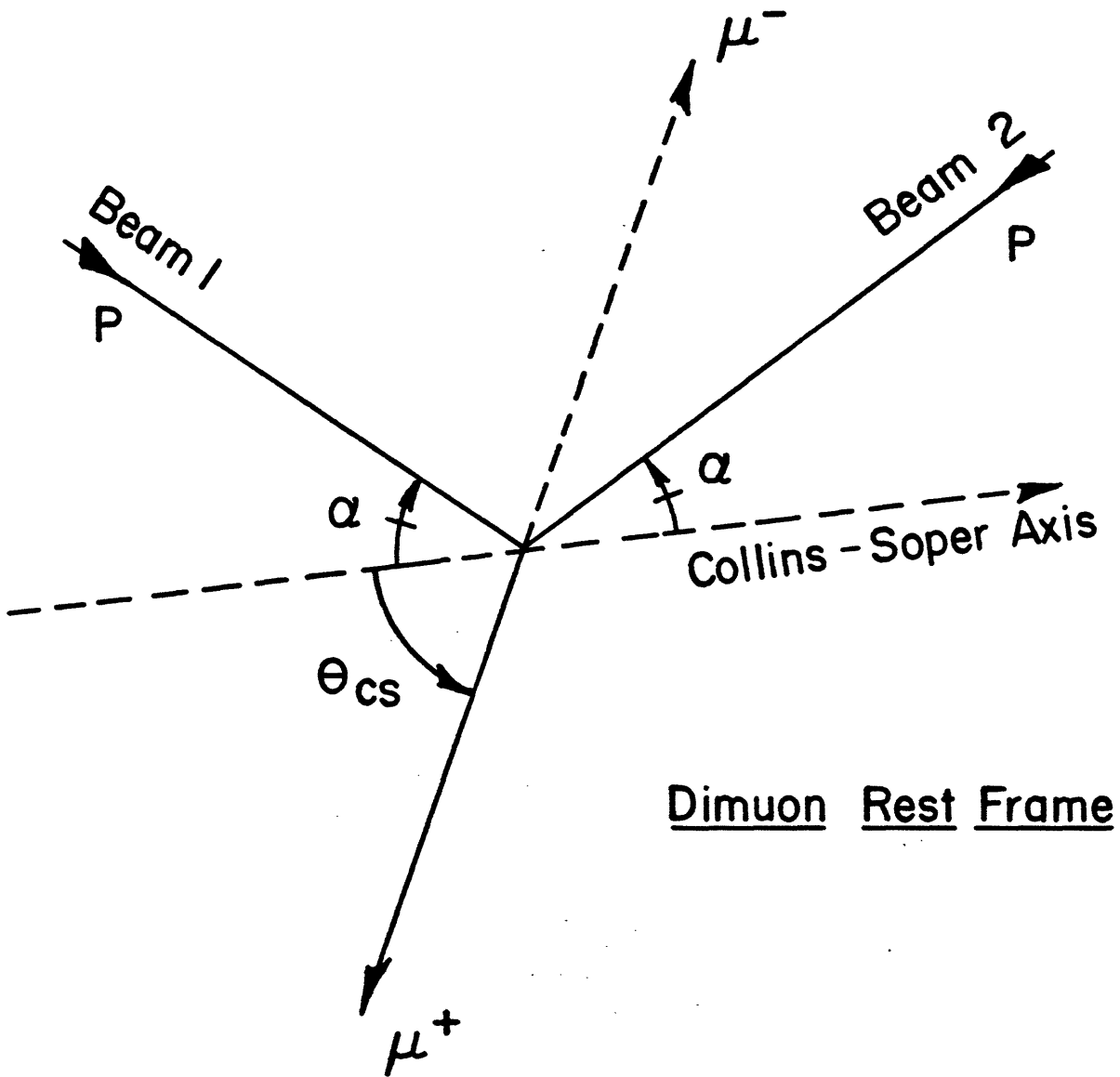
$\cos\theta_{cs} \equiv$ Cosine of helicity angle relative to the Collins-Soper axis.

The Collins-Soper¹⁾ axis is defined to bisect the angle between beam 1 and the reversed beam 2 (See Fig. AI-1), as seen in the dimuon rest frame. θ_{cs} and ϕ_{cs} are conventionally defined relative to the direction of the μ^+ .

REFERENCES

- 1) J.C. Collins and D.E. Soper, Phys. Rev. D 17, 1834 (1977).

Figure AI-1
Definition of θ_{CS}



APPENDIX II SENSITIVITIES AND SYSTEMATICS

This appendix presents details of fit sensitivity to assumed production parameters (ie. acceptance effects) and background subtraction. The effect of systematics on net normalization is estimated. Results of the IBM analysis package are used.

AII-1) Sensitivity to Production Parameters

The Monte-Carlo weighting scheme was discussed in Section III-6. We describe the distribution of generated events as:

$$\text{Eq. AII-1) } \frac{d^4 N}{dm dp_t^2 dX_F d\cos\theta_{cs}} \propto \frac{(1 - m/\sqrt{s})^\kappa}{m^4/\sqrt{s}} e^{-\alpha p_t} (1 - |X_F|)^\beta (1 + \eta \cdot \cos^2\theta_{cs})$$

Events are generated flat in ϕ_{cs} . In Figure AII-1 thru AII-7, the sensitivity to the assumed production parameters α, β, η is investigated.* The horizontal axis of these plots determines the value of α, β, η , or κ used in the Monte-Carlo weighting. Each plot varies only one of the production parameters, while keeping the others fixed at their selected values. The vertical axis represents the value α, β, η , or κ resulting from the fit to the data (as annotated on the figure; see Sec. IV). The heavy dots represent the actual fits performed, the lighter dots are interpolations to guide the eye. The circle which is drawn on the plots represents the selected "operating point"; its x-coordinate is the value of the production parameter used in the final accepted fit, and the y-coordinate is the result of this fit. The vertical error bar is output from the fit, and the horizontal error bar is output from the corresponding fit to the varied production parameter.

The dependence of fits on their respective production parameters (ie. $p_t(\text{fit})$ vs. $p_t(\text{weight})$) is an effect of detector resolution; the acceptance is defined as the ratio of events fitted within bin limits over events generated within bin limits.

*) κ is fixed at 10 in all figures except AII-3 and AII-4, where it is allowed to vary.

AII-2) Background Sensitivity

Figures AII-8 → AII-12 study the background sensitivity of the data fits. The horizontal axis lists the percentage of full background subtracted (from 50% → 150%), and the vertical axis is the value of $\alpha, \beta, \eta, A, B, \kappa$ output from the data fit. The heavy points are results of actual fits, the light points are interpolations. The circle is the operating point at 100% background subtraction, and the error bar is output from that fit. Horizontal errors are not drawn, but from statistical arguments we expect our background accuracy to be better than 15%.

Background effects are more pronounced at lower mass; for $m > 8$ GeV there is comparatively little background, hence its effect is negligible.

AII-3) Normalization Error

From the studies contained in this appendix and Secs. II and III, we can add contributions to the systematic error on net cross-section normalization:

<u>Error Source</u>	<u>%Error</u>
Production Parameter Sensitivity	5%
Background Sensitivity	4%
Luminosity Measurement	6%
Selection Efficiency (scan error)	5%
<hr/> TOTAL	<hr/> $\sqrt{\Sigma \epsilon^2} = \underline{10\%}$

Thus we estimate that systematics on cross-section normalization amount to within a $\pm 10\%$ error.

FIGURE AII-1

$\sqrt{s}=62$ MODEL SENSITIVITY - MASS SPECTRUM

$$e^{-\kappa p_T} (1-|x_F|)^{\beta} (1+\eta \cos^2 \theta_{co}) (A(1-\sqrt{\tau})^{\kappa}/\sqrt{\tau} + B(T))$$

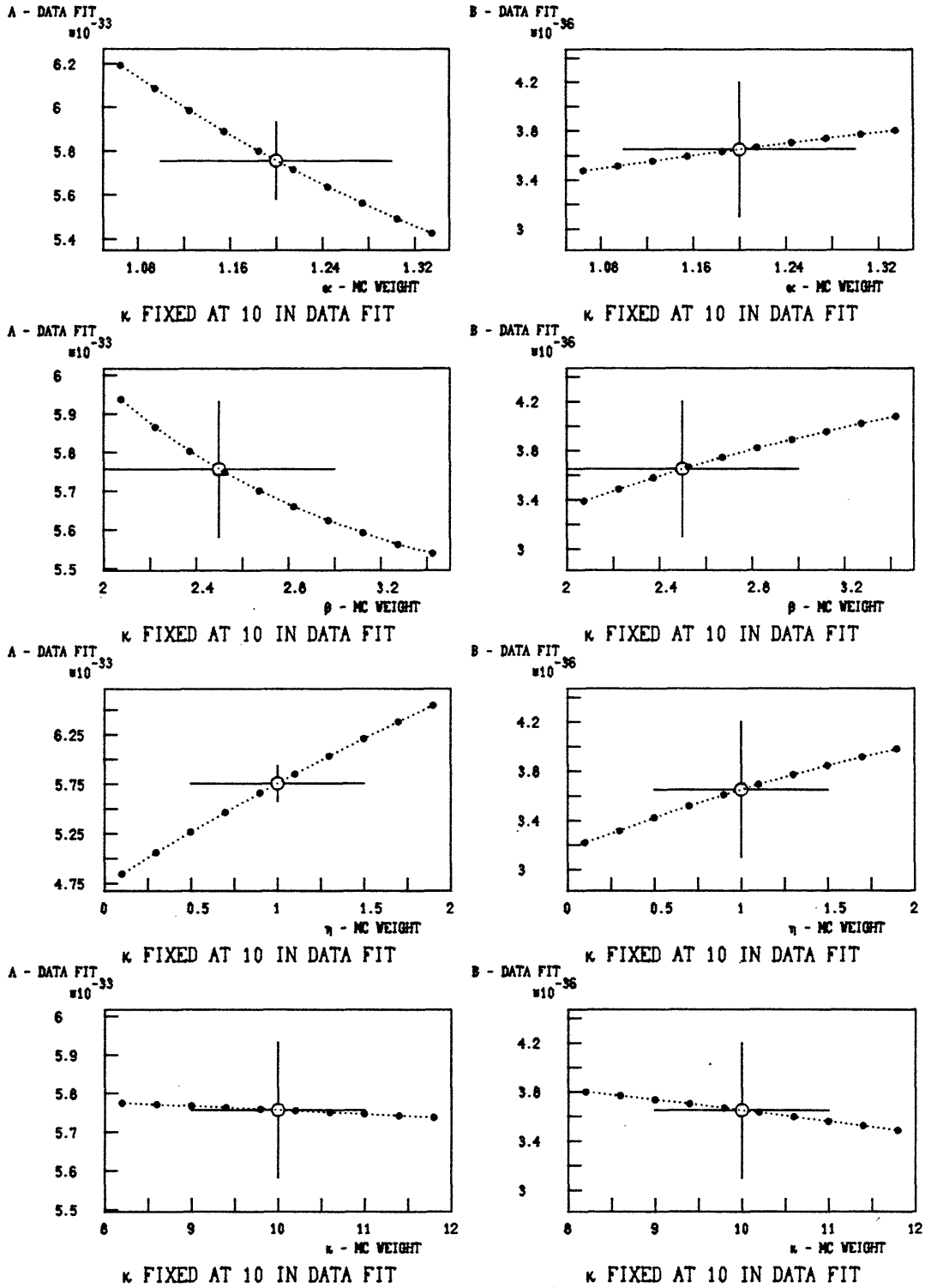


FIGURE AII-2

$\sqrt{s}=44$ MODEL SENSITIVITY - MASS SPECTRUM
 $e^{-\kappa p_T} (1-|x_F|)^{\beta} (1+\eta \cos^2 \theta_{c\bar{c}}) (A(1-\sqrt{\tau})^{\kappa}/\sqrt{\tau} + B(T))$

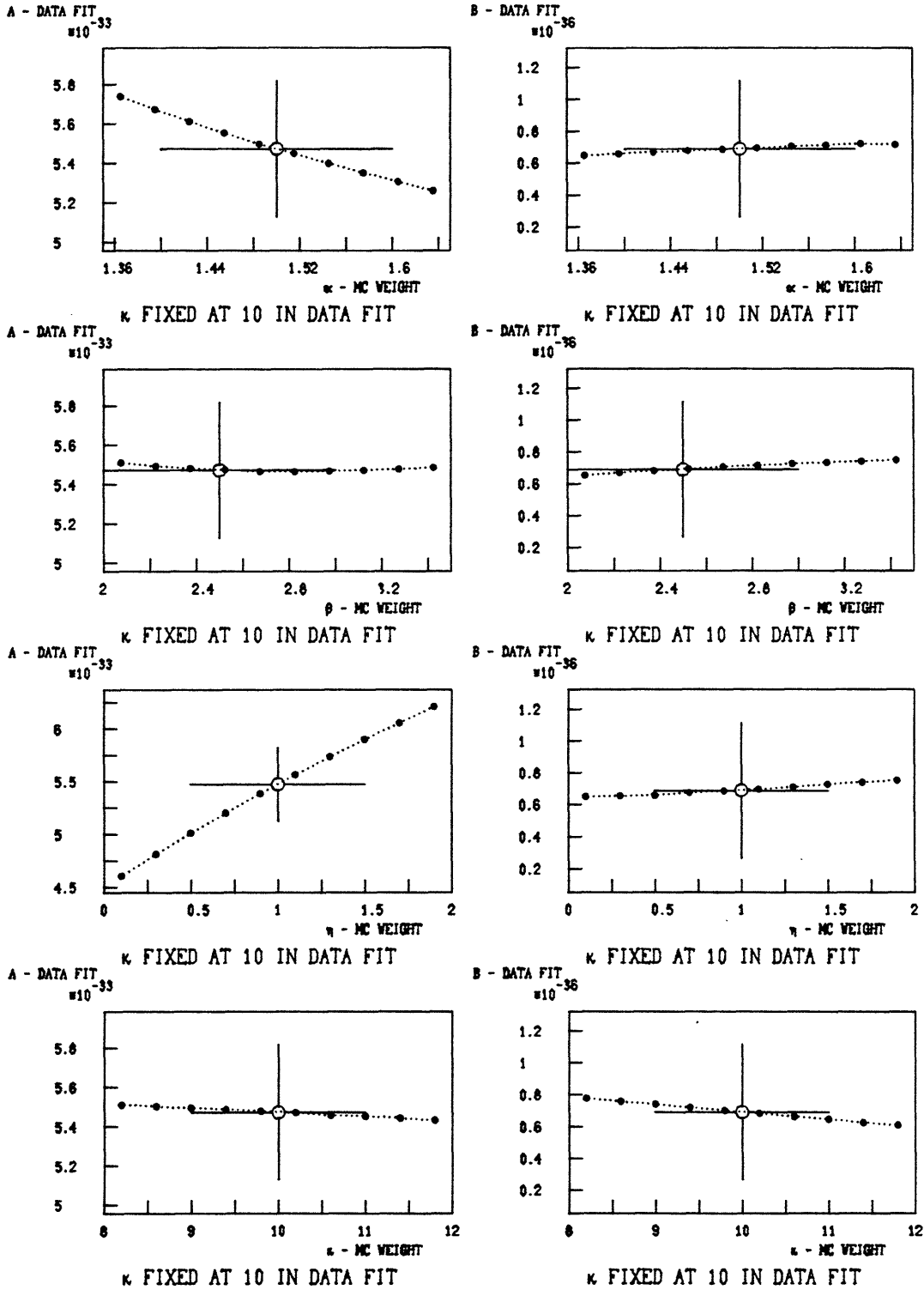


FIGURE AII-3

√s=62 MODEL SENSITIVITY - MASS SPECTRUM

$$e^{-\alpha p_1} (1-|x_F|)^{\beta} (1+\eta \cos^2 \theta_{c0}) (A(1-\sqrt{\tau})^{\kappa} / \sqrt{\tau} + B(T))$$

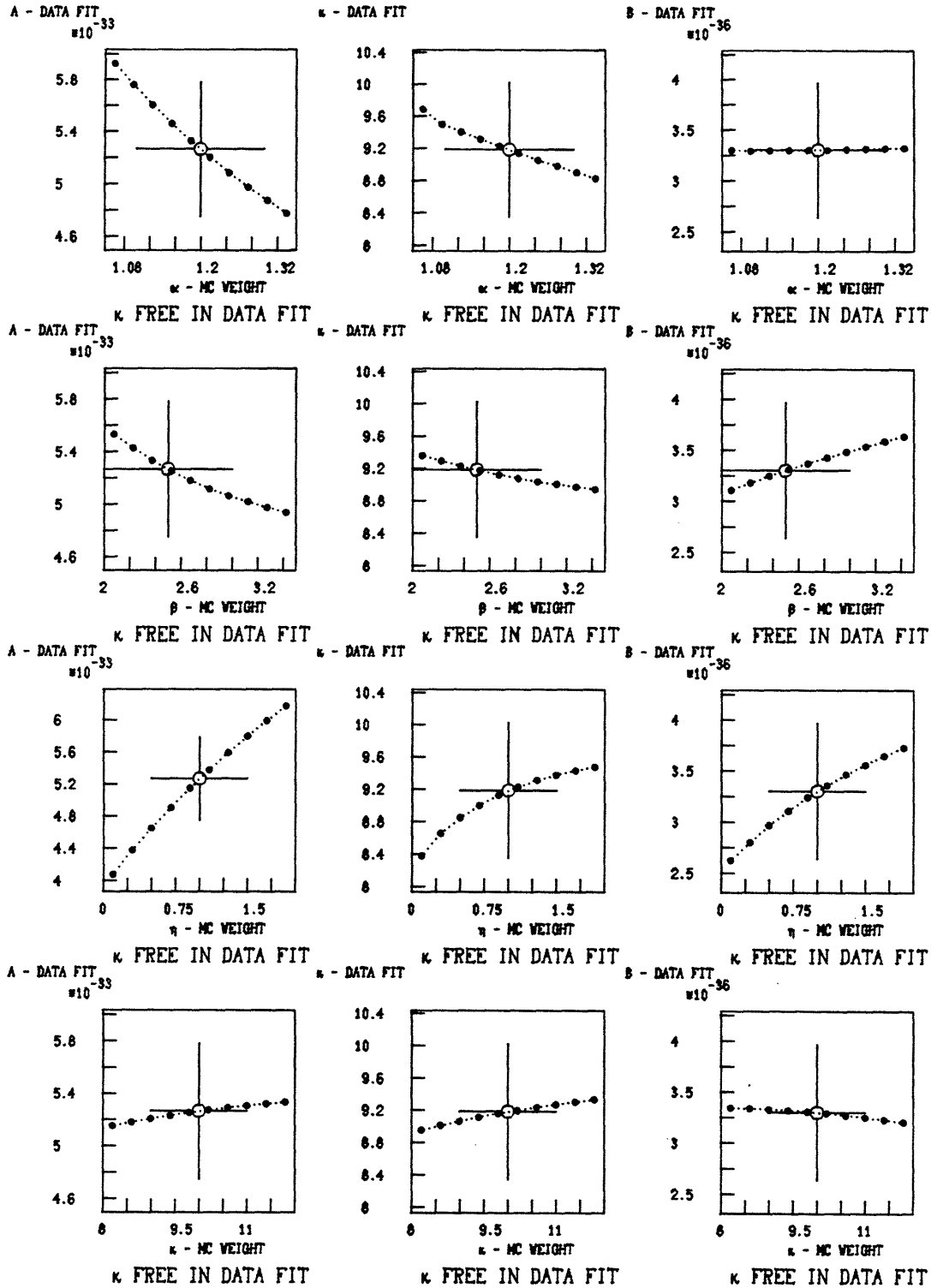


FIGURE AII-4

$\sqrt{s}=44$ MODEL SENSITIVITY - MASS SPECTRUM

$$e^{-\alpha p_1} (1-|x_F|)^{\beta} (1+\eta \cos^2 \theta_{cs}) (A(1-\sqrt{\tau})^k / \sqrt{\tau} + B(T))$$

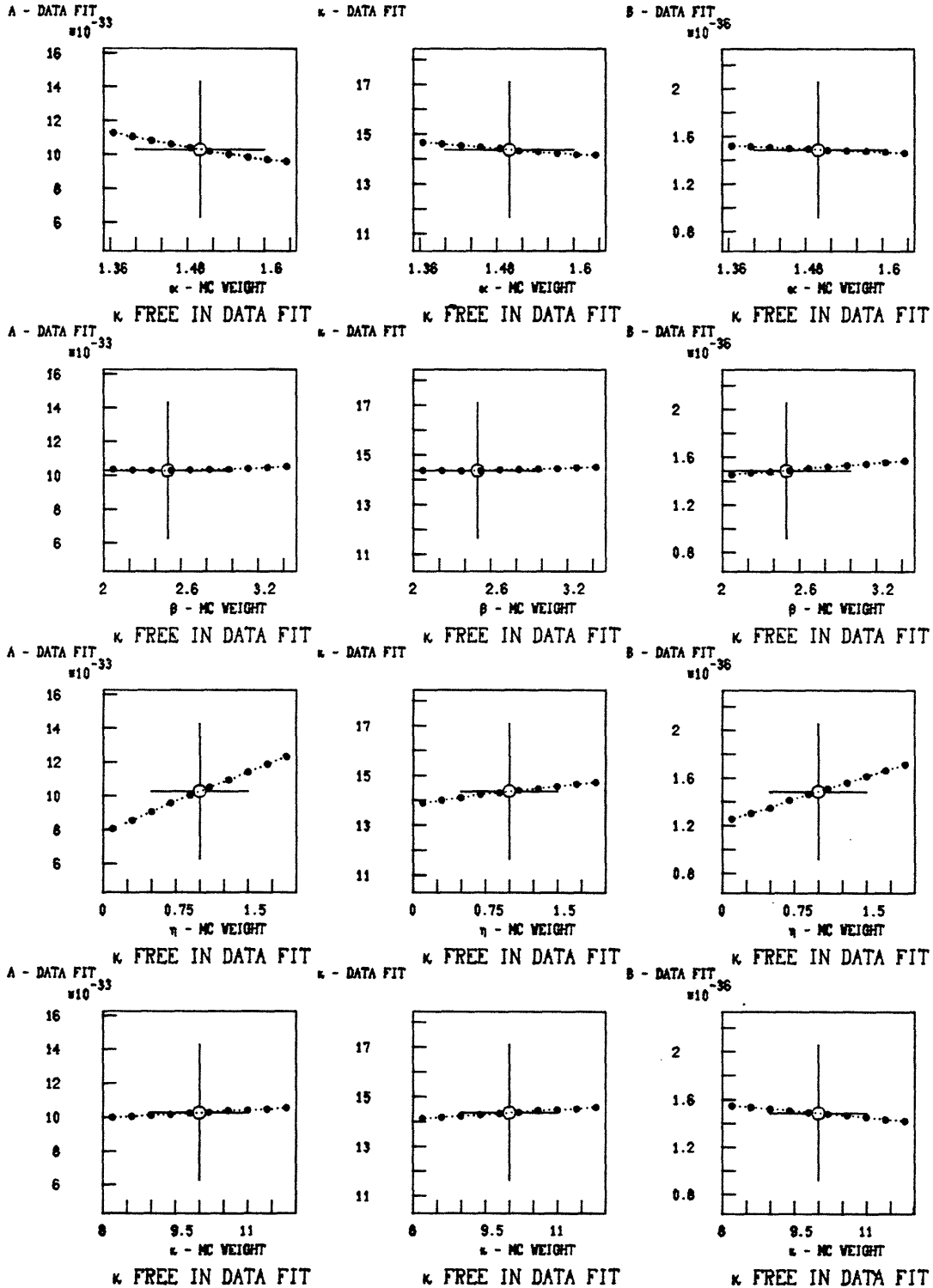
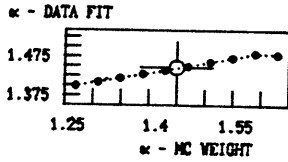


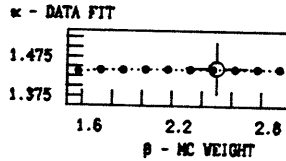
FIGURE AII-5

MODEL SENSITIVITY $e^{-\alpha P_1}$

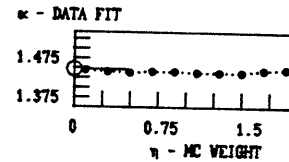
$$e^{-\alpha P_1} (1 - |x_f|)^{\beta} (1 + \eta \cos^2 \theta_{cs})$$



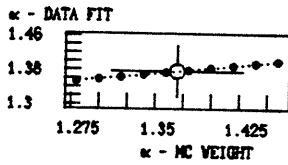
$\sqrt{s}=62$ M=2-4



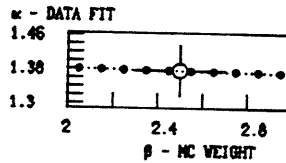
$\sqrt{s}=62$ M=2-4



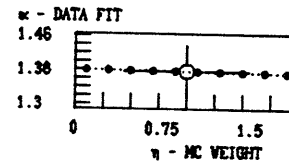
$\sqrt{s}=62$ M=2-4



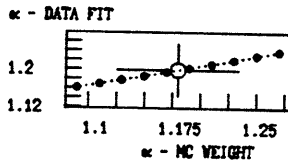
$\sqrt{s}=62$ M=5-8



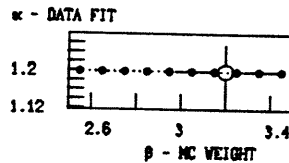
$\sqrt{s}=62$ M=5-8



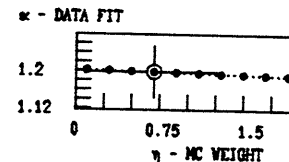
$\sqrt{s}=62$ M=5-8



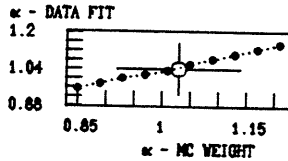
$\sqrt{s}=62$ M=8-11



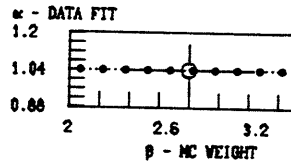
$\sqrt{s}=62$ M=8-11



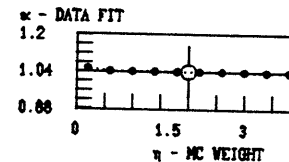
$\sqrt{s}=62$ M=8-11



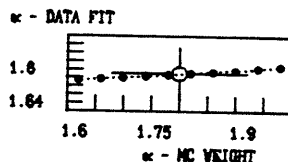
$\sqrt{s}=62$ M=11-30



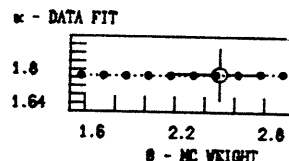
$\sqrt{s}=62$ M=11-30



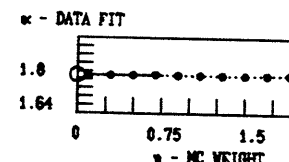
$\sqrt{s}=62$ M=11-30



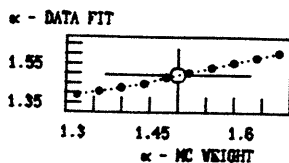
$\sqrt{s}=44$ M=2-4



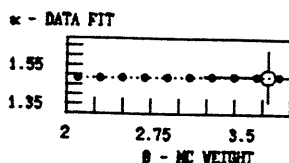
$\sqrt{s}=44$ M=2-4



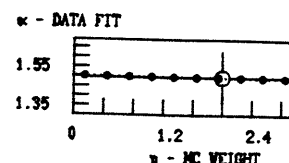
$\sqrt{s}=44$ M=2-4



$\sqrt{s}=44$ M=8-30



$\sqrt{s}=44$ M=8-30



$\sqrt{s}=44$ M=8-30

FIGURE AII-6

MODEL SENSITIVITY $(1-|x_F|)^{\beta}$

$$e^{-\alpha p_1} (1-|x_F|)^{\beta} (1+\eta \cos^2 \theta_{c_0})$$

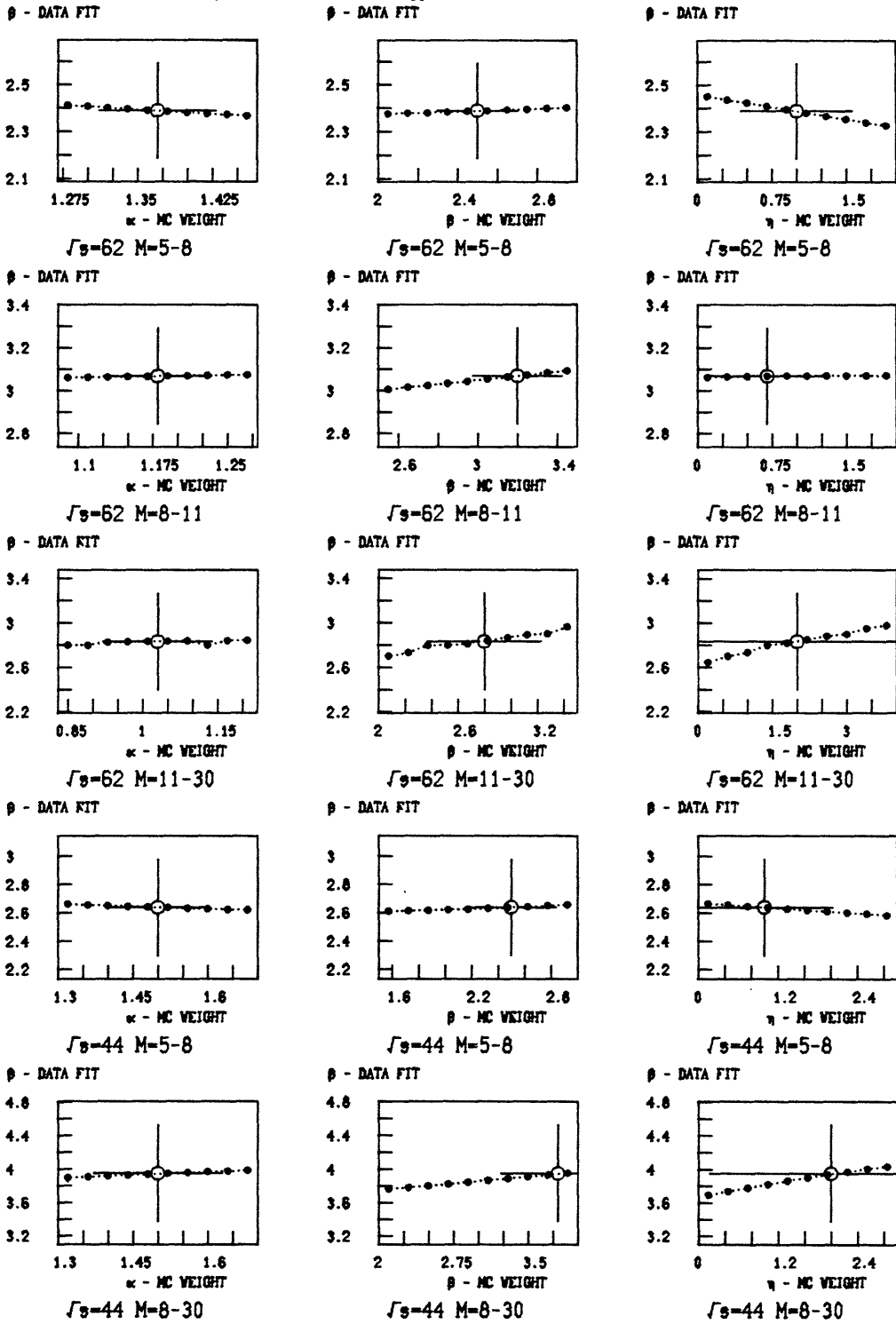


FIGURE AII-7

MODEL SENSITIVITY $1 + \eta \cos^2 \theta_{cs}$

$$e^{-x} P_1(1 - |x_F|)^{\beta} (1 + \eta \cos^2 \theta_{cs})$$

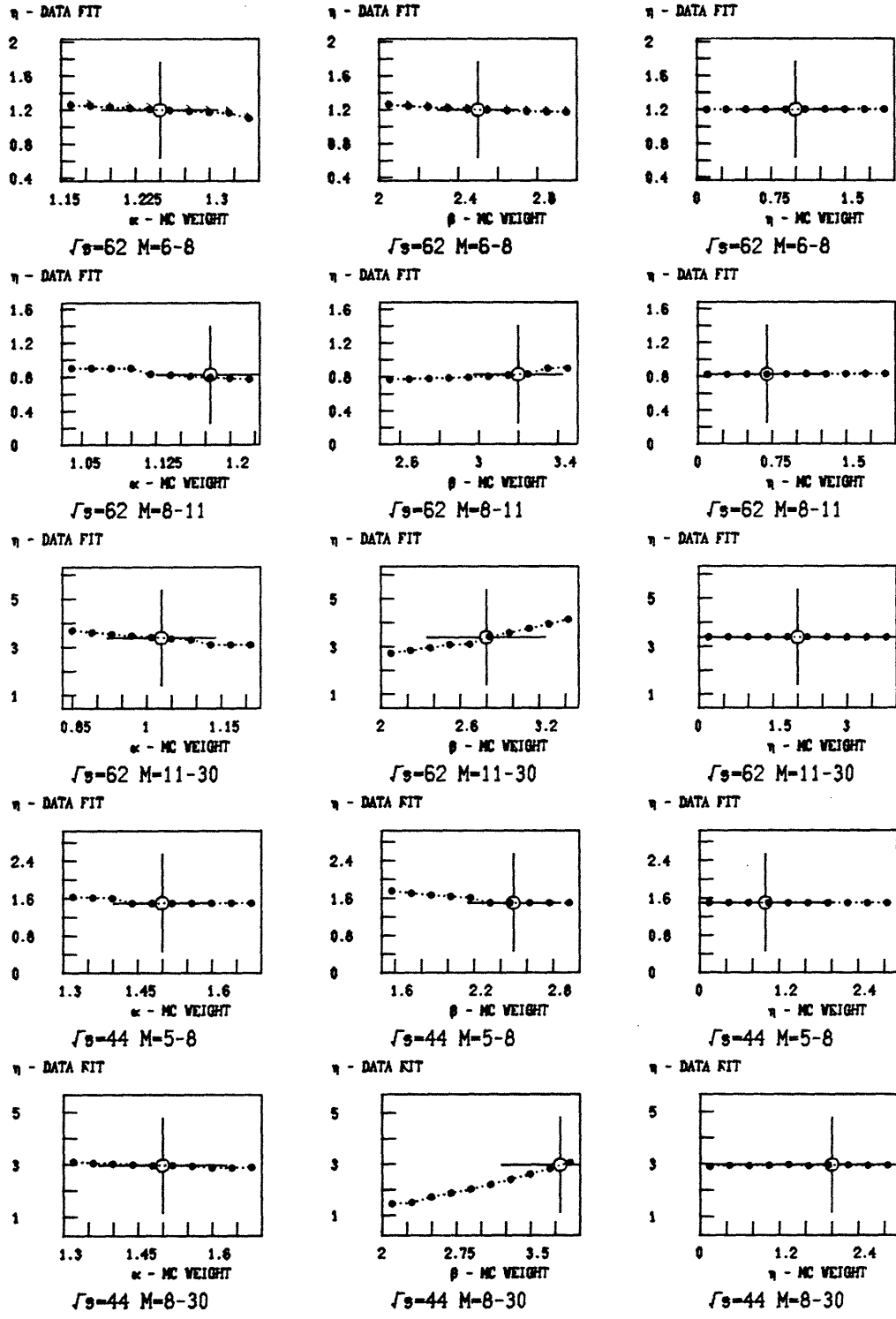
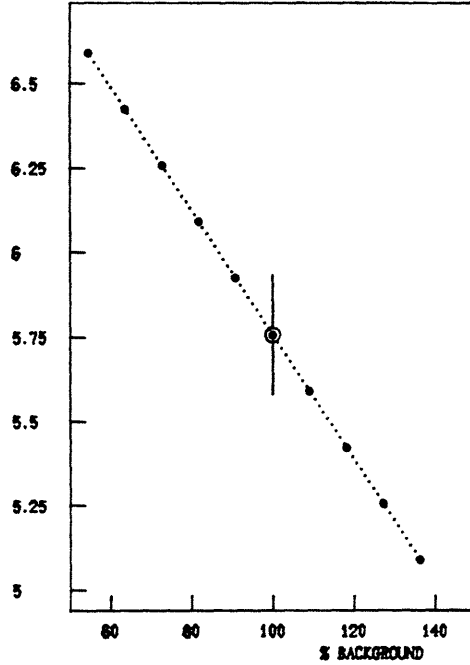


FIGURE AII-8

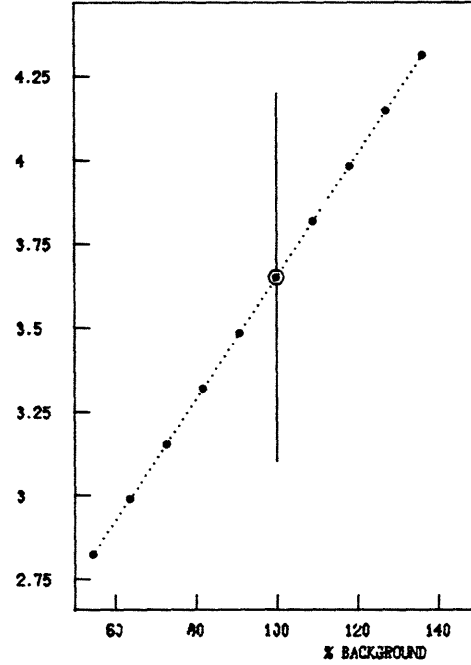
BACKGROUND SENSITIVITY $(A(1-\sqrt{\tau})^{10}/\sqrt{\tau}+B(\tau))$

A - DATA FIT_33
#10



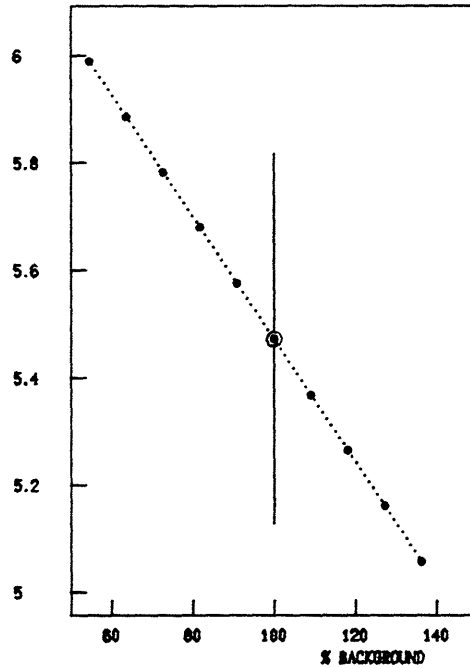
$\sqrt{s}=62$ GeV

B - DATA FIT_36
#10



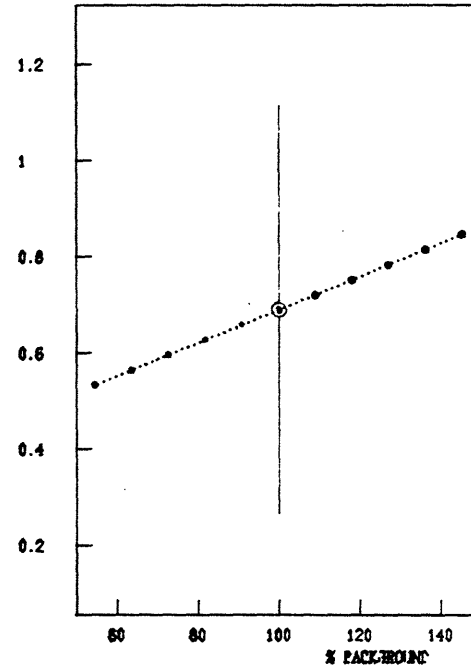
$\sqrt{s}=62$ GeV

A - DATA FIT_33
#10



$\sqrt{s}=44$ GeV

B - DATA FIT_36
#10



$\sqrt{s}=44$ GeV

FIGURE AII-9

BACKGROUND SENSITIVITY $(A(1-\sqrt{T})^k/\sqrt{T}+B(T))$

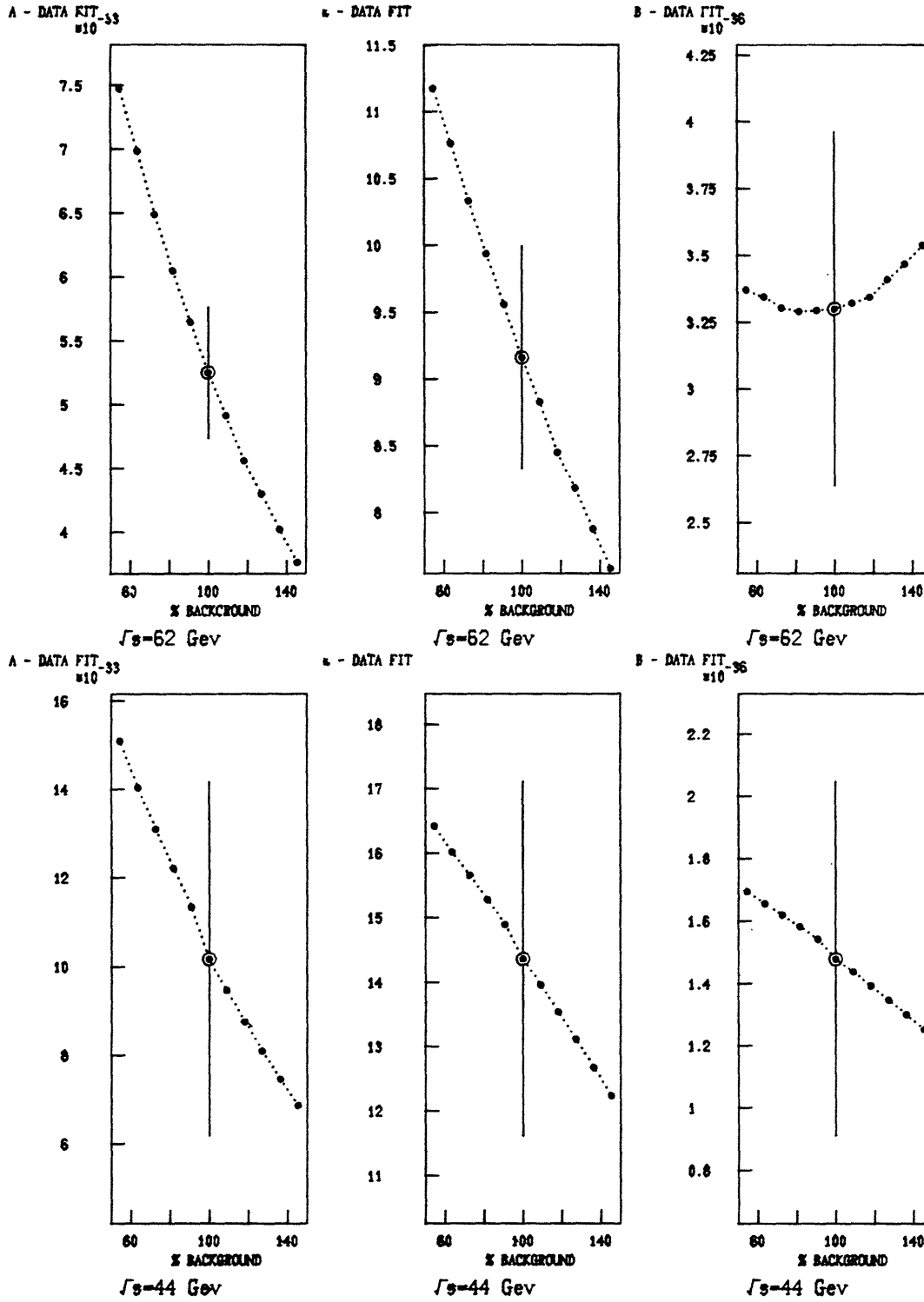
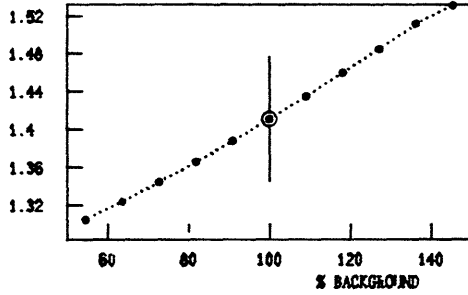


FIGURE AII-10

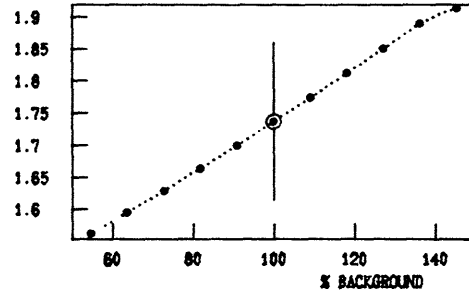
BACKGROUND SENSITIVITY $e^{-\alpha P_1}$

α - DATA FIT



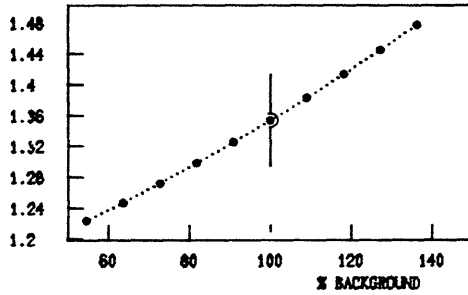
$\sqrt{s}=62$ M=2-4

α - DATA FIT



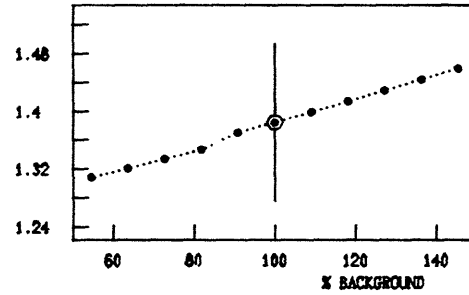
$\sqrt{s}=44$ M=2-4

α - DATA FIT



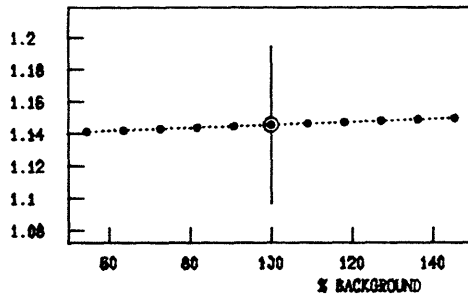
$\sqrt{s}=62$ M=5-8

α - DATA FIT



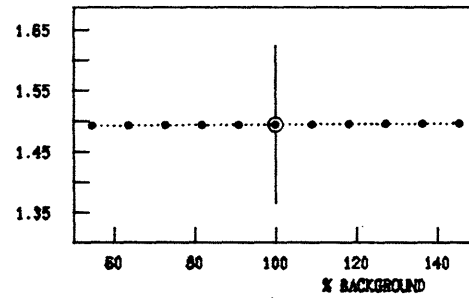
$\sqrt{s}=44$ M=5-8

α - DATA FIT



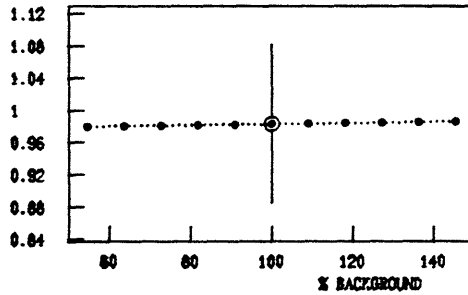
$\sqrt{s}=62$ M=8-11

α - DATA FIT



$\sqrt{s}=44$ M=8-30

α - DATA FIT

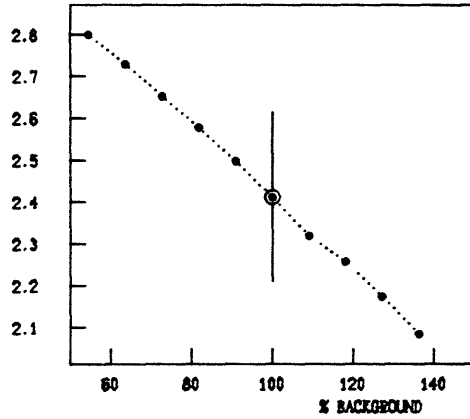


$\sqrt{s}=62$ M=11-30

FIGURE AII-11

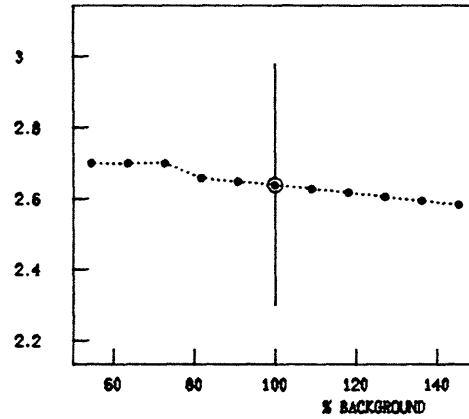
BACKGROUND SENSITIVITY $(1 - |x_F|)^{\beta}$

β - DATA FIT



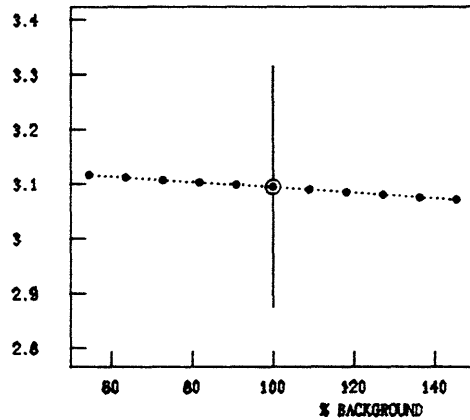
$\sqrt{s}=62$ M=5-8

β - DATA FIT



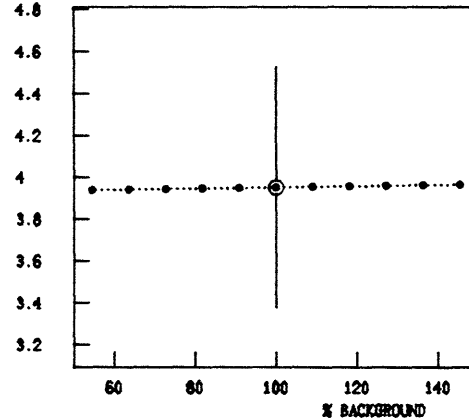
$\sqrt{s}=44$ M=5-8

β - DATA FIT



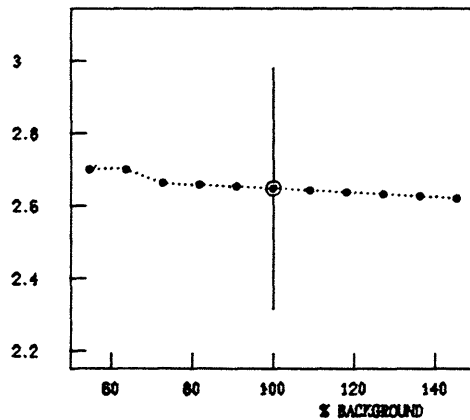
$\sqrt{s}=62$ M=8-11

β - DATA FIT



$\sqrt{s}=44$ M=8-30

β - DATA FIT

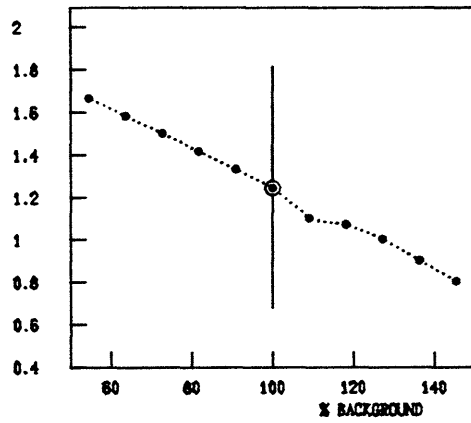


$\sqrt{s}=62$ M=11-30

FIGURE AII-12

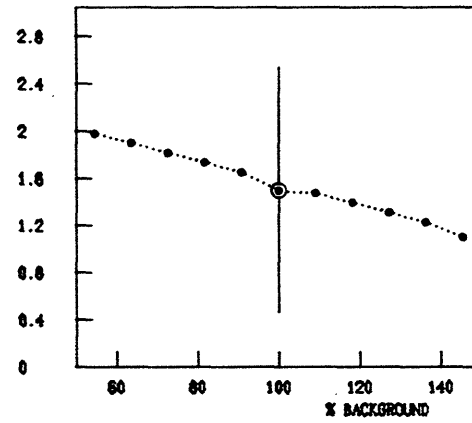
BACKGROUND SENSITIVITY $1 + \eta \cos^2 \theta_{cs}$

η - DATA FIT



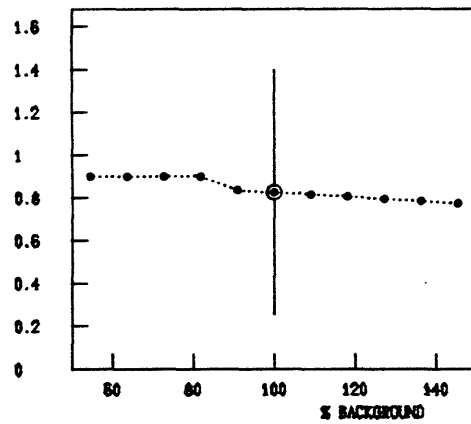
$\sqrt{s}=62$ M-6-8

η - DATA FIT



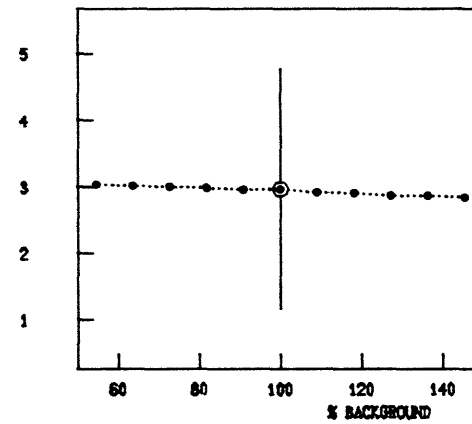
$\sqrt{s}=44$ M-5-8

η - DATA FIT



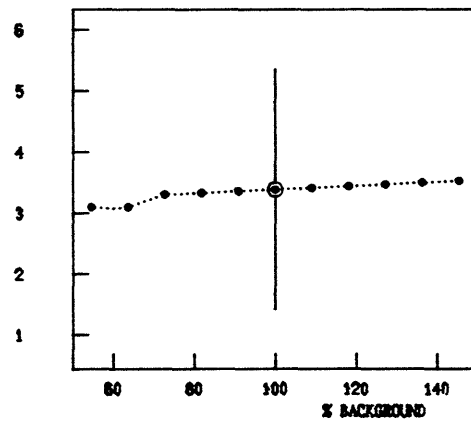
$\sqrt{s}=62$ M-8-11

η - DATA FIT



$\sqrt{s}=44$ M-8-30

η - DATA FIT



$\sqrt{s}=62$ M-11-30

APPENDIX III THE CDC ANALYSIS AND THE AVERAGING PROCESS

AIII-1) The CDC Analysis

This section briefly traces event processing through the second analysis package. The net statistics accepted by the CDC chain are generally lower than the statistics produced by the IBM programs because of the requirement of two outer chambers* per track in the CDC analysis. This is particularly relevant at low mass ($m < 4$ GeV), where the tracks produced with smaller momenta do not always penetrate the detector completely.

a) Pass 1

The CDC Pass 1 performs the same function as the IBM Pass 1; raw events are pre-filtered before being fit in Pass 2. The following cuts are applied:

- 1) The drift-times are checked on all hit chamber wires; all wires out-of-time are rejected as accidentals. At least 7 spacepoints are required in the detector.
- 2) Spacepoints must exist in two sets of outer chambers in different parts of the detector (effective ϕ -match).
- 3) ϕ -sectors are defined between the outer chambers and the intersection region; traversed counters and inner-chamber spacepoints are located in these sectors. All tracks exiting the detector must have at least one spacepoint in the inner chambers; tracks going forward must have at least two spacepoints in the inner chambers. At least two acceptable tracks must be present.
- 4) Precise spacepoints are constructed in the outer chambers using the detector survey and TDC calibrations. A straight line is fit through these points, and cuts are made on the resulting χ^2 .

*) The phrase "outer chambers" refers to the double chamber layer surrounding the periphery of the magnet outside of the D-hodoscope (see Figs. III-1 and III-3). The phrase "inner chambers" refers to the muon detection chambers sandwiched between the magnet yokes, and does not include chambers of the vertex detector (sometimes called "inner detector") or Naples telescopes; these chambers are always named more explicitly.

- 5) Spacepoints within the ϕ -sectors defined in paragraph 3 are once more located, however a more detailed reconstruction is attempted, and stricter cuts are imposed on the location of these spacepoints to reduce accidentals, "chimney" events (see Fig. III-5), and unfittable events.
- 6) Circles are constructed between the outer-chamber spacepoints and the interaction region. Loose cuts are made to insure that the spacepoints associated with candidate tracks are also consistent in the θ direction. The CDC Pass 1 accepts 0.2% of all raw triggers.

b) Pass 2

The CDC Pass 2 performs the detailed momentum fit and makes additional quality checks via the procedure detailed below:

- 1) A vertex search (see part (b) of Sec III-2) is initiated, and events without vertices are rejected. The Pass 1 cuts listed above are re-applied with slightly stricter tolerances.
- 2) An initial momentum value is assumed, and starting from the line fit through the outer chambers, candidate muon tracks are "swam" through the detector and magnetic field toward the interaction region. This "swimming" is done in 10 cm. steps, and errors due to multiple scattering, energy loss, etc. are updated after each step. A weighted χ^2 is calculated from the inner-chamber spacepoints and vertex, as sketched in Eq. III-5. An iterative χ^2 minimization program is used to determine the optimum fit; the track is re-swam after each new momentum adjustment, until the χ^2 minimum is reached. These methods are quite alien to those imposed by the IBM package; chamber weighting, calculation of energy loss, and the basic fitting methods are totally different.
- 3) Muons appearing back-to-back ($\cos\theta_{\mu\mu} < -0.96$) are assumed due to cosmic rays and are eliminated. The position intercepted along D-counters traversed by the track is estimated and required to be consistent with the value derived from counter timing. All events with both tracks traversing the D-hodoscope and having < 8 nsec. TOF difference across the detector are assumed accidental and rejected.

80% of the input Pass 1 events are approved and fitted by the CDC Pass 2.

c) Pass 3 and beyond.....

The CDC Pass 3 program reads the Pass 2 output tapes, imposes χ^2 -maximum cuts on the momentum fits, and runs further checks for cosmic rays, consistent spacepoint locations, etc. as described in (b) and (c) above. Kinematic parameters are calculated via the fitted momenta, events of different sign are separated, and a paired-background data sample is generated, normalized, and subtracted from the unlike-sign data (as in Secs. III-4 and III-6).

Monte-Carlo events (from a totally different Monte-Carlo generating program then described earlier) are fitted by Pass 2, run through the Pass 3 cuts, and packed into a multi-dimensional histogram. The data fits are attempted by re-weighting the fitted Monte-Carlo events to an assumed production model (the form of Eq. III-7 is used), and varying the weighting parameters until the Monte-Carlo distributions match those of the data-background. This differs from the approach employed by the IBM package, where fits are made to the final cross-sections in Pass 6 based on acceptances constructed in Pass 5 with static weighting parameters.

The cross-sections are derived in the CDC Pass 3 from acceptances calculated by weighting the Monte-Carlo to the final parameters output from the data fits, and dividing by the generated distribution (as in Eq. III-8).

AIII-2) The Averaging Process

The results of both analysis chains were compared in Sec. III-8. To account for any systematic differences in X_F , p_t , and $\cos\theta_{cs}$ distributions over the selected mass intervals, the cross-sections were averaged together bin-by-bin. The IBM and CDC results were given equal weight. If one analysis was missing a point (due to lack of statistics), the results of the other analysis were used unaltered.

In summary, the cross-sections were averaged as:

$$\langle d\sigma/d\lambda \rangle = \frac{1}{2} [d\sigma/d\lambda_{(IBM)} + d\sigma/d\lambda_{(CDC)}]$$
$$\langle \epsilon \rangle = \sqrt{(\epsilon_{(IBM)}^2 + \epsilon_{(CDC)}^2)/2}$$

Due to good normalization agreement, the IBM results are used unaltered for $d\sigma/dm$.

APPENDIX IV SEARCH FOR EVIDENCE OF THE 2γ PROCESS

Figure AIV-1 shows the distributions of charged particle multiplicity associated with the muon pairs. The inner (vertex) detector and forward telescopes were described in Sec. II-1. Only tracks in the inner detector are examined ($7^\circ < \theta < 171^\circ$), tracks found in the forward telescopes are not counted. The data includes all events with $m < 15$ GeV and $p_t < 5$ GeV, and has not been corrected for vertex detector acceptance.¹⁾ If at least one charged track is within 200 mrad, of a muon track (as extrapolated from the momentum fit), it is considered "linked" to the muon, and the multiplicity count is decremented by 1. In this way, contribution from the muon pair is subtracted from the multiplicity count, and we plot "multiplicity minus muons" in Fig. AIV-1.

There are an average of 3.6 spacepoints per charged track. We require at least one spacepoint in the chambers of the vertex detector to be within 10 cm. of each extrapolated muon track. Runs with average hadron multiplicities of under 4 tracks/event were eliminated, as well as events suffering from excessive noise in the chambers. We require:

$$\#spacepoints < (4.75) \cdot \#tracks + 16$$

for each event. This cut was derived by examining the distribution of total spacepoints in the vertex detector chambers vs. the number of constructed tracks.

The average multiplicities have been estimated from the histograms in Fig. AIV-1. At 62 GeV, we find (with muons subtracted) $\langle N \rangle \approx 10.6$ for the $\mu^+\mu^-$ data ($\langle N \rangle = 12.5$ for like sign background), and at 44 GeV, we see $\langle N \rangle = 9.0$ for the $\mu^+\mu^-$ data ($\langle N \rangle = 10.6$ for like sign background).

In Fig. IV-14 (a), an enhancement can be noticed at zero multiplicity; ie. an excess of dimuon events produced without any observed hadrons. This enhancement is not significantly present in the 44 GeV data (Fig. AIV-1 (b)). or like sign distributions.

Over 90% of all events having under 3 charged tracks (not incl. muons) in the inner detector have no vertex. This reduces the efficiency of the track-finding program. To ascertain the effects of inefficiency upon low multiplicity candidates, pictures of the inner-detector were manually scanned for these events. Vertices were estimated, and any extra hadron

tracks missed by the analysis program were recovered and counted. Pictures of the outer detector were made for the clean hadronless events (see Fig. AIV-2), and 90% were found to be bona-fide dimuons. The multiplicity plot resulting from this scan²⁾ still shows an excess of hadronless events.

Figure AIV-3 shows the multiplicity-minus-muons distribution for the 62 GeV $\mu^+\mu^-$ data, with tracks in the forward telescopes ($1^\circ < \theta < 30^\circ$) included. We find $\langle N \rangle = 12.3$ from this distribution (≈ 1.7 tracks added per event). The vertex-finding efficiency rises from 90% to 97% with the inclusion of the telescope data in the analysis. This reduces contamination from inefficiency in lower multiplicity events, and the enhancement of the hadronless bin is seen even more clearly.

An explanation for this effect has been proposed²⁾ in which the hadronless dimuons arise from the elastic 2γ process, as sketched in Fig. I-4. Calculations^{2,3)} have indicated that the scattered protons will remain in the beamline over the distance covered by the inner chambers and telescopes, resulting in the appearance of a "hadronless" event. Based on 2γ Monte-Carlo simulations,^{3,4)} a sample of ≈ 70 elastic 2γ events are expected to be accepted by the detector over the luminosity accumulated at 62 GeV. This is in approximate agreement with the ≈ 100 hadronless event excess found in Fig. AIV-3 and the event scan. The growth of the 2γ process with $[\ln(s)]^3$ predicts⁴⁾ a 30% reduction of the hadronless excess at $\sqrt{s} = 44$ GeV, which may support the lack of hadronless events in Fig. AIV-1 (b).

Weighting our Monte-Carlo to be predicted 2γ production characteristics,^{3,4)} we show the mass spectrum of the generated and accepted 2γ events in Fig. AIV-4 (a). Due to the acceptance cutoff at low mass, the fitted event distribution peaks at $m \approx 5$ GeV and falls rapidly with decreasing mass, despite the exponential rise in the generated spectrum as $m \rightarrow 0$. In Fig. AIV-4 (b), we compare the fitted 2γ Monte-Carlo mass distribution (dashed line) with that of the actual hadronless event sample (data points). The hadronless events rise to a peak at $m = 3$ GeV, which is not exhibited by the 2γ Monte-Carlo. The higher multiplicity data (solid line) also shows the peak at $m=3$ GeV, which is understood to arise from $J \rightarrow \mu^+\mu^-$. Because of charge-conjugation invariance, the J can not be produced directly by the 2γ process. Insufficient statistics exist beyond the J region ($m > 4.5$ GeV) to enable a significant comparison between

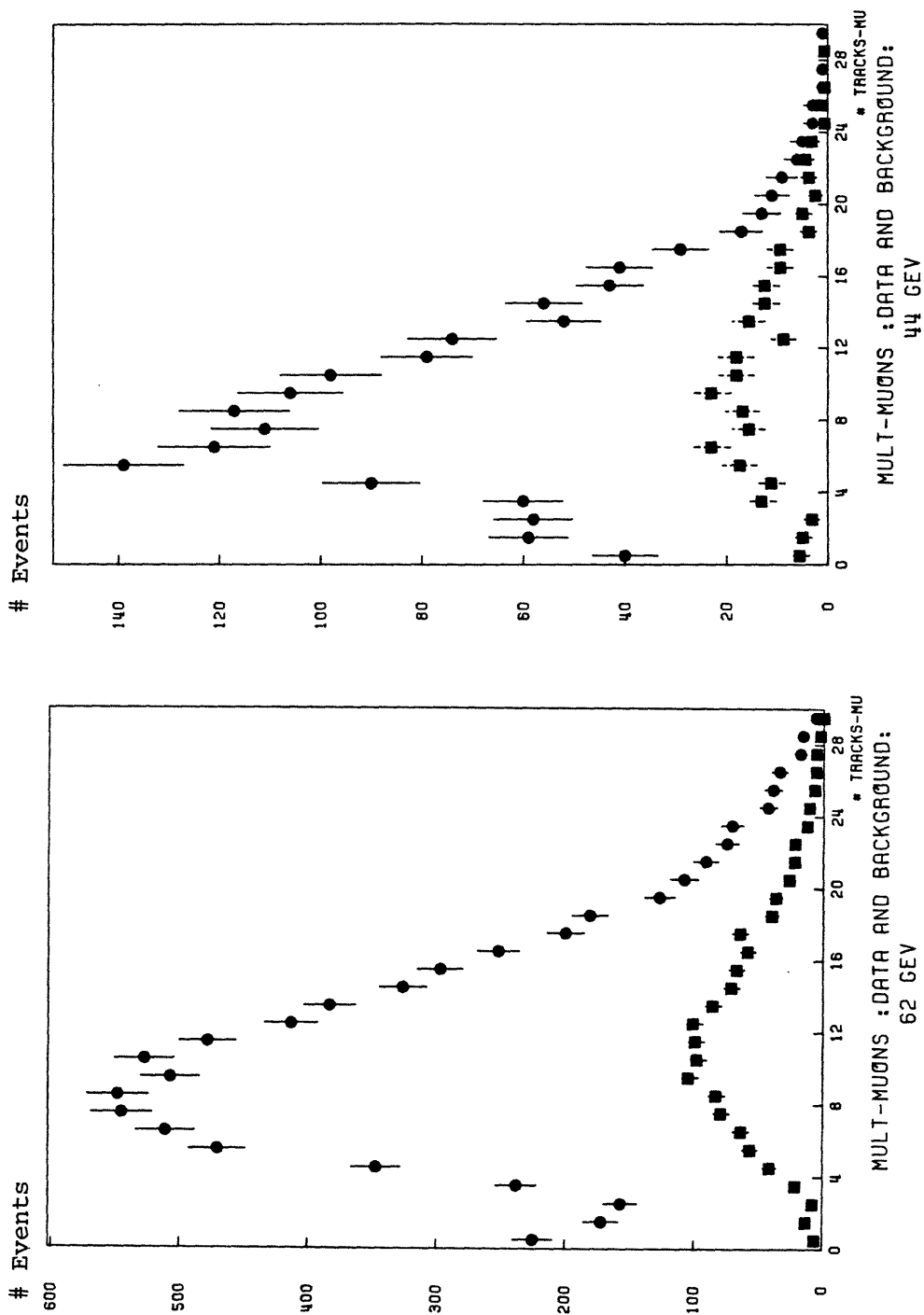
hadronless events, 2γ Monte-Carlo events, and higher multiplicity events.

Thus the sample of hadronless events obtained at 62 GeV appears to be dominated by $J \rightarrow \mu^+ \mu^-$, and shows no evidence of 2γ production characteristics which can be significantly discerned from the spectra of higher multiplicity data.

REFERENCES

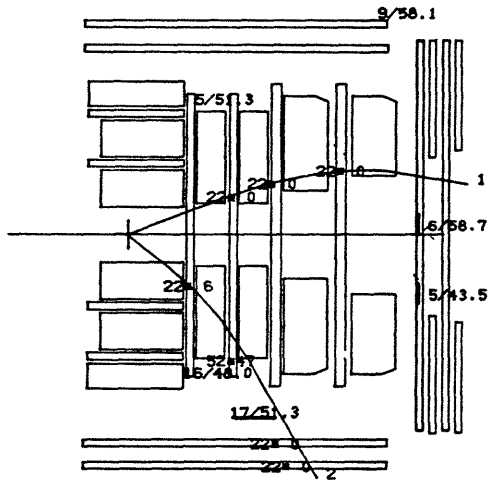
- 1) D. Antreasyan et. al., (article on associated multiplicity to be published in Nuc. Physics B).
V. Cavassinni, Thesis, Scuola Normale Superiore, Pisa (1978).
- 2) F. Vannucci, "Evidence for 2γ Processes at the ISR",
CERN-EP/80-82 (1980).
- 3) J.A.M. Vermaseren, private communication.
- 4) R. Moore, Z. Phys. C5, 351 (1980).

FIGURE AIV-1

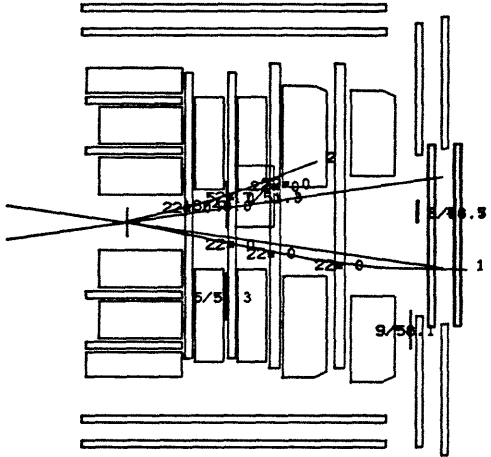
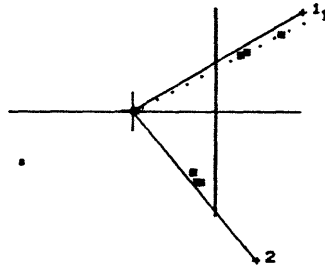


Charged particle multiplicity distributions for unlike-sign data (circles) and like-sign background (squares). The background distributions are normalized as in Eq. III-6. Tracks found in the forward telescopes are not included. The muons have been subtracted from the multiplicity count.

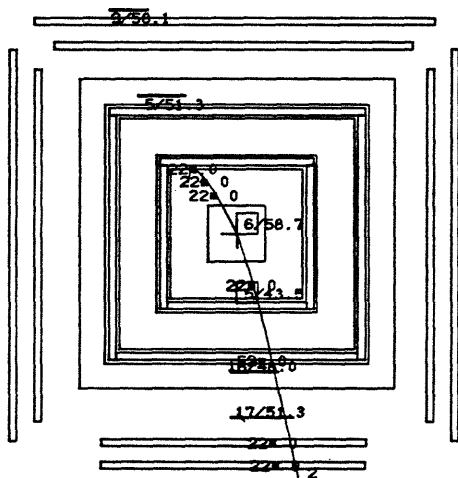
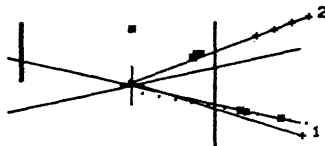
FIGURE AIV-2 A TYPICAL HADRONLESS EVENT



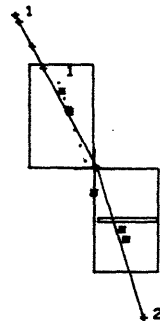
Side View



Top View



Rear View



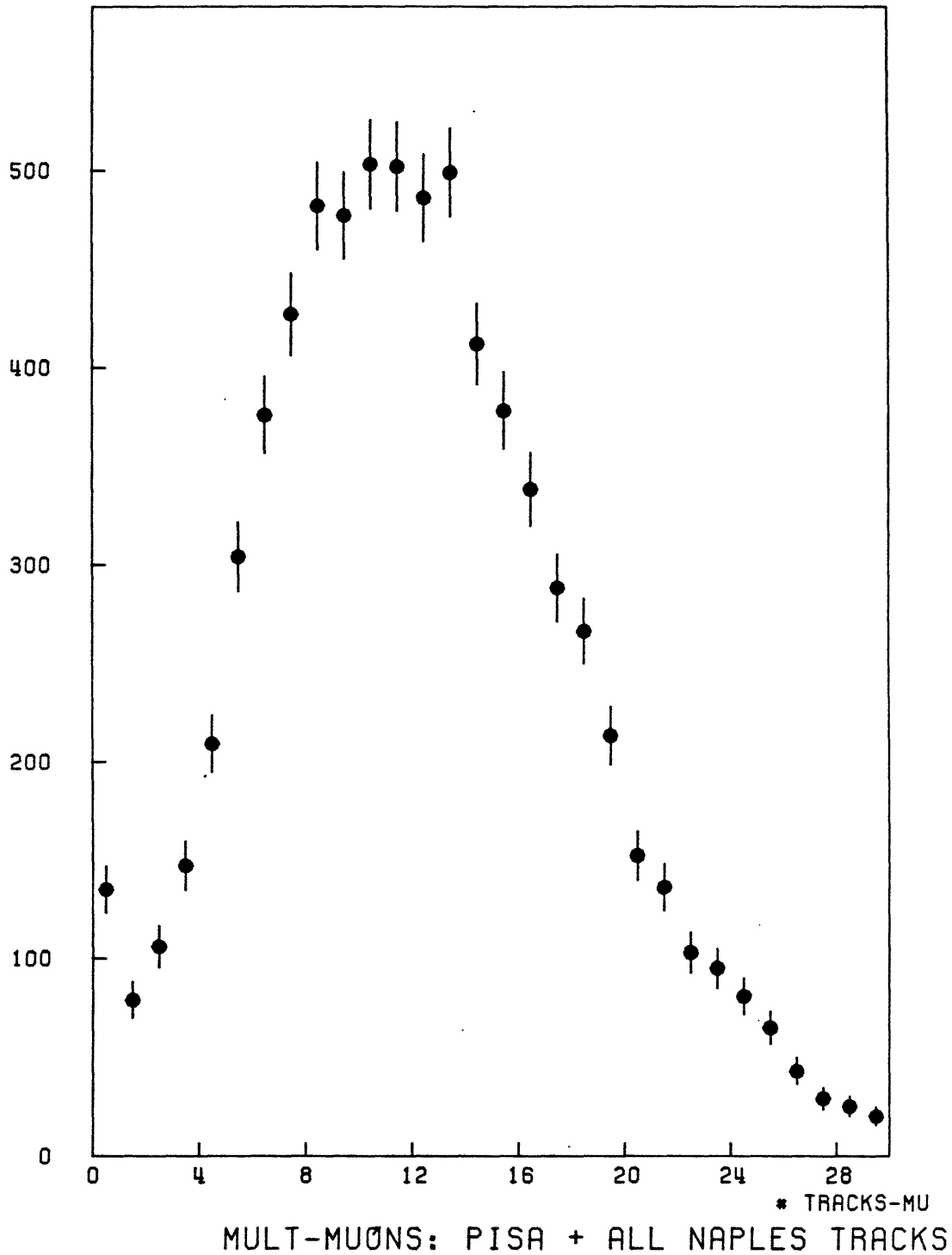
MUON DETECTOR

INNER DETECTOR

RUN NO 1257 EVENT 5621
 MASS= 3.672 PPERP= 0.694 XF=0.221
 P1= 4.84 X1= 0.79 P2= -2.93 X2= 1.25
 BDL1= 24.66 BDL2= 22.43

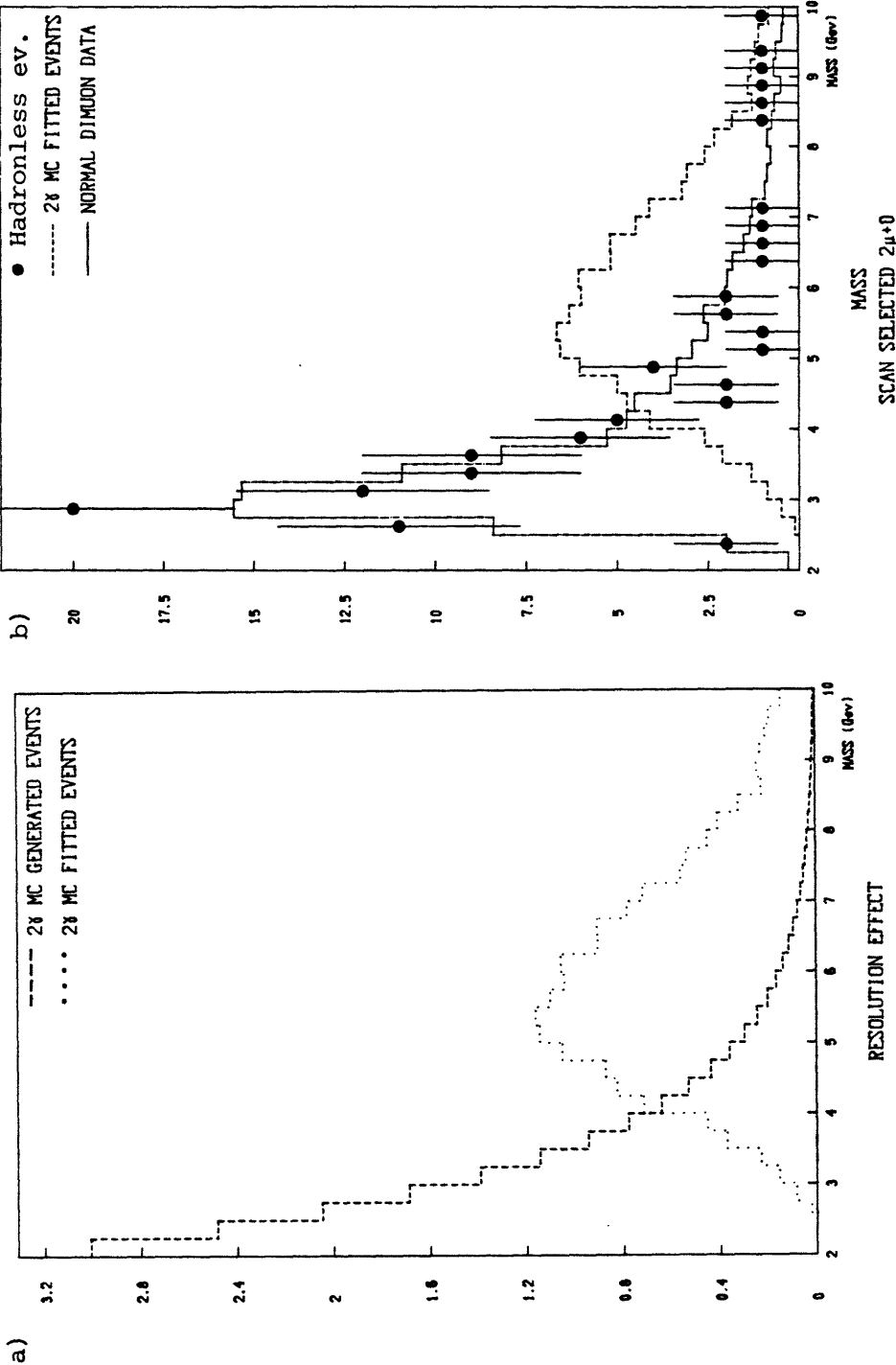
Both muons are "linked" with tracks and/or spacepoints in the inner detector. This event should be compared with a standard event (as in Fig. II-6), where much more activity is present in the vertex detector.

FIGURE AIV-3



Charged particle multiplicity distribution (muons subtracted) for the unlike-sign data at $\sqrt{s} = 62$ GeV, including tracks found in the forward telescopes. The excess of hadronless events can be seen more clearly due to the increase in vertex-finding (hence track-finding) efficiency.

FIGURE AIV-4



Part a) shows the spectrum of generated 2γ Monte-Carlo events vs, that of the fitted and accepted 2γ Monte-Carlo events. The effects of the acceptance cutoff at low mass are evident.
 Part b) shows the distribution of hadronless events (selected by the eye-scan) compared with the 2γ Monte-Carlo prediction (dotted line) and higher multiplicity data (solid line). The J peak at 3 GeV is seen in both hadronless and higher multiplicity events, in disagreement with 2γ Monte-Carlo predictions. The 2γ Monte-Carlo and higher multiplicity distributions are normalized to the hadronless event distribution.

ACKNOWLEDGMENTS

The years I have spent as an MIT student will always number as one of the most exciting and influential periods of my life. I am very grateful to all who have helped to make it such.

It is a pleasure to thank my advisor, Prof. Ulrich Becker for his guidance, assistance, concern, and friendship during my stay at MIT and CERN. It has been enjoyable working with him. His criticism and advice have proven instrumental in the effort and preparation leading to this thesis, and his dedication and competence will always serve as an inspiration to me.

Very special thanks are extended to my friend and co-worker, Francois Vannucci. Our many discussions have paved the way for this thesis; his criticism has been indispensable, and his encouragement was always a welcome boost. Equally important were the occasional philosophical digressions, impromptu jokes, and walks through the Jura mountains upon which we embarked.

Dikran Antreasyan deserves special acknowledgment in this thesis. His assistance has been greatly appreciated, both with dimuon physics and the Swiss Automobile Bureau. Without the limitless help and patience of Walter Toki, I would have had little chance of charting my way triumphantly through the maze of MORTRAN known as the IBM analysis package. Mike Hodous's complete knowledge of data tape format and CDC computer systems proved extremely useful, and his friendship, practicality, assistance, and textbooks were always appreciated. I'm grateful to Manfred Steuer for his help in keeping the detector together, and for his assistance in coping with the inevitable Swiss bureaucracy. Laura Perasso's help with experimental procedure was appreciated, and I acknowledge Terry Lagerlund for writing one of the most complete and intelligent on-line software packages that I've had the pleasure of working with. Karl Strauch deserves thanks for his help in completing our publications. Prof. S.C.C. Ting warrants special acknowledgment for his leadership, which made the experiment possible.

Other members of the collaboration have made major contributions to the experiment at various points; in particular, I would like to thank

Bill Atwood, Jim Branson, Joe Burger, Min Chen,, M. Fudisaki, Takeshi Matsuda, Harvey Newman, Dave Novikoff, and Ingrid Schulz for their participation. I acknowledge the support staffs from CERN for their excellent performance; in particular I would like to thank Ola Leistam of the ISR division for his help in keeping the experiment running, and Harry Renshall of the PEO for his assistance with TRIAB. I am thankful to the Pisa/Naples portion of our collaboration for their support; Nino DelPrete, Marisa Valdata-Nappi, Vincenzo Cavasinni, Piero Braccini, and Giorgio Bellettini were of particular help to me. I would like to extend special thanks to Ariella Cattai for her friendship and support throughout my hectic last months at CERN.

The administrative and support personnel at MIT and LNS certainly deserve mention in this thesis; Jean Hudson, Susan Marks, Fred Epling, Jim Donahue, and Peter Berges gave much help and encouragement. No thesis at MIT is complete without thanking Terry Crossley in the Physics Graduate office; her optimism and support will be long remembered. I am grateful to the MIT Physics Department for their support during my first three years at MIT as a Karl Taylor Compton Fellow. The help and patience of Nick Saia and the illustrators of the LNS drafting office was much appreciated.

I thank the many people at Tufts University who made my undergraduate years most profitable and prosperous; in particular I acknowledge Fu Tak Dao for encouraging me to pursue particle physics. My former co-workers at the Charles Stark Draper Laboratory also deserve recognition in this thesis; the experience I gained there in systems engineering and real-time programming have proven indispensable during my stay at MIT.

Last (but hardly least), I would like to acknowledge my parents. By encouraging my scientific interests and curiosity as a child, they ignited the motivation leading toward the completion of this thesis. Their patience and support has always been beyond compare. They certainly deserve special mention here; in addition to their role as parents, my mother's help in typing this manuscript was irreplaceable, and my father's assistance in preparing the figures and graphics was essential.

PRINTER PLOTS



Computer reconstructions of the vertex detector, showing charged hadron tracks associated with the muon pair. This figure is included for aesthetic purposes only.